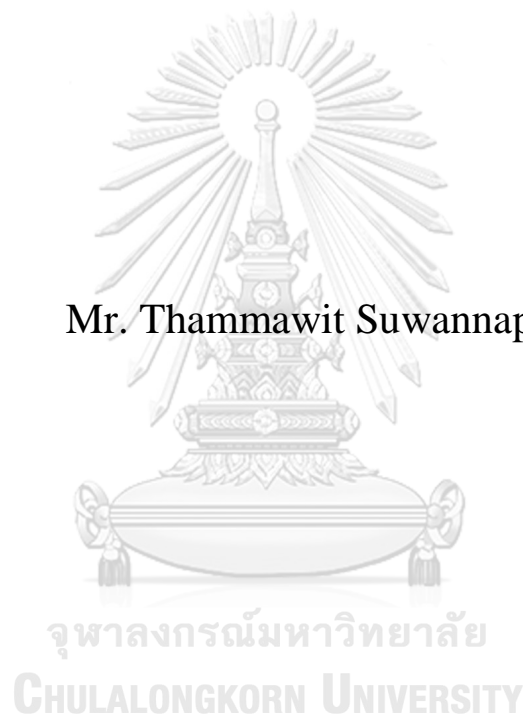


Development of an Integrated Microfluidic System for Cell  
Sorting and Trapping—Considering Sorting Efficacy and Cell  
Viability

Mr. Thammawit Suwannaphan



A Dissertation Submitted in Partial Fulfillment of the Requirements  
for the Degree of Doctor of Philosophy (Mechanical Engineering) in  
Mechanical Engineering  
Department of Mechanical Engineering  
FACULTY OF ENGINEERING  
Chulalongkorn University  
Academic Year 2020  
Copyright of Chulalongkorn University

การพัฒนาระบบของไหลจุดภาคแบบบูรณาการสำหรับการคัดแยกและดักจับเซลล์—คำนึงถึง  
ความสามารถในการคัดแยกและการมีชีวิตของเซลล์



วิทยานิพนธ์นี้เป็นส่วนหนึ่งของการศึกษาตามหลักสูตรปริญญาวิศวกรรมศาสตรดุษฎีบัณฑิต  
สาขาวิชาวิศวกรรมเครื่องกล ภาควิชาวิศวกรรมเครื่องกล  
คณะวิศวกรรมศาสตร์ จุฬาลงกรณ์มหาวิทยาลัย  
ปีการศึกษา 2563  
ลิขสิทธิ์ของจุฬาลงกรณ์มหาวิทยาลัย

Thesis Title	Development of an Integrated Microfluidic System for Cell Sorting and Trapping— Considering Sorting Efficacy and Cell Viability
By	Mr. Thammawit Suwannaphan
Field of Study	Mechanical Engineering
Thesis Advisor	Associate Professor ALONGKORN PIMPIN, Ph.D.
Thesis Co Advisor	Wutthinan Jeamsaksiri, Ph.D.

---

Accepted by the FACULTY OF ENGINEERING, Chulalongkorn University in Partial Fulfillment of the Requirement for the Doctor of Philosophy (Mechanical Engineering)

..... Dean of the FACULTY OF ENGINEERING  
(Professor SUPOT TEACHAVORASINSKUN, Ph.D.)

#### DISSERTATION COMMITTEE

..... Chairman  
(Assistant Professor WERAYUT SRITURAVANICH, Ph.D.)

..... Thesis Advisor  
(Associate Professor ALONGKORN PIMPIN, Ph.D.)

..... Thesis Co-Advisor  
(Wutthinan Jeamsaksiri, Ph.D.)

..... Examiner  
(Assistant Professor SARAN SALAKIJ, Ph.D.)

..... Examiner  
(Professor ACHARIYA SAILASUTA, Ph.D.)

..... External Examiner  
(Associate Professor Vejapong Juttijudata, Ph.D.)

ชรรณวิทย์ สุวรรณพันธุ์ : การพัฒนาระบบของไหลจุลภาคแบบบูรณาการสำหรับการคัดแยกและดักจับเซลล์—คำนึงถึงความสามารถในการคัดแยกและการมีชีวิตของเซลล์. ( Development of an Integrated Microfluidic System for Cell Sorting and Trapping— Considering Sorting Efficacy and Cell Viability) อ.ที่ปรึกษาหลัก : รศ. ดร. อลงกรณ์ พิมพ์พิณ, อ.ที่ปรึกษาร่วม : ดร. วุฒินันท์ เกียรติศักดิ์ศิริ

การศึกษานี้แบ่งออกเป็นสองส่วน ในส่วนแรกเป็นการศึกษาเพื่อตรวจสอบการมีชีวิตรอดและความเสียหายของเซลล์เม็ดเลือดขาวหลังจากการแยกด้วยระบบอุปกรณ์ที่ออกแบบแล้วและต่อหลอด-ท่อขยายที่อัตราการไหลที่เหมาะสมในการคัดแยกขนาดของเซลล์ มีการทดสอบสามเทคนิคได้แก่ การย้อมสีทริฟแพนบลู กล้องจุลทรรศน์อิเล็กตรอนแบบส่องกราด และการย้อมสีแบบสี่ไรท์จิมซ่า หลังจากฉีดเซลล์ผ่านระบบอุปกรณ์ที่ออกแบบแล้วที่อัตราการไหล 2 มิลลิเมตรต่อนาที พบว่าเซลล์มีชีวิตรอด 85% เซลล์เกิดการเสียชีวิตรูปร่าง 30% และมีความเสียหายต่อโครงสร้างภายในเซลล์ 2% ตามลำดับ ผลทดสอบในอุปกรณ์ที่ท่อหลอด-ท่อขยายพบว่าเซลล์มีชีวิตรอด 89% ขณะที่เซลล์เกิดการเสียชีวิตรูปร่าง 12% และเกิดความเสียหายต่อโครงสร้างภายในเซลล์ 14% ที่อัตราการไหล 0.3 มิลลิเมตรต่อนาที เมื่อพิจารณาผลของแบบจำลองคณิตศาสตร์พบว่าความเค้นเฉือนในระบบอุปกรณ์ที่ออกแบบแล้วมีอิทธิพลสูงกว่าความเค้นดึง และเกิดขึ้นตรงบริเวณใกล้ผนังท่อ เป็นเวลานานจนครอบคลุมตลอดความยาวของท่อ จึงทำจำนวนเซลล์บิดเบี้ยวมากและเซลล์ตายได้ ในขณะที่ระบบอุปกรณ์ที่ท่อหลอด-ท่อขยาย ความเค้นดึงมีอิทธิพลสูงกว่าความเค้นเฉือน และเกิดขึ้นตรงบริเวณมุมในช่วงที่ท่อเปลี่ยนหน้าตัด อย่างไรก็ตาม การไหลมีความเร็วสูงทำให้เซลล์ไหลผ่านในระยะเวลาสั้น แต่เนื่องจากขนาดของความเค้นดึงสูงมากและครอบคลุมพื้นที่เกือบเต็มหน้าตัดท่อในบริเวณดังกล่าว จึงทำให้เซลล์ที่มีโครงสร้างภายในถูกทำลายเป็นจำนวนมากและเซลล์ตายได้ ดังนั้นระบบที่ออกแบบแล้วและต่อหลอด-ท่อขยาย จะทำให้เซลล์เสียหายไม่เหมือนกันด้วยความเค้นคนละประเภทกัน ในงานส่วนที่สองได้นำระบบอุปกรณ์ที่ออกแบบแล้วและหลุมจุลภาคแบบสามเหลี่ยมมาบูรณาการเข้าด้วยกัน และทดสอบระบบด้วยอนุภาคพลาสติกและเซลล์มะเร็งผิวหนังตามลำดับ การทดสอบสมรรถนะของการคัดแยกอนุภาคพลาสติกขนาด 10, 15 และ 20 ไมโครเมตร พบว่าเมื่ออัตราการไหลเพิ่มขึ้นจาก 0.2, 0.5, 1 และ 2 มิลลิเมตรต่อนาที อนุภาคขนาด 10, 15 และ 20 ไมโครเมตร เกิดการเคลื่อนที่เข้าหาผนังด้านในมากขึ้น และไหลออกไปที่ห้องดักจับที่มีหลุมจุลภาคหมายเลข 3, 2 และ 1 ในขณะอัตราการไหล 0.5 มิลลิเมตรต่อนาที เป็นอัตราการไหลที่สามารถดักจับอนุภาคได้สูงสุด และพบว่าอนุภาคขนาด 15 ไมโครเมตรถูกดักจับที่ห้องดักจับที่สามถึง 80% ดังนั้นอัตราการไหลนี้จึงน่าจะดักจับเซลล์ที่มีขนาดประมาณ 15 ไมโครเมตรได้ดี และถูกใช้ในการทดลองสำหรับเซลล์มะเร็งผิวหนัง ซึ่งพบว่าเซลล์มีชีวิตรอด 74% และหลังจากนำเซลล์ไปเลี้ยงในหลุมจุลภาคต่อเป็นเวลาสามวัน พบว่าเซลล์มีชีวิตรอดเหลือ 68% ที่อัตราการไหลของสารอาหาร 10 ไมโครลิตรต่อชั่วโมง

จุฬาลงกรณ์มหาวิทยาลัย  
CHULALONGKORN UNIVERSITY

สาขาวิชา	วิศวกรรมเครื่องกล	ลายมือชื่อนิติศ
ปีการศึกษา	2563	ลายมือชื่อ อ.ที่ปรึกษาหลัก .....
		ลายมือชื่อ อ.ที่ปรึกษาร่วม .....

# # 5971419221 : MAJOR MECHANICAL ENGINEERING

KEYWORD: MICROFLUIDICS, SORTING, TRAPPING, CULTURING,  
EXTENSIONAL STRESS, SHEAR STRESS, EXPOSURE TIME

Thammawit Suwannaphan : Development of an Integrated Microfluidic System for Cell Sorting and Trapping—Considering Sorting Efficacy and Cell Viability.  
Advisor: Assoc. Prof. ALONGKORN PIMPIN, Ph.D. Co-advisor: Wutthinan Jeamsaksiri, Ph.D.

This study is divided into two phases. The first phase is about the investigation of cell viability and damage of white blood cells after sorting in both a spiral microchannel and contraction and expansion array (CEA) at appropriate flow rates for cell separation. Three techniques such as Trypan Blue staining, Scanning Electron Microscopy (SEM) and Wright-Giemsa staining are employed in the experiments. After flowing the sample through a whole setup of spiral microchannel at 2 ml/min, 85% of cells are viable while 30% of cells are significantly deformed and 2% of cells are seriously damaged in their intracellular structures. In CEA experiments, they are 89, 12 and 14%, respectively, at 0.3 ml/min. Considering computational results of flow dynamics at the same conditions, shear stress dominates over extensional stress in the spiral microchannel covering the entire length of the channel close to the walls with long exposure time. This may cause cell death and significant deformation. On the other hand, extensional stress dominates in the CEA and occurs at the corner where the cross-section of the flow channel changes. Despite of short exposure time due to high flow rate, the extensional stress with extremely high magnitude covers almost entire the cross-section of the flow channel. It potentially causes intracellular damage to the cells, and cell death. Therefore, the spiral microchannel and CEA cause cell damage in different ways due to the different types of stresses. The second phase demonstrates the integrated microfluidic device combining with the spiral microchannel and triangular wells together. The system is tested with microbeads and mast-cell-tumor (MCT) cells. When the flow rate increases in the range of 0.2, 0.5, 1 and 2 ml/min, the 10, 15 and 20  $\mu\text{m}$  microbeads gradually move towards the inner wall at the outlet of the spiral channel, and comes in the 3<sup>rd</sup>, 2<sup>nd</sup> and 1<sup>st</sup> chamber of microwells. At the flow rate of 0.5 ml/min, the maximal percentage of the trapping for 15  $\mu\text{m}$  microbeads is found at 80% in the 3<sup>rd</sup> chamber. Regarding this reason, this flow rate is used in the cell experiments since the size of MCT cells is about 15  $\mu\text{m}$ . When sorting the MCT cells at this flow rate, cell viability is 74%. After culturing in the microwells for three days, cell viability is 68% when the continuous flow of nutrient is fed at 10  $\mu\text{l/hr}$ . The results show the feasibility of the developed system in biological applications.

Field of Study: Mechanical Engineering  
Academic Year: 2020

Student's Signature .....  
Advisor's Signature .....  
Co-advisor's Signature .....

## ACKNOWLEDGEMENTS

Firstly, I would like to express my sincere gratitude to my advisor Prof. Alongkorn Pimpin for the continuous support of my Ph.D. study and related research, for his patience, motivation, and immense knowledge. His guidance helped me in all the time of research and writing of this thesis. I could not have imagined having a better advisor and mentor for my Ph.D. study.

Besides my advisor, I would like to thank the rest of my thesis committee: Prof. Werayut Srituravanich, Prof. Achariya Sailasuta, Prof. Saran Salakij and Prof. Vejapong Juttijudata for their insightful comments and encouragement, but also for the hard question which incited me to widen my research from various perspectives and Dr. Wutthinan Jeamsaksiri who provided me to access to the laboratory and research facilities for microfluidic devices and introduced me to the scholarship of TGIST.

A very special gratitude goes out to all down at the scholarship from Thailand Graduate Institute of Science and Technology (TGIST), Chulalongkorn Academic Advancement into Its 2nd Century Project (Smart Medical Device) and The 90th Anniversary of Chulalongkorn University Scholarship for helping and providing the funding for the work. Without their precious support, it would not be possible to conduct this research.

I thank my fellow labmates: Thanapat Chunfong, Pachara Noosawad and Thiwa Nantapak for the stimulating discussions for helping SOLIDWORKS program and simulation of COMSOL and for the sleepless nights, we were working together before deadlines, and for all the fun we have had in the last four years.

I would like to thank my life-coach: Siriporn Taylor (my godmother) who has also been generous with her love and encouragement despite the long distance from the USA.

Last but not the least, I deeply thank my parents, Witaya Suwannaphan and Daranee Attachoo for their unconditional trust, timely encouragement, and endless patience. It was their love that raised me up again when I got weary.

Finally, I would like to thank myself who never thought that this man could really come this far from a student who was really shy and always sat in the back row of the class to a Ph.D. who stands and teaches students in front of the class.

Thammawit Suwannaphan

## TABLE OF CONTENTS

	<b>Page</b>
ABSTRACT (THAI) .....	iii
ABSTRACT (ENGLISH).....	iv
ACKNOWLEDGEMENTS .....	v
TABLE OF CONTENTS.....	vi
List of Figure.....	1
List of Tables .....	5
Chapter 1 Introduction .....	6
1.1 Importance and Rationale.....	6
1.2 Reviews of Cellular Stress Responses .....	9
1.3 Reviews of the Effects of Shear Stress on Cellular Changes .....	10
1.4 Reviews of the Effects of Extensional Stress on Cellular Changes.....	13
1.5 Reviews of Spiral Microchannel.....	14
1.5.1 Progress in spiral microchannel using a classic spiral .....	14
1.5.2 Progress in spiral microchannel with different geometry designs .....	19
1.6 Reviews of Contraction-Expansion .....	25
1.7 Reviews of Microfluidic Integration.....	30
1.7.1 Optics.....	30
1.7.2 Magnetophoresis .....	31
1.7.3 Dielectrophoresis.....	32
1.7.4 Acoustophoresis .....	33
1.7.5 Hybrid techniques.....	33
1.7.6 Integrated microfluidics for monitoring and detection.....	34
1.7.7 Integrated microfluidics with other techniques. ....	34
1.8 Summary and Approach .....	35
Chapter 2 Spiral Microchannel and Contraction-Expansion Array.....	36

2.1 Design and Fabrication .....	36
2.2 Experiment.....	38
2.2.1 Test Methods .....	38
2.2.2 Feeding System and Test Conditions .....	43
2.2.3 Spiral Microchannel and Test Conditions .....	43
2.2.4 Contraction-Expansion Array (CEA) Systems and Test Conditions .....	44
2.3 Simulation.....	45
2.3.1 Simulation of Feeding System .....	45
2.3.2 Simulation of Spiral Microchannel .....	48
2.3.3 Simulation of Contraction-Expansion Microchannel Array .....	50
2.4 Results.....	52
2.4.1 The Results of Feeding System .....	52
2.4.2 The Results of Spiral Microchannel .....	55
2.4.3 The Results of Contraction-Expansion Microchannel Arrays .....	58
2.4.4 The Summary of Spiral Microchannel and Contraction-Expansion Array .....	59
Chapter 3 Microfluidic Integration .....	62
3.1 Design and Fabrication .....	62
3.2 Experiment.....	65
Mast cell tumor cell line (LuMC) .....	67
3.3 Results.....	70
3.4.1 The Results for Polystyrene Beads.....	70
3.4.2 The Results for Fibroblast (STO Mouse Fibroblast Cells).....	75
3.4.3 The Results for Mast Cell Tumor Cell Line (LuMC) .....	81
3.4.4 The Summary of Integrated Microfluidic Device .....	83
Chapter 4 Conclusions and Discussion.....	84
4.1 Conclusion for Feeding System, Spiral Microchannel and CEA .....	84
4.2 Conclusion for Integrated Microfluidic Device.....	85
4.3 Discussion.....	86



Appendix A Sample Preparation .....	88
A1. Preparation for RBC Lysing Solutions (10X concentration).....	88
A3. Leukocyte Preparation for Cell Suspension.....	88
A4. Biological Specimen Preparation for SEM.....	88
A5. Blood Smear.....	89
A6. Biological Specimen Preparation of Wright's Stain.....	89
A7. Fibroblast Preparation of Cell Suspension.....	89
A8. Media Preparation for Mast Cell Tumor Cell Line (LuMC) .....	89
A9. Media Solution Procedure.....	90
A10. Mast Cell Tumor Cell Line (LuMC) Preparation for of Cell Suspension .....	90
Appendix B Cell Enumeration.....	91
B1. Cell Enumeration Protocols for Hemocytometer.....	91
B2. Cell Concentration Formula.....	91
B3. Percentage of Cell Viability Formula .....	91
B4. Percentage of trapping distribution in a chamber .....	92
B5. Percentage of sorting efficacy in a chamber .....	92
REFERENCES .....	93
VITA.....	101

## List of Figure

<p>Figure 1.1 Several applications using a classic spiral micorchannel to (a) prove the concept of spiral microfluidic study based on the principle of lift and Dean drag force [32], (b) separate tumor cells (neuroblastoma and glioma cells) [38], (c) separate blood cells from plasma [41]. (d) separate stem cells (single cells from clusters) [44], (e) separate sperm cells from WBCs [46], (f) separate non-spherical shapes of phytoplankton [47].....</p>	17
<p>Figure 1.2. Spiral micorchannel with (a) the trapezoidal cross section [52], (b) stair-like cross section [56], (c) double spiral microchannel for tumor cell separation [57], (d) cascaded spiral microchannel for CTCs isolation [59], (e) two spiral channels and one zigzag channel [60], (f) the triplet parallelizing spiral microfluidics for tumor separation [61], (g) multiplexed spiral microfluidics [62] and (h) the modified outlets [65].....</p>	22
<p>Figure 1.3 The contraction-expansion regions were designed with (a) rectangular structures placed along the side microchannel [68], (b) axisymmetric multi-orifice cahmbersn [69], (c) symmetric chambers with siphoning channels [71] and (d) alternating pattern of reservoirs for rare cell isolation [74]. ....</p>	27
<p>Figure 1.4 The contraction-expansion regions were designed with (a) right angled isosceles triangular cavities (b) asymmetrically patterned half circular cavity arrays (c) asymmetrically patterned diamond cavity arrays [75], (d) High-rectangle (e) Low-rectangle (f) Circle and (g) Streamline cavity arrays [77]. ....</p>	28
<p>Figure 2.1 Schematic drawing (not draw to actual scales) and actual device of (a) spiral microchannel and (b) contraction-expansion array.....</p>	37
<p>Figure 2.2 Process flow of PDMS fabrication by Etching.....</p>	37
<p>Figure 2.3 An assembled microfluidic device—spiral microchannel (left) and CEA (right) with bonding the PDMS on a slide glass or PDMS .....</p>	38
<p>Figure 2.4 Cell features were observed under a light microscope—viable cells (blue arrows) and non-viable cells (red arrows) .....</p>	39
<p>Figure 2.5 Normal cells observed using SEM .....</p>	40
<p>Figure 2.6 Degenerated cells observed using SEM .....</p>	41
<p>Figure 2.7 Example the image of normal (blue arrow) and degenerated cells (red arrow) observed using SEM.....</p>	41
<p>Figure 2.8 Normal cells (blue arrow) and degenerated cells (red arrow) observed using Wright-Giemsa stain .....</p>	42

Figure 2.9 Schematic drawing of feeding system: syringe, needle and silicone tubes. .....	44
Figure 2.10 Schematic drawing of complete setup of spiral microchannel devices and the setup of spiral microchannel including feeding system: syringe, silicone tubes, needle and spiral microchannel: straight channel and outlets.....	44
Figure 2.11 Schematic drawing of the complete setup of contraction–expansion microchannel array: feeding system and CEA.....	45
Figure 2.12 Picture of (a) Geometry of syringe with revolving and (b) Corner refinement and Distribution function.....	47
Figure 2.13 Example of contour—total extensional and shear component of stress tensors, the maximum stresses exerted at the corner of syringe.....	47
Figure 2.14 Picture of (a) Spiral microchannel and (b) straight and 10 outlets.....	49
Figure 2.15 Example of contour—total extensional and shear component of stress tensors in the spiral channel, the maximum stresses exerted at the walls of the channel. ....	49
Figure 2.16 Picture of CEA: symmetry domain in x-z axis (left) and symmetry domain in y-z axis (right).....	50
Figure 2.17 Geometry of CEA’s chamber with corner refinement and distribution function. ....	51
Figure 2.18 Example of contour—total extensional and shear component of stress tensors in the CEA’s chamber, the maximum stresses exerted at the corner of CEA..	51
Figure 2.19 Percentage of cell viability, cell morphology and intracellular structures in feeding system with increasing flow rates.....	52
Figure 2.20 Paths of cell movement with the magnitude of extensional and shear in r-axis: total extensional and shear components of stress tensor (path 1) at (a) 1 ml/min (b) 8 ml/min and average total extensional and shear components of stress tensor along with four different paths at (c) 1 ml/min and (d) 8 ml/min ( $r = 0$ at the centerline of syringe and $Z = 0$ at the bottom of syringe’s barrel). ....	54
Figure 2.21 Vortices in a spiral microchannel drive cells travelling in six different locations leading to cell deformation (a) extensional stress and (b) shear stress at 2 ml/min.....	55
Figure 2.22 Magnitude of total extensional and shear components of stress tensor (a) at 2 ml/min (b) at 10 ml/min, along with a streamline in the middle of channel and average total extensional and shear components of stress tensor (c) at 2 ml/min and	

(d) at 10 ml/min along with nine different paths of the streamlines in one loop of spiral (0–360°). .....	56
Figure 2.23 Contraction and expansion chamber at the corner. (a) Contour of extensional stress and high stress area, (b) the magnitude of total extensional and shear component of stress tensor and the height of chamber in Y-axis (path 1) and (c) the magnitude of average total extensional and shear components of stress tensor with four paths of streamlines ( $Y = 0$ , at the centerline of the main channel).....	59
Figure 3.1 The schematics design of the device (a) the integrated microfluidic device (b) spiral microchannel part (c) expanded channel and outlets (d) trapping chamber with 21 microwells (e) microwells and (f) spheroid in a microwell.....	63
Figure 3.2 Schematic picture of (a) process flow of PDMS fabrication and (b) microfluidic assembly.....	64
Figure 3.3 The design of stage for helping focusing objectives .....	64
Figure 3.4 Setup of the integrated microfluidic device (a) schematic drawing setup and (b) actual setup under a light microscope .....	65
Figure 3.5 The setup of integrated microfluidics.....	66
Figure 3.6 Experiment in the injection made for investigating trapping distribution and sorting efficacy.....	66
Figure 3.7 Experiment in the withdrawn mode for cell culture (a) schematic drawing (b) the actual setup of microfluidic integration.....	67
Figure 3.8 Introducing the cells without passing through the spiral part (a) flowing the cells with the volume of 3 ml at 5 <sup>th</sup> and 4 <sup>th</sup> outlets and (b) switching and introducing the cells with the another volume of 3 ml at 1 <sup>st</sup> and 2 <sup>nd</sup> outlets.....	68
Figure 3.9 Surface roughness was caused by machining from CNC process on the side of equilateral triangular well.....	69
Figure 3.10 Observation of particles of 10, 15 and 20 $\mu\text{m}$ under a light microscope .	70
Figure 3.11 Percentage of trapping distribution in chambers at (a) 0.2, (b) 0.5 (c) 1 and (d) 2 ml/min.....	72
Figure 3.12 Percentage of sorting efficacy (counting particles—wells, surface and outlets) in chambers at 2 ml/min.....	72
Figure 3.13 Percentage of particle trapping in each row of the 3 <sup>rd</sup> chamber at 0.5 ml/min.....	74

Figure 3.14 Example of mixtures of particle of 10 $\mu\text{m}$ , 15 $\mu\text{m}$ and 20 $\mu\text{m}$ were trapped in wells—the largest size of beads were trapped in the front and the smaller size were trapped in the back well. ....	74
Figure 3.15 Schematic picture of (a) free body diagram of a particle moving to a surrounding fluid (b) trajectory of projectile in a well and (c) trajectory of projectile in a chamber.....	75
Figure 3.16 Measurement of fibroblast sizes on a hemocytometer with a microscopy program.....	76
Figure 3.17 Percentage of STO viability—Control (blue), Day1 (red), Day3 (green) and Day3 without passing through the spiral part (yellow). ....	77
Figure 3.18 Percentage of STO trapping distribution in all chambers at 0.5 ml/min ..	78
Figure 3.19 Percentage of cell trapping in the rows of the 3 <sup>rd</sup> chamber at 0.5 ml/min. ....	78
Figure 3.20 Spheroid formation of STO in well (a) Day1, (b) Day3 in equilateral triangular microwell and (c) Day1 and (d) Day3 in the diamond pyramidal microwell [Thanapat Chunfong] .....	79
Figure 3.21 Influence of vortices in each row affecting the trapping distribution .....	80
Figure 3.22 Influence of vortices in each row affecting STO formation.....	80
Figure 3.23 Sizes of LuMC cells are measured under a light microscope .....	81
Figure 3.24 Percentage of LuMC viability—Control (blue), Day1 (red), Day3 (green) and Day3 without passing through the spiral part (yellow). ....	82
Figure 3.25 Mast cell tumor cells (LuMC) (a) Day1 and (b) Day3 and mouse fibroblasts (STO) .....	82

## List of Tables

Table 1.1 Summarization of shear stress over the past decades .....	12
Table 1.2 Summarization of the studies of extensional stress that affects various types of cells.....	14
Table 1.3. Progress in conceptual proof of spiral microfluidic studies using particle matter. ....	15
Table 1.4 Progress in spiral microfluidics separating cellular matter—cancer cells, blood cells, stem cells and others.....	18
Table 1.5. Progress of several designs of spiral microchannel for specific applications. ....	24
Table 1.6. Progress in several designs of contraction-expansion arrays for specific applications .....	29
Table 2.1 Dimension of actual syringes of 1, 2.5 and 5 ml. ....	46
Table 2.2 Summarization of cell loss and damage for each component.....	60
Table 3.1 Volume of sample was collected at the five outlets for four sets .....	69

# Chapter 1

## Introduction

### 1.1 Importance and Rationale

Cancer is defined as unwanted and uncontrolled growth of cells in human body. Among deadly diseases, cancer is one of the most feared illnesses and it can be non-infectious or non-communicable disease. There are several causes of being cancer including smoking, drinking, eating habit, pollution, infection and inherited genes. According to the Ministry of Public Health, cancer is the second leading cause of death globally and the statistics demonstrated over 8.8 million deaths in 2015 [1]. On the other hand, cancer is the first leading cause of death in Thailand. About 60,000 patients die from cancer in Thailand and the numbers of new patients seem to increase gradually every year [2]. Additionally, as reported by World Health Organization, 8.2 million people die from cancer all over the world each year and will reach to 19 million patients by the year of 2025 [3]. Surprisingly, if we look at the numbers of statistics closely, cancer is one of the most lethal diseases not only in Thailand but also in other countries. To decrease the numbers of deaths, it is essential to initially and fully understand fundamental knowledge of cancer. Therefore, we will be able to diagnose the causes of cancer accurately and give patients treatment appropriately and properly.

Over the past decades, microfluidic technology has thrived and flourished in the field of medical diagnostics and has a bright future in the field of medical treatment as well. Because of portability, inexpensiveness, high throughput, less sample used and simplicity, microfluidic technology have been attracted attentions and invented for several researchers. In several applications, microfluidic technology has a great potential to help diagnosing and analyzing cell biology including RBCs, WBCs, sperms, mammalian cells, plant cells, MCTs, CTCs and spheroid (fibroblast) analysis and provide precise and accurate results with a high efficiency of the device. For this, microfluidic technology is one of the most potential approaches that could allow us to understand the fundamental knowledge in biology especially cancer cell behavior.

Nowadays, the recent advancement in microfluidics research is the implementation and integration of several microfluidic techniques with multiple functions onto a single chip which is known as Lab-On-a-Chip (LOC). Over the past years, the microfluidic systems requiring assembly and fluidic interconnection among other components have been produced in a number of applications and they have been proven to be appropriate for a variety of biological and chemical applications

Several integrated microfluidic devices would combine with other techniques—active or passive technique including hydrodynamics, optics, magnetophoresis, dielectrophoresis, acoustophoresis which provides the convenience of operation with multiple functions in one process than a single technique alone. Not only were single cells tested by microfluidic integration but spheroids were also examined in terms of cell culture study and drug resistance. Therefore, the study of

microfluidic integration has played an important role in biological diagnostics as well as having a great potential to single cell, cluster and spheroid for the study of cancer behavior.

Over the past years, mechanical engineers and doctors in Veterinary Science at Chulalongkorn University have cooperated and dedicated on this research to develop advanced technology to help diagnosing and analyzing a single cell/spheroid known as Microfluidics. Thailand Micro Electronics Center (TMEC) has also supported us with facility and fabrication including sorting and trapping chip. Beside the development of microfluidic device, we have also achieved the integration of microfluidics by integrating the previous microfluidic devices together—sorting and trapping device consisting of three functions—sorting, trapping and culturing. This device could separate cells as single cells based on their sizes and then trap them separately in the individual wells to observe their motion, trajectory and degree of freedom. Finally, trapped cells will be cultured continuously for the study of cell proliferation, division, differentiation and further analysis of cells either single cells, clusters or spheroids.

Besides the developing efficiency of microfluidic devices, prolonging cell viability is also really crucial in microfluidic study. According to the studies of cell damage, the loss of cell, intracellular and extracellular changes depend on various exogenous factors—shear and extensional stress from fluid flow and the cell ability to handle stresses. Thus, the causes of cell loss and cellular changes from stresses will be investigated as well as the sorting efficacy and trapping distribution will be investigated. The novel of integrated microfluidic device will be designed and fabricated focusing on sorting efficacy and trapping distribution as well as prolonging cell viability and preventing cells from physical and biological damage.

As we mentioned above, this thesis is divided into two phases. In the first phase, we present the investigation of shear and extensional stress affecting cell viability and the change in cell morphology and intracellular structures in the setup of two sortors—spiral microchannel and CEA device. The setup of spiral microchannel is examined including a feeding system, i.e. syringe, silicone tube, and spiral microchannel as well as the contraction-expansion microchannel array (CEA) is also tested including feeding system and CEA part. WBCs are used as experimental sample due to a wide range of cell's sizes (7-12  $\mu\text{m}$ ) and a good biomarker. The experiment of WBCs is examined with three methods including Trypan Blue stain, Scanning Electron Microscopy (SEM) and Wright-Giemsa stain under various conditions. To improve more understanding of stresses and other factors, the experiments are investigated together with computational simulation to explain some phenomena that happen in our setup of both spiral microchannel and CEA device. In second phase, the integrated microfluidic device—sorting and trapping is designed based on the previous knowledge and then fabricated. The integrated microfluidic device is investigated the sorting efficacy and trapping distribution in each chamber and row in different sizes of microbeads (10  $\mu\text{m}$ , 15  $\mu\text{m}$  and 20  $\mu\text{m}$ ) and examined with actual cells—STO and LuMC ( $\sim 15 \mu\text{m}$ ). Finally, the investigation of cell culture is also taken place in the last part with both STO and LuMC cells as well as evaluating cell viability before, after flowing through the device and three days of cell culture in comparison.



We strongly believe that in this acknowledge, we will be able to better understand physical changes affected by stresses including cell viability and cellular damage. Furthermore, a new fully integrated technique will provide huge advantages for several studies including cell culture study, drug resistance and physical-biological analysis. Ultimately, this knowledge will also serve a better understanding of cancer cell behavior to researchers and doctors that help potentially save more peoples' lives from cancer in the future.

### Objectives

1. Studying and investigating the effects of stresses on WBCs including cell viability, cell morphology and intracellular structures with experimenting and computational simulation in both spiral microchannel and contraction-expansion microchannel array.

2. Comparing both the efficacy of the spiral microchannel and contraction-expansion microchannel array and then choosing the appropriate one to be integrated with the triangular microwell to complete a clinical application for cell sorting, trapping and culturing as Lab-On-a Chip.

### Research Plans

Protocols	Year 1 (2017)						Year 2 (2018)					
	1 <sup>st</sup> Semester			2 <sup>nd</sup> Semester			1 <sup>st</sup> Semester			2 <sup>nd</sup> Semester		
	Aug -Sep	Oct- Nov	Dec- Jan	Fab- Mar	Apr- May	Jun- Jul	Aug -Sep	Oct- Nov	Dec- Jan	Fab- Mar	Mar -Apr	Jun- Jul
Literature Review	←————→											
Study Parameters and Experiment	←————→											
Repeated Experiment of Feeding and Spiral				←————→								
Simulation of CEA									←→			
Experiment of CEA										←→		
International Conferences	←→					←→	←→					←→

Protocols	Year 3 (2019)						Year 4 (2020)					
	1 <sup>st</sup> Semester			2 <sup>nd</sup> Semester			1 <sup>st</sup> Semester			2 <sup>nd</sup> Semester		
	Aug -Sep	Oct- Nov	Dec- Jan	Fab- Mar	Mar -Apr	Jun- Jul	Aug -Sep	Oct- Nov	Dec- Jan	Fab- Mar	Mar -Apr	Jun- Jul
Integrated sorting and trapping	←————→											
Examination with beads and cells			←————→									
Improving the efficiency						←————→						
Data Analysis										←————→		

## 1.2 Reviews of Cellular Stress Responses

After reviewing the past several studies of cellular shear stress responses, the effects of shear stress on cell viability could be categorized into 5 main indicators in general. Here, these five indicators—loss of viability, membrane integrity, release of intracellular components, morphological variations and metabolism will be discussed in this section.

Loss of viability or cell death is related to cell lysis because it is the most extreme response of cells to an imposed hydrodynamic stress [4]. Cell death has many forms including apoptosis, necrosis, pyroptosis and autophagic. As for Apoptosis, it is considered as programmed forms of cell death which is associated with biochemical and morphological changes. It could be observed as shrinkage and blebbing of cells. On the other hand, Necrosis term is used and associated with the loss of control ionic balance, uptake of water, swelling and cellular lysis [5]. According to the studies of Ma et al., McQueen et al. and Zhang et al., they investigated shear stress using the capillary to measure the order of stress. They found that the stress affecting on necrotic cell death was about 100-240 Pa. Other researchers also confirmed that stresses could trigger cells to be Apoptosis and Necrosis causing cells to die [6-10]. Another experiment by Tanzeglock et al. showed that the order of 0.59 Pa did not cause HEK cells to die. However, necrosis and permanent deformation of cells occurred when hydrodynamic stress was 2.09 Pa [6].

Membrane integrity, it is an indicator that can evaluate the loss of viability. One of the most commonly approaches of measuring membrane integrity is a trypan blue dye exclusion test. The numbers of viable and dead cells are measured microscopically using a hemocytometer. Because it is easy to test and able to measure dead cells immediately, so that, trypan blue dye exclusion test becomes our primary method to examine cell viability in this work. In addition, membrane integrity in plant cells could be measured by using dielectric spectroscopy [4].

Release of intracellular components—enzyme is used as an indication of cell lysis. It is frequently evaluated in suspending fluid, known as the release of lactate dehydrogenase (LDH). Petersen et al. reported the relation between the release of LDH, cell viability, magnitude of stress and exposure time. Chittur et al., Tramper et al. and Goldlum et al. also investigated the effects of stress evaluated by the release of lactate dehydrogenase [11-14].

Morphological variation is one of the indicators measuring the deformation of cell that are associated with the hydrodynamic environment. Tanzeglock et al. examined the shear and extensional stress affecting on cell death measuring morphological changes that decrease in cell size and increase in cell granularity [6]. Similarly, the experiment of Stathopoulos and Hellums also observed and measured the change of cell morphology as an indicator. Sato et al. demonstrated shear stress on cells on the micropipette aspiration technique. The samples were exposed to the shear stress about 1, 3, 8.5 Pa for 0.5 to 24 hours and showed photomicrographs to observe morphological variation [15].

Metabolic indicator such as respiration activity, it is one of the responses that has been shown to be a sensitive indicator. The respiration is caused by intracellular enzymes or organelles affected by stresses. Metabolic indicator such as the reduction of tetrazolium salt in the mitochondria of living cell is also indicated the indirect evaluation of cell viability [4]. One of the experiment by Abu-Reesh and Kargi showed both laminar and turbulent shear stress affecting biological functions such as respiration activity [16].

As can be seen from the above studies, hydrodynamic stress plays a remarkable role in biological and physical damage. With low stresses, cells tends to change in biological function such as growth rate, cellular volume, metabolism and membrane permeability. In contrast, with a high stress, cells are be affected physically including cell lysis, membrane integrity and cell morphology causing the loss of cell viability [17]. To have a better understanding of stresses affecting cells, the past studies of cellular responses with different types of stress will be discussed in details in the next section including the types of stresses, types of cells, magnitude of stresses, exposure time with different approaches.

### **1.3 Reviews of the Effects of Shear Stress on Cellular Changes**

The effects of shear stress and interfacial phenomena on cell viability of both animal and plant cells have been drawn a great attention to several researchers. In these reviews, there are several approaches including viscometer, cone plate apparatuses, flow channel assemblies and capillary recirculation systems are utilized to measure shear stress on various types of cells—animal and plant cells. Furthermore, exposure time, shear stress and more information of biological and physical changes are also provided in this review.

In the study of Nevaril et al. red blood cells (RBC) were tested by Couette viscometer. The results showed that hemolysis appeared with shear stress around 150-300 Pa [18]. Leverett et al. performed the effect of hemolysis in high and low shear stresses. They found that applying low stresses with short exposure time, it could cause a little damage on cells. However, above threshold of 150 Pa, extensive cell damage was observed with high stresses (300 Pa) and short exposure time caused cells to be ruptured severely [19]. Furthermore, turbulent flow was extensively studied by Sutura and Mehrjardi in turbulent Couette flow. The results demonstrated that RBC suspension sheared about for 4 minutes and increasing shear stress from 10 to 450 Pa resulting in the deformation of RBCs and RBCs become fragmented at shear stress about 250 Pa [20]. Sallam and Hwang also studied shear stress and the effects on RBCs. When shear stress was further increased to 400 Pa, it was found that RBC hemolysis was increased as well [21]. Additionally, besides types of cells, the age of the blood also has effects on cell resistance. For example, fresh blood is more robust than old blood [22].

Hybridoma Cell is another sample that has been tested for many researches. Smith et al. showed the investigation of shear sensitivity including cell viability, lactate dehydrogenase and cell morphology on mouse hybridoma cells using Couette viscometer for 15 hours. The results indicated that cell damage was observed at the shear stress about 0.67 Pa with releasing LDH and cell viability reduced from

85% to 70% but the change in morphology was not found [9]. The study of Petersen et al. reported the order of stress affecting hybridoma cells including cell viability and the release of LDH from 0 to 5 Pa with exposure time from 0 to 10 minutes [14]. Similarly, Schürch et al. et al. investigated shear stress on hybridoma cells (myeloma line P-3X63-Ag8) using a rotating viscometer. The results showed that the loss of cell viability started being appeared at the shear stress of less than 6 Pa [23]. Abu-Reesh and Kargi experimented both laminar and turbulent shear stress affecting cell viability and at different levels and exposure time. Above threshold of shear stress at 5 Pa in turbulent flow resulted in 50% loss of cell viability [16]. The above studies can be suggested that in order to keep hybridoma cells viable and functional, shear stress should be lower than 5 Pa.

Insect cells are considered as the most shear sensitive cells. Tramper et al. studied shear sensitivity of insect cells with *Spodoptera frugiperda* (SF-21) in a Haake viscometer. The results demonstrated that the cells started losing their viability when shear stress reached to 1 Pa and about 50% loss of viability when shear stress increased to 1.5 Pa for 3.5 hours [12]. Goldblum et al. also investigated shear stress in a modified Weissenberg R-16 rheogoniometer using *Trichoplusia ni* (TN-368) and *S.frugiperda* (SF-9) cells as cell suspension. TN-368 and SF-9 were affected by shear stress with the magnitude of 0.12 and 0.59 Pa for 5 minutes [13].

Beside insect cells, other animal cells are also investigated in several approaches. Augenstein et al. investigated wall shear stress on mouse (L929) and human (HeLaS3) cells utilizing a capillary system. The results showed cell death observed in a typical experiment that cells were pumped through a test capillary. The investigation was found that mouse cells were more sensitive than human cells at the wall shear stress of 100 Pa for 0.5 s [24]. Similarly, McQueen et al. utilized their device produced turbulent flow in contraction to study the effect of shear stress on mouse myeloma cells. The evidence indicated that cell lysis was obviously observed with above threshold wall shear stress of 180 Pa for 0.02 s [8]. The study of Dewitz et al. investigated the effect of shear stress on human leukocyte cells using concentric cylinder viscometer. The results demonstrated that the change in cell function appeared at the shear stress of 15 Pa [25]. Chittur et al. also demonstrated shear stress on human T lymphocyte cells. According to the study, the cells could withstand shear stress of up to 20 Pa for 10 minutes in a modified Couette viscometer [11]. Kretzmer and Schiigerl reported the magnitude of shear stress that affected the release of LDH and the loss of cell viability using baby hamster kidney cells (BHK 21 c13). The results indicated that shear stress about 0.16 Pa, the loss of cell viability was not found. However, the release of LDH was increasing into medium when increasing shear stress. The loss of cell viability was found after shear stress increased to 1.5 Pa [26]. Similarly, another experiment using BHK-21 by Luwing et al, found that the influence of shear stress about 4.5 Pa could affect morphology to spread after division [27].

Plant cells are one of the cell types that have been intensively studied over the past years. The main reason that allows plant cells are more robust than mammalian cells is that they have a thick cellulose-based cell wall. One of the examples of plant cell investigation is the study of Patricia. The study reviewed the effect of hydrodynamic stress on plant cell wall performed by bioreactors. According

to the review, plant cell wall allows cell to maintain turgor and tensile strengths in the order of 10-30 atm (1 atm = 101.325 kPa) [4].

Table 1.1 Summarization of shear stress over the past decades

Authors	Year	Sample	Methods	Magnitudes No effect cell viability (Pa)	Magnitudes of Cell death (Pa)	Exposure Time
Nevaril et al.	1968	RBCs	Viscometer	150-300 Hemolysis	-	2 min
Augenstein et al.	1971	Mouse (L929) and Human (HeLaS3) cells	Capillary System	100		0.5 s
Leverett et al.	1972	RBCs	Viscometer	150 Hemolysis	300	Short Time
Sutera et al.	1975	RBCs	Viscometer	<250 (Deformation) >250 (Fragmentation)		4 min
Dewitz et al.	1980	Human Leukocytes	Concentric Cylinder Viscometer	15 Altered Cell Function	-	-
Sallam et al.	1984	Human RBCs	Viscometer	400 (Hemolysis)	-	-
Carpita et al.	1985	Carrot	Gas decompression	-	$1-3 \times 10^6$	-
Tramper et al.	1985	Spodoptera frugiperda (SF-21)	Haake Viscometer	Lysis (0.113 % LDH)	1.5 (50% Loss Viability)	
Smith et al.	1987	Hybridoma	Viscometer		(420 s <sup>-1</sup> )	15 hrs
McQueen et al.	1987	Mouse myeloma	Capillaries	180 (lysis)	-	0.02s
Chittur et al.	1988	T cells, B cells and monocytes	Viscometer	10-20 the release of LDH, cellular enlargement and the membrane depolarization	-	-
Petersen v et al.	1988	Hybridoma Cells	Couette Viscometer	-	5	10 mins
Schurch et al.	1988	Hybridoma Cells	Rotating Viscometer	-	<6	-
Abu-Reesh et al.	1989	Hybridoma cells	Searle Viscometer	<5 (Respiration Activity) >5 (Loss of Membrane) >5 (Cell lysis)	>5 (50% Loss Viability)	0.5-2 hrs

As can be seen, cells have several forms of changes—physical and biological changes [5, 17]. The level effects of cell damage are various such as deformation, injury and lysis depending on cell types, forms of stress, magnitude of stress and exposure time. According to the above studies, plant cells are the most robust and animal cells are susceptible, especially insect cells because they have no cell walls and the size of insect cells, which are quite large compared to other types of cells. To have a better understanding of the effects of the shear stresses on different types of cells, Table 1.1 summarizes over the past decades of many of studies. To compare those past studies, we reported the studies in terms of magnitude of shear stress in Pascal with exposure time and types of cells that can withstand shear stress in different level of shear stress.

As mention above, although some studies of shear stress used the same type of cells in their research, the examined cells in different approaches would withstand shear stress in different order and respond to shear stress in different way. Therefore, the conclusion may not be made because the data of shear stress affecting on cells still have been limited and had relatively small number of applications to be proved. In addition, in the past, the studies of shear stress were intensively focused. However, nowadays, the studies of extensional stress are attracted attentions to the fact that extensional stress could potentially be the main cause of cell loss instead of shear stress.

#### **1.4 Reviews of the Effects of Extensional Stress on Cellular Changes**

Despite, the recent advancements of microfluidics, the investigation of extensional stress is still restricted, partially due to limitation in examining and measuring extensional stress directly. Furthermore, the new studies of stresses have questioned whether shear or extensional stress is dominant the cause of cell death. For this reason, it is necessary to review and collect data in the past studies to ensure that extensional stress is one of the major factors that cause cell to death rather than shear stress. In this section, the past studies of extensional stress will be reviewed narratively including magnitude of extensional stress, methods, types of cells and results.

The study of Tanzeglock et al. (2009) was one of the most first reviews of extensional and shear stress affecting on cells using rheometer and syringe. They discovered that extensional stress about 1.09 Pa caused cells to become apoptosis death for Human embryonic kidney (HEK) cells and 3.05 Pa for Chinese hamster ovary (CHO) cells while necrosis prevailed around 1 Pa in shear flow and 500 Pa in extensional flow [6]. Down et al. confirmed that extensional stress was developed at the capillary entrance. The results indicated that extensional stress may have a significant factor in contributing to failure of the RBC membrane and the damage threshold for hemolysis was about 3000 Pa, which could cause RBC trauma [28]. The study of Aguado et al. suggested that two factors that had the effect on cell loss were shear and extensional stress, especially extensional flow caused mechanical disruption in a syringe needle [29]. Yen et al. (2015) studied the effects of shear and extensional stress acting as the force behind hemolysis. The study suggested that extensional stress played a significant role in cell damage rather than shear stress and the threshold value of extensional stress was about 1000 Pa with the exposure time about 0.06 ms [30]. Bae et al. (2016) demonstrated the effects of extensional stress with Chinese hamster ovary (CHO) cells. CHOs were introduced and experienced the extensional stress at the middle of microfluidic cross-slot geometry channel. They discovered that the critical extensional stress that could damage cell mechanically was about 250 Pa [31].

As can be seen from the above mentioned studies, cells have several ways to respond to stress levels—physical and biological changes. The effects of cellular responses could be various, such as cell deformation, injury, lysis and loss depending on cell types, types of stresses, approaches, magnitude of stress and exposure time. However, the data of different types of cell that withstand stress differently and limited measurement techniques lead to different experimental results. Furthermore,

cellular heterogeneity also plays a significant role in different experimental results. Consequently, the above data cannot be clearly concluded due to insufficient data of stresses affecting cells. To have a better understanding of stress on cells, we summarize the data of extensional stress on cells including methods, types of cells, magnitude of stress and exposure time (Table 1.2).

Table 1.2 Summarization of the studies of extensional stress that affects various types of cells

Authors	Year	Sample	Methods	Magnitudes of Cell Damage (Pa)	Magnitudes of Cell Death (Pa)	Exposure Time
Tanzeglock et al.	2009	HEKs and CHO	Rheometer and Syringe	—	500	—
Down et al.	2011	Red Blood Cells	Capillary	—	3,000	ms
Aguado et al.	2012	—	Needle	—	—	—
Yen et al.	2015	Red Blood Cells	Capillary	—	1,000	0.06 ms
Bae et al.	2016	Chinese Hamster Ovary Cells	Cross-Slot	—	250	—

## 1.5 Reviews of Spiral Microchannel

### 1.5.1 Progress in spiral microchannel using a classic spiral

As a proof of concept of inertial focusing behavior, microbeads are frequently used as models for study and analysis of interest in particle migration because they mimic cellular samples with physical sizes similar to the cells. Bhagat et al. (2008) characterized a planar passive spiral microchannel device that could separate microbead mixtures (1.9 and 7.32  $\mu\text{m}$ ) and demonstrated both numerically and experimentally how Dean Force played an important role in separation [32]. Hasni et al. (2011) utilized a spiral microfluidic channel to sort large microbeads. In this work, 40 and 60  $\mu\text{m}$  polystyrene beads were tested. Polystyrene beads were started focusing at the flow rate of 1 ml/min while two focusing streamlines of 40 and 60  $\mu\text{m}$  occurred at 3 ml/min [33]. Martel and Toner (2012) also proved the concept of inertial focusing behavior in a spiral microchannel device of varying widths but fixing the height as well as discovered other parameters that affected inertial focusing behavior. Owing to the experiment, the inertial focusing behavior was successfully tested with microbeads of 10  $\mu\text{m}$  at flow rate of 1.6-2 ml/min [34]. Xiang et al. (2013) showed quantitative characterization of the focusing process and analysis of particle migration behavior in a five loop planar Archimedean spiral microchannel. The results suggested that two different sizes of the particles (2.1 and 4.8  $\mu\text{m}$ ) and rare particles were successfully separated using the spiral microchannel device [35]. Another study of Xiang et al. (2015) proposed an improved insight of particle migration and proposed a two stage process model of inertial focusing to understand the particle focusing process in a classic spiral microchannel device. The focusing and separation were performed with different-sized particles along the channel. The results illustrated

the quantitative characterization of the focusing and separation performances of mixed particles (5 and 10  $\mu\text{m}$ ) for guiding the design of multi-particle sorting devices [36]. Due to the limitation of particle focusing, particles with diameter of 5  $\mu\text{m}$  or above were used to study particle focusing behavior in microfluidics. However, Johnston et al. (2014) characterized inertial microfluidics using spiral microchannel to separate extremely small particles (1, 2.1 and 3.2  $\mu\text{m}$ ). The results depicted that the efficiency of cleaning up 1  $\mu\text{m}$  microspheres from 2.1 and 3.2  $\mu\text{m}$  was 93% and 87 %, respectively [37]. To ease of understanding, the summarization of conceptual studies is demonstrated in Table 1.3 as well as the different designs of spiral microchannel presented in Figure 1.1. As seen in the above data, many researchers have experimented and proved the concepts of spiral microchannel using microbeads to show the promise in terms of separating polymer particles because the physical property is similar to the cellular sample, however, it is still impractical for cellular analysis and biological studies.

Table 1.3. Progress in conceptual proof of spiral microfluidic studies using particle matter.

Authors/Year	Cross Section ( $\mu\text{m}$ )	Dimensions	Shape Size of Sample ( $\mu\text{m}$ )	Flow Rate	Max Velocity (m/s)	Special Remarks
<b>Bhagat et al. 2008</b>	W=100 H=50	Loops=5 Initial Radius=3mm Total Length=13cm	Microbeads =7.32,1.9	0.020 ml/min	0.067	
<b>Hasni et al. 2011</b>	W=500 H=220	Loops=5	Microbeads =40,60	3 ml/min	0.455	Separate Large Particles
<b>Martel et al. 2012</b>	W=50-400 H=50	Initial Average Radius=1500 $\mu\text{m}$ Final Average Radius=6000 $\mu\text{m}$ Total Length=6cm	Microbeads =10	1.6-2 ml/min	1.33	
<b>Xiang et al. 2013</b>	W=160	Loops=5 Initial Radius=3.5mm Total Length=16cm	Microbeads =4.8, 2.1	De =3.36		
<b>Johnston et al. 2014</b>	W=20 H=20	Loops=4 Initial Radius=2.12mm Total Length=82mm	Microbeads =1,2.1,3.2	0.01 ml/min	0.417	Separate Small Particles
<b>Xiang et al. 2015</b>	W=150 H=50	Loops=5 Total length=16cm	Microbeads =5,10	De = 12		

To show the applicability of devices for clinical applications, cellular samples have also been examined by a classic spiral microfluidics in several applications. One of the most popular examples is sorting targeted cells from undesirable cells such as separation of cancer cells from blood cells (RBCs or WBCs) or blood cells from



plasma. In 2009, inertial microfluidics for continuous particle separation using an Archimedean spiral microchannel to separate cancer cells—neuroblastoma and glioma cells was utilized by Kuntaegowdanahalli et al. (2009). This paper was reported for the use of Dean coupled inertial migration to sort samples. The data showed that the efficiency of cell separation was 80% with cell viability was >90% [38]. Thanomsridetchai et al. (2017) demonstrated the separation of natural Mast-cell tumor cells (MCTCs) using a spiral microchannel with low-aspect-ratio at 0.5-2 ml/min. Flow cytometric analysis reported that the efficiency of cell separation between 15 to 25  $\mu\text{m}$  was about 90% but the smaller particles of <5  $\mu\text{m}$  were not focused. In this work, before performing, the enumeration of cell viability was about 90-95%. However, the cell viability after performing was not calculated [39]. As for sorting of blood cells, Nivedita and Papautsky (2013) developed the spiral inertial microfluidic device for the separation of blood cells (WBCs and RBCs) from a diluted sample of blood with a flow rate of 2 ml/min. The spiral microchannel device showed the high separation efficiency of 95% with high viability of blood cells [40]. Xiang and Ni (2015) utilized an inertial microfluidic platform using spiral microchannel to investigate blood cell separation from plasma with the flow rate of 0.7 ml/min. As a result, the purity of blood isolation was close to 100% and plasma was 38.5% with over 98% viability of blood cells after running under the maximum flow rate of 0.7 ml/min [41]. Another research of Nivedita et al. (2017) using RBCs exhibited the investigation of secondary flow in a spiral microchannel with low aspect ratio. The data was found that secondary Dean vortices appeared when using a high flow rate (3 ml/min) and observed that the samples were trapped in the secondary Dean vortices [42]. The most recent research of Guzniczak et al. (2020) investigated additional force, deformability-induced lift force that affected particle focusing using a spiral microchannel. In this work, Jurkat cells were tested as a cellular deformability model to study the separation of cells in different deformability properties. After the sample flowing through the spiral microchannel, cell viability was not significantly affected at highest flow rate [43].

Another important spiral microchannel application is the isolation of stem cells for further analyze and study in field of medical and biological researches. Nathangari et al. (2015) utilized inertial microfluidics to isolate single cells from clusters for further clonal analysis or differentiation studies. The spiral microchannel was performed as a sorter at minimum flow rate of 1 ml/min sorting Neural stem cells (NSCs) to avoid any deleterious effects on the viability. Owing to the results of experiment, with the low flow rate, the single cells could be isolated from clusters while using the high flow rate, larger astrocytes were collected in outlet 1 while the smaller were collected neurons in outlet 2. Membrane integrity was also performed to estimate cell viability after sorting process. The data demonstrated that the initial cell viability was 92% reduced to 90% after sorting [44]. Similarly, a two-loop spiral microchannel for the enrichment and purification was performed by Song et al. (2017). The spiral micorchannel sorted neural stem cells (NSCs) from non-neural populations of iPSC-derived NSCs. According to the results, introducing the flow rate of 3 ml/min, NSCs were enriched to 2.5 $\times$  and the recovery of NSCs was 93% [45].

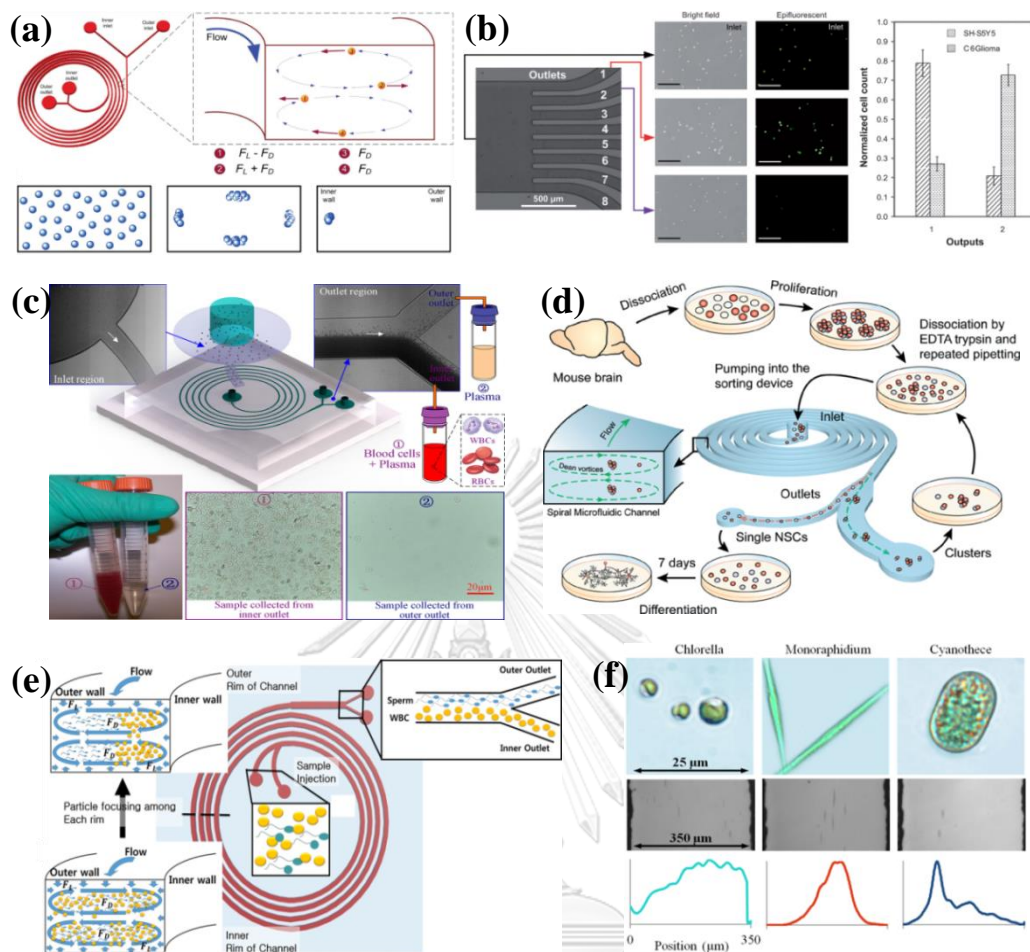


Figure 1.1 Several applications using a classic spiral microchannel to (a) prove the concept of spiral microfluidic study based on the principle of lift and Dean drag force [32], (b) separate tumor cells (neuroblastoma and glioma cells) [38], (c) separate blood cells from plasma [41]. (d) separate stem cells (single cells from clusters) [44], (e) separate sperm cells from WBCs [46], (f) separate non-spherical shapes of phytoplankton [47].

Table 1.4 Progress in spiral microfluidics separating cellular matter—cancer cells, blood cells, stem cells and others.

Authors/Year	Cross Section ( $\mu\text{m}$ )	Dimensions	Shape Size of Sample ( $\mu\text{m}$ )	Flow Rate	Max Velocity (m/s)	Cell Viability	Special Remarks
<b>Kuntaegowda nahalli et al. 2009</b>	W=500 H=130	Loops=5 Radius=1cm	Neuroblastoma=12 Glioma=12-14	3 ml/min	0.769	>90%	
<b>Nivedita et al. 2013</b>	W=500 H=110	Loops=4 Length=8cm	WBCs =10-20 RBCs=7	2 ml/min.	0.606	High	
<b>Xiang et al. 2015</b>	W=150 H=50	Loops=5 Radius=3.5mm Length=16cm	RBCs=8 WBCs=7–12	ml/min	0.7 1.556	>98%	Y-Shaped Outlet
<b>Nathamgari et al 2015</b>	W=500 H=150	Loops=5 Radius=1cm	NSCs Single cells=8–14 Clusters=40–60	1 ml/min	0.222	90%	Considering Stresses Affecting on Viability
<b>Son et al. 2015</b>	W=150 H=50	Loops=4 Radius=0.853cm	Sperm= $\sim$ 5 $\mu\text{m}$	0.52 ml/min	1.156	Double at Inner Outlet	Sperm Quality Analysis
<b>Son et al 2015</b>	W=150 H=50	Loops=4 Radius=0.7cm	Sperm= $\sim$ 5 $\mu\text{m}$ RBCs= $\sim$ 9 $\mu\text{m}$	0.52 ml/min	1.156	—	Separate Sperms from RBCs
<b>Schaap et al. 2016</b>	W=350 H=100	Loops=3 Radius=5mm Length=14cm	Chlorella= $\sim$ 6 Cyanothecae= Long $\sim$ 15.6 Short $\sim$ 11.1 Monoraphidium= 54.6 Diameter $\sim$ 3.14	3.2 ml/min	1.524	—	Non-Spherical Shapes
<b>Song et al. 2017</b>	W=500 H=160	Loops=2 Length=10cm	NSCs=10-12 Non-neural =6-19	3 ml/min	0.625	—	
<b>Thanormsrid etchai et al. 2017</b>	W=500 H=130	Loops=5 Radius=5.5mm In. Radius=5.5mm Out. Radius=9.5mm	MCTCs=10 – 25	1 ml/min	0.256	—	Low-Aspect-Ratio
<b>Nivedita et al. 2017</b>	W=250 H=150	Loops=2 Radius=4.74mm	RBCs=7	3 mL/min	1.333	—	Secondary Dean Vortices
<b>Son et al. 2017</b>	W=150 H=50	Loops=4 Radius=700 $\mu\text{m}$	Sperm= $\sim$ 5 $\mu\text{m}$ WBCs= $\sim$ 12 RBCs= $\sim$ 9	0.52 ml/min	1.156	—	WBCs Removal from Semen
<b>Guzniczak et al. 2020</b>	W=170 H=30	Loops=6 Radius=0.325mm	Jurkat=13 $\pm$ 2	Re = 168	2.944	High	

Apart from blood cells, cancer cells, stem cells and other cellular samples such as sperms and phytoplankton have also been used as a model. The sperm quality analysis using in a spiral channel was presented by Son et al. (2015). The four-loop spiral microchannel showed the enrichment of quality sperm from a semen sample. Normal and abnormal sperms were successfully separated at 0.52 ml/min and sperm viability at the outer outlets was about double the percentage of sperm viability at the inner outlet [46]. In the same year and same group of study, Son et al. (2015) also demonstrated an inertial microfluidic approach using spiral microchannel. According to the review, the spiral microchannel separated non-motile sperm cell from blood cells (RBCs) at the optimum flow rate of 0.52 ml/min. The data depicted that the recovery of non-motile sperm and RBCs were 81% and 99% at outer wall and inner wall outlets, respectively [48]. Two years later, the same of group of Son et al. (2017) developed a sorter for the separation of sperm cells from WBCs using a spiral microchannel. The device could also possibly separate motile sperm, viable less-motile and non-motile sperm cells with a high efficiency. The data showed that recovery rate of sperm cells and WBCs were 83% and 93% at the outlets [49]. As for the experiment of separation for phytoplankton, the sorting of algae using inertial microfluidics for separating three species in shapes and sizes of samples was demonstrated by Schaap et al. (2016). In their work, *Chlorella*, *Cyanothece* and *Monoraphidium* were tested as experimental models and the three-loop spiral with the width of 350  $\mu\text{m}$  and the height of 100  $\mu\text{m}$  was performed. They discovered that the optimum flow rate of 3.2 ml/min for *Monoraphidium* and *Cyanothece* separation could provide 77% of cell separation efficiency [47].

To ease of understanding, the summary of progress of spiral microfluidics for cellular samples is demonstrated in Table 1.4. As seen in the Table 1.4, the blood cells are quite robust to the mechanical forces. The data shows that blood cell viability is >95% followed by cancer cells and stem cells about 90%. However, according to the studies cell viability in spiral microchannel, the data still have been limited and a small number of studies have been reported in terms of cell viability and damage. Therefore, apart from using a classic spiral microchannel examined with diversities of cellular samples, more data of spiral microchannel with several designs are also crucial to collecting and comparing for our research.

### 1.5.2 Progress in spiral microchannel with different geometry designs

Recently, several researchers have focused on the structure designs of spiral microchannel device to achieve a higher separation efficiency and purity. To this end, trapezoidal cross section has been designed to meet the requirement of applications with higher recovery rate. One of the most important reasons that trapezoidal cross section has been drawn considerable interest in recent years and several researchers because this design creates a stronger Dean vortex cores that enhance the separation throughput and efficiency. Wu et al. (2012) exhibited a novel structural design of spiral microchannels that improved the recovery rate of separation. The spiral microchannel with the trapezoidal cross section was fabricated and tested with cellular sample—sorting leukocytes from diluted human blood with the efficiency of cell separation >80% at 0.8 ml/min. As a result, there was no negative effect on cell viability before and after the separation process with cell viability of separated WBCs about 98.22% [50]. One year later, a spiral microchannel with trapezoidal cross-

sections that provided higher recovery rate compared to the conventional spiral microchannel was reported by Guan et al. (2013). The results showed that at the flow rate of 0.5-3 ml/min, the distance of particle focusing in the trapezoidal cross-section is larger than in the rectangular cross-section. This indicates that the efficiency of cell separation with trapezoidal cross-sections is achieved over the rectangular cross section [51]. Warkiani et al. (2014) successfully demonstrated the enrichment of CTCs from WBCs using a novel spiral microchannel design with the trapezoidal cross section. They observed that the smaller particles tended to move towards the outer wall while the larger particles equilibrate close to the inner wall. Moreover, the device could separate CTCs from WBCs successfully with the recovery rate of >80% with a relatively high purity. In addition, the data showed that shear exerted on the cells during the process of cell separation did not significantly cause cell loss (>90% viable cells) and morphological cancer cells remained unchanged during the separation process [52]. In 2017, the microfluidic cell retention device using spiral microchannel with trapezoidal cross-section was utilized by Kwon et al. (2017). The data was found that CHO cells were focused at the equilibrium position near the inner wall and went to the inner outlet while the cell-limited harvest stream moved towards the outer wall and went to the outer outlet with the recovery of 99% and cell viability >97% [53]. Al-Halhouli et al. (2018) proposed the experiment of spiral microchannels with a trapezoidal cross section to sort different sizes of microbeads. The spiral microchannel consisted of 8 loops with the width of 600  $\mu\text{m}$  and the inner height and outer height of 50 and 90  $\mu\text{m}$ . Using this platform, the spiral microchannel with the trapezoidal cross section could sort the mixture of 5 and 15  $\mu\text{m}$  microbeads at the flow rate of 5 ml/min with a high recovery rate successfully [54]. Rzhnevskiy et al. (2019) introduced a spiral microfluidic chip with a trapezoidal cross section for the isolation of tumor cells (PCa) from the urine of PCa patients detected by GPC1. The trapezoidal cross-section had the width, inner wall and outer wall of 600, 90 and 140  $\mu\text{m}$ , respectively. Owing to the results, the spiral microfluidic device provided 86% efficiency of separation at the optimum flow rate of 1.7 ml/min [55].

In addition, several novel structural designs of geometry have been created over the past years for further improvements in the potentially clinical applications. In 2008, the investigation of spiral microchannel with stair-like cross section using inertial microfluidics was exhibited by Ghadami et al. (2017). According to the results, vortices were positioned in the longitudinal direction. The equilibrium position of particles was close to the inner wall with below the threshold volume of flow rate while particles were trapped in the outer vortex with above one. In this way, different-size particles could be sorted easily [56]. In 2012, a novel design inertial microfluidics was introduced as a double spiral microchannel. Sun et al. (2012) introduced a double spiral microfluidic platform for label-free tumor cell separation and enrichment. The double spiral microchannel was designed with S-turn junction added for reversing the flow direction. According to the experiment, large tumor cells tended to be focused at the middle of the outlet while smaller hematologic cells tended to be removed from the inner outlet. As a result, the separation of tumor cells (MCF-7 and Hela) from whole blood 92.28% and 96.77% of tumor cells were collected at the inner and middle outlet with tumor recovery rate of 88.5% without noticeable cell damage [57]. Similarly, Wang et al. (2020) also utilized double spiral microchannel for fractionation of cellulose nanofibers (CNFs). They examined the

regular and double spiral microchannel with different radius curvatures and length to compare fractionation efficiency. The result showed that the fractionation efficiency of spiral microchannel with larger radius curvature was 75.4% while the spiral microchannel with smaller radius curvature was 70.9%. Surprisingly, the fractionation efficiency of the double spiral microchannel was lower than a classic spiral microchannel [58]. Moreover, another spiral microfluidic design was also proposed as a cascaded spiral microchannel to improve the efficient separation. In 2014, cascaded inertial focusing microfluidics for tumor isolation with high purity was proposed by Kim et al. (2014). The data demonstrated that CTCs (Human breast cancer epithelial cells) were separated from WBCs with a high efficiency of 86.76%, depletion rate of 97.91%, viability of >90% and retaining their initial morphology [59]. Like Kim's study, Abdulla et al. (2018) investigated a cascaded spiral microfluidic device for separation of circulating tumor cells from human blood. The cascaded spiral microfluidic device consisted of three parts: two parts of spiral channels and one part of zigzag channel. According to the results, human lung cancer cells (A549) and human breast cancer cells (MCF-7) were isolated from human blood cells (WBCs and RBCs) with the separation efficiency of 80.75% and 73.75% and cell viability of 95% and 98%, respectively [60]. In 2018, the hybrid chip was first introduced by Chen's research. Chen (2018) proposed a triplet parallelizing spiral microfluidics for tumor separation. This study exhibited a hybrid chip which interconnected with the triplet parallelizing spiral microchannel and numerable tilted slits (Spiral-Slits Chip). Using inertial platform, the chip successfully separate CTCs from blood cells—WBCs and RBCs at a high flow rate with 90% efficiency [61].

To improve more the efficacy of cell separation and purity, some studies have developed the design and fabrication of spiral microchannel with 3D spiral or multiplexed spiral microfluidic chip. In 2014, a multiplexed spiral microfluidic chip with three spirals stacked for CTC enrichment from whole blood was developed by Khoo et al. (2014). The device could separate CTCs—breast cancer cells and lung cancer cells from whole blood successfully. Owing to the results, the multiplexed spiral microfluidic chip provided high throughput of 20 times faster, high sensitivity of 100% detection and isolated CTCs remained viable [62]. Similar to the group of Khoo et al., Warkiani et al. (2015) also reported inertial microfluidics using a multiplexed spiral microfluidic chip for tumor isolation with ultra-fast and label-free. A multiplexed spiral microfluidic chip was fabricated with three stacked spiral microchannel and two loops of spiral. The results demonstrated high recovery of >85%, WBCs depletion of 99% with high viability [63]. The same group of Warkiani et al. (2015) introduced multiplexed inertial filtration system with the trapezoidal cross section. In this study, the multiplexed device consisted of 40 spiral microchannels. The results suggested that the multiplexed device could provide a high throughput at 150–300 ml/min [64].

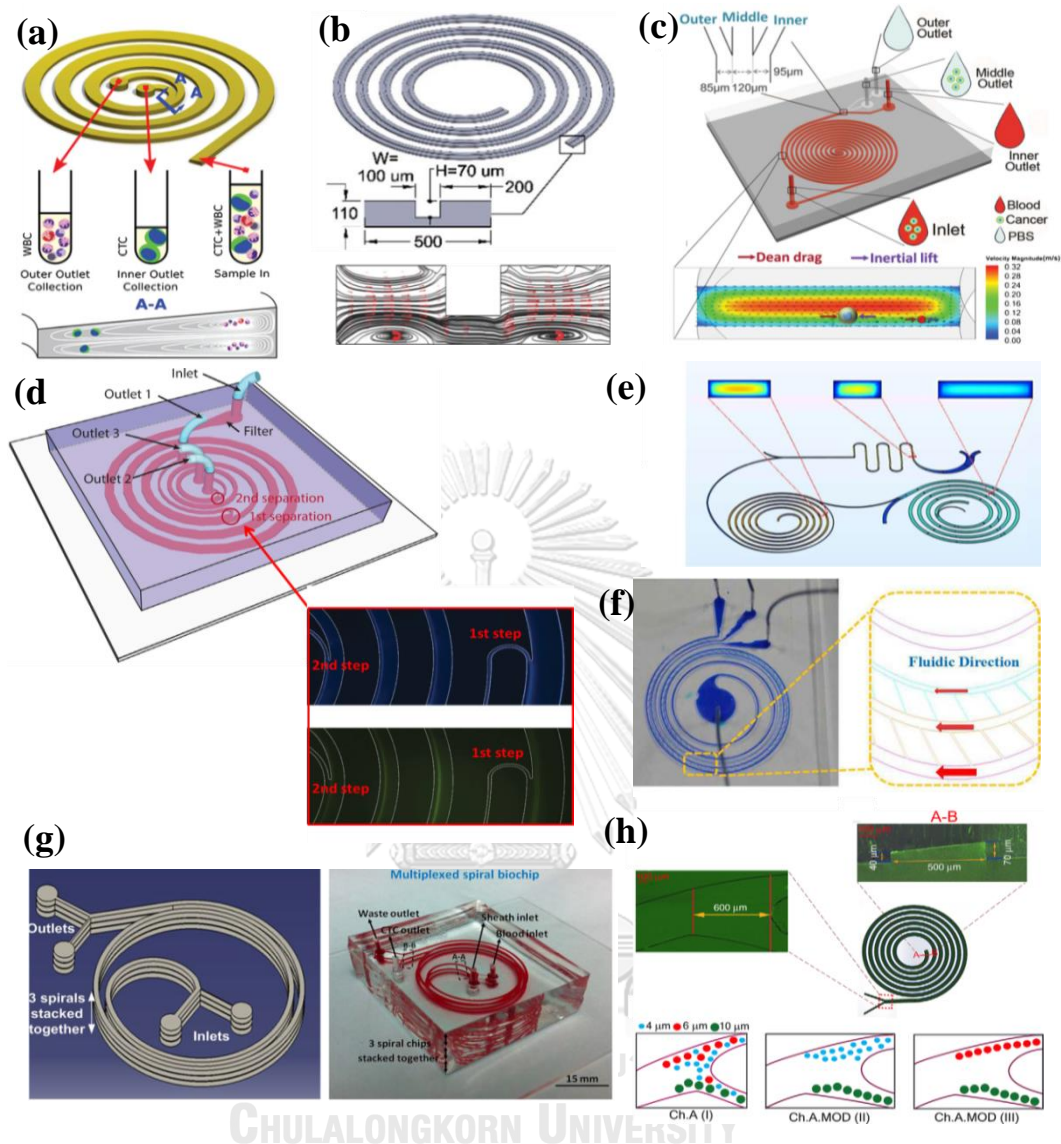


Figure 1.2. Spiral microchannel with (a) the trapezoidal cross section [52], (b) stair-like cross section [56], (c) double spiral microchannel for tumor cell separation [57], (d) cascaded spiral microchannel for CTCs isolation [59], (e) two spiral channels and one zigzag channel [60], (f) the triplet parallelizing spiral microfluidics for tumor separation [61], (g) multiplexed spiral microfluidics [62] and (h) the modified outlets [65].

As can be seen from the above studies, several researchers have created many designs to achieve their goals with a higher efficiency and purity to meet the demand of specific applications such as rectangular channels with ultra-low aspect ratio, trapezoidal cross section, stair-like cross section, cascaded spiral microfluidic device and multiplexed spirals. However, the recent study proved that the structural designs of the outlet (downstream) also dominated the efficiency of particle/cell separation. With a proper design of flow conditions and outlets, inertial microfluidic device could be achieved with more efficiency of separation. The most recent study of spiral microchannel with trapezoidal cross sections was performed by Mihandoust et al. (2020). The group of Mihandoust investigated the modification of three different outlet geometries of spiral microchannels that could provide more efficient separation. Using 4, 6 and 10  $\mu\text{m}$  particles were successfully demonstrated. The modified outlet geometries of the spiral microchannel with trapezoidal cross section could improve the particle efficient separation (>98%) [65]. According to the above studies, the summary of spiral microfluidic studies is presented in Table 1.5 with available information including cross section of the channel, dimensions, maximum of flow rate, maximum of velocity and special remarks reported in recent years.

The above spiral microfluidic studies provide us a better understanding of the separation principles of inertial lift force and Dean drag force including the balance of inertial lift force and Dean drag force, vortices and several applications in use. However, it is not sufficient to fully understand the mechanism of the particle separation due to the lack of theoretical and experimental data and the reliable results rely on the laboratory experiments but not the numerical model or computational simulation. Moreover, according to Dean drag force, this force is a function of the radius of curvature which cannot maintain or sustain the Dean drag force constantly from the first to the end of the loop and it requires the length of channel for particle focusing. This limitation may be addressed by using alternative designs of spiral microfluidics to improve the efficiency of separation such as trapezoidal cross-section and 3D or multiplexed spiral microfluidics. However, the productions of these alternative designs are expensive. For this, it is not suitable to produce large numbers of qualities with low cost compared to the classic spiral microchannel [66]. Therefore, a novel approach of the inertial microfluidics that constrains inertial lift and Dean drag forces with higher controllability to occur in fixed directions and magnitudes is contraction-expansion array (CEA). For more information, this approach will be described and compared to the spiral microchannel in the next section.

As seen in the Table 1.5, the data demonstrates the experiment of spiral microchannel designs with varieties of designs. Usually, high flow rates are required for spiral microchannel approaches to sort samples efficiently and effectively in the range of 0.1-3.5 ml/min. However, increasing flow rate may have negative effects on cell viability. For this reasons, it is necessary to compare another inertial microfluidics with low flow rates in order to prolong and maintain cell viability. Therefore, the approach of contraction-expansion arrays is also introduced and compared to the spiral microchannel approach.



Table 1.5. Progress of several designs of spiral microchannel for specific applications.

Authors/ Year	Cross Section ( $\mu\text{m}$ )	Dimensions	Shape Size of Sample ( $\mu\text{m}$ )	Flow Rate	Max Velocity (m/s)	Cell Viability	Special Remarks
<b>Wu et al. 2012</b>	W=500 In.Height=70 Out.Height=100		Beads=6,10 or 15.5	0.8 ml/min	0.314	98.22 %	Trapezoidal Cross-Section
<b>Sun et al. 2012</b>	W=300 H=50	Loops=6 Radius=9mm	MCF-7=18 Hela=13 Blood cells=6	25 ml/hr	0.463	High	Double Spiral (S-Turn)
<b>Guan et al. 2013</b>	W=600 In.Height=80 Out.Height=130	Loops=8 Radius=8mm	Beads=5.78, 9.77, 15.5, 26.25	3.5 ml/min	0.926	—	Trapezoidal Cross-Section
<b>Warkiani et al. 2014</b>	W=600 In.Height=80 Out.Height=130	Loops=8 Radius=8mm	CTCs=10–20 WBCs=7–12	1.7 ml/min	0.450	90%	Trapezoidal Cross-Section
<b>Kim et al. 2014</b>	W=300 H=50	Radius=5000 $\mu\text{m}$	Beads=10,20 MCF-7= 17.58 WBCs= 9.02	3 ml/min	3.33	>90%	Cascaded Spiral
<b>Khoo et al. 2014</b>		Loops=2 Three Stacked Spiral	Breast cancer =13 Lung cancer =12.5-20.6 Blood Cells= $\sim$ 3– 15	Ratio of flow rate (Sample and sheath)=1:9		High	Multiplexed Spiral
<b>Warkiani et al. 2015</b>	W=500 H=170	Loops=2 Radius of $\sim$ 10 mm	Beads=6, 10,15 Blood Cells= $\sim$ 3– 15 CTCs= $\geq$ 15	Sample=10 0 $\mu\text{l}/\text{min}$ Buffer=750 $\mu\text{l}/\text{min}$	0.167	High	Three Stacked Biochips
<b>Warkiani et al. 2015</b>	W=600, In.Height=130 Out.Height=80 W=450, In.Height=70 Out.Height=30	Loops=8 Radius=8 mm	CHOs=10–20 Yeasts=3–5	6 mL/min 2 mL/min	1.587 1.481	—	Trapezoidal Cross-Section 40 Multiplexed Devices
<b>Kwon et al. 2017</b>	W=600 In.Height=80 Out.Height=130 W=1000 In.Height=260 Out.Height=80	Loops=8 Four Spirals Loops=6	CHO cells= 17.7 $\pm$ 2.5	1 mL/min	0.098	>97%	Trapezoidal Cross-Section 40 Multiplexed Devices
<b>Ghadami et al. 2017</b>	W=500 H=110	Loops=4 In.Radius=2mm	HUVEC=7.32 L929=20	2.304 ml/min	0.698	—	Stair-Like Cross Section
<b>Al- Halhouli et al. 2018</b>	W=600 In.Height=50 Out.Height=90	Loops=8	Beads=5,10,15	5 ml/min	19.84	—	Trapezoidal Cross Section

<b>Abdulla et al. 2018</b>	Part1:W=300 H=80	Loops=5 with one zigzag channel	Beads=5,8,15,24 A549=10~15	Sample=2 ml/min	1.389	95- 98%	2 Spiral and 1 Zigzag
	Part2:W=600 H=80		MCF-7=15~25	Buffer1=1. 2 ml/min			
	Part3:W=200 H=80		RBCs=7.34	Buffer2=1. 2 ml/min			
<b>Chen 2018</b>	W=200 H= 70	Radius=1 cm	CTCs= 15~25 WBCs=9~16 RBCs=4-8	120 ml/h.	2.381	—	Triplet Parallelizing Spiral
<b>Rzhevskiy et al. 2019</b>	W=600		PCa= ~15~20	1.7 mL/min	0.411	—	Trapezoidal Cross-Section
	In.Height=90 Out.Height=140						
<b>Wang et al. 2020</b>	W=300 H=45	Loops=6 Radius=5mm	CNFs= 200~300 nm	220 $\mu$ L/min	0.272	—	Double Spiral
<b>Mihandoust et al. 2020</b>	W=500	Loops=6	Microbeads=4,6, 10	3.5 mL/min 1 mL/min	2.121 0.606	—	Trapezoidal With Modification
	In.Height=40 Out.Height=70	Loops=6 Extended =800 $\mu$ m					

## 1.6 Reviews of Contraction-Expansion

In 2011-2013, the studies of Lee et al. (2011) presented a proof of concept of contraction-expansion microfluidic device for completing separation of microparticles. In this work, the comprehensive of physics and the design of CEA microfluidic device were described and exhibited by the experiment of microparticles. The microchannel was designed with the width and depth of 350 and 38  $\mu$ m while the contraction regions were designed as rectangular reservoirs placed along the side microchannel (side wall 1) with the width and length of 50 and 300  $\mu$ m. The particles of 4 and 10  $\mu$ m were examined as a model. The particle migration is determined by the balance of the inertial lift forces and Dean drag forces. According to the results, the device achieves the separation of larger particles (10  $\mu$ m) to move towards the side wall 1 (dominated by inertial lift forces) while smaller particles (4  $\mu$ m) move away from the side wall 1 (dominated by Dean drag forces) [67]. Two years later, the same group, Lee et al. (2013) developed and modified the contraction-expansion microfluidic device for cancer cell separation from human whole blood. In this experiment, a low flow rate was employed to avoid cells from stresses in fluid. The CEA microchannel was designed with the width and depth of 350 and 50  $\mu$ m. The contraction regions were designed with six rectangular structures and placed along the side microchannel (side wall 1). The results were similar to the previous research, the large particle (cancer cells) move towards the side wall 1 while the smaller particle (WBCs and RBCs) move towards the side wall 2. Furthermore, the separation efficiency was 99.1% while a blood cell rejection ratio was 88.9% and further improved to 97.4% using two-step filtration process without significantly effect on cell viability [68].

In 2008-2015, an inertial method was introduced by Park et al. (2008) using contraction-expansion microchannel in turn and series with axisymmetric multi-orifice channels. The contraction-expansion reservoirs were designed as axisymmetric pattern. The contraction regions have the width and length of 40 and 100  $\mu$ m while the expansion region was the square of 200 $\times$ 200  $\mu$ m wide. They found that the particle focusing was located at two side positions ( $\sim$ 0.6 r') in the outlet channel with

$Re_p$  of 0.8 to 2.3 while at the middle of the channel with  $Re_p$  of 3 to 3.5 [69]. Wu et al. (2015) utilized the inertial microfluidics using a contraction-expansion microchannel to separate microparticles and cells with sheathless particle, a high efficiency of separation, high purity and high throughput. The designs were divided into three parts: a straight channel with low aspect ratio, symmetrically square microstructures in series and a trifurcating outlet. They observed that larger particles move towards the centerline of the channel whereas the smaller particles move close to the sidewall of the channel. The particles of 5.5 and 9.9  $\mu\text{m}$  were separated with the efficiency of >92% and 98% and purities of >98% and 92%. As for the cellular sample, WBCs and RBCs were sorted with the efficiency of 89.7% and 99.8% and purities of 91% and 99.6% [70].

Later on, the system configuration was modified by Wang et al. (2013), Wang and P a p a u t s k y (2015), and Wang et al. (2016), reported high size-selectivity, efficiency and purity using a CEA microchannel [71-73]. In their works, two symmetric chambers with high-aspect ratio channel were designed for microvortex-aided cell extraction. A side outlet in each expansion chamber was connected and utilized to continuously siphon. Larger particles by an assistance of a horizontal vortex induced inside the expansion chamber, while the smaller particles still move along in the main flow. Thus, the symmetric chambers with siphoning channels cause the formation of vortex and cell extraction. According to Wang et al. (2013), microbeads of 21  $\mu\text{m}$  was separated from 18.5  $\mu\text{m}$  particles with >90% purity and 90% efficiency while large particles were isolated from human-blood sample with an efficiency of 86% and 5 $\times$ enrichment [71]. Owing to the Wang et al. (2015) developed CEA device with siphoning channel that achieves the separation of microparticle mixtures into three components with high resolution [72]. One year later, the same group of Wang et al. (2016) developed inertial microfluidics using contraction and expansion with double sorting and purification function for separation of human cancer stem cells from human blood. The data showed that the device achieved separation of human cancer stem cells from human blood with >90% efficiency and >1500 enhanced purity and removing red blood cells with ~99.97% efficiency [73]. As can be seen, these all studies of Wang et al. showed the high efficiency of separation and purity using the CEA device with siphoning channels as well as applying to other applications including microbeads, human blood cells and human cancer stem cells.

As you can see from the above studies, several studies of contraction-expansion array (CEA) microchannel have been proposed with the alternate arrangement of rectangular structures to improve Dean vortices to be stronger in the system. Unlike the design of Wang et al. (2013, 2015 and 2016) and Lee et al. (2011 and 2013), in 2011, a contraction-expansion microfluidic channel with alternating pattern of reservoirs for rare cell isolation and enrichment was depicted by Hur et al. (2011). The CEA channel was designed with a high aspect ratio straight channel (50 $\times$ 70  $\mu\text{m}$ ). The ten trapping reservoirs were designed with square shape of 400 $\times$ 400  $\mu\text{m}$  and 70  $\mu\text{m}$  deep. The ten trapping reservoirs were placed in an alternating pattern. The results demonstrated that the device achieved the separation of larger cancer cells from the smaller blood cells with remaining highly viable cells as well as determining the optimum flow rate for vortex formation and the critical diameter required for trapping particles [74].

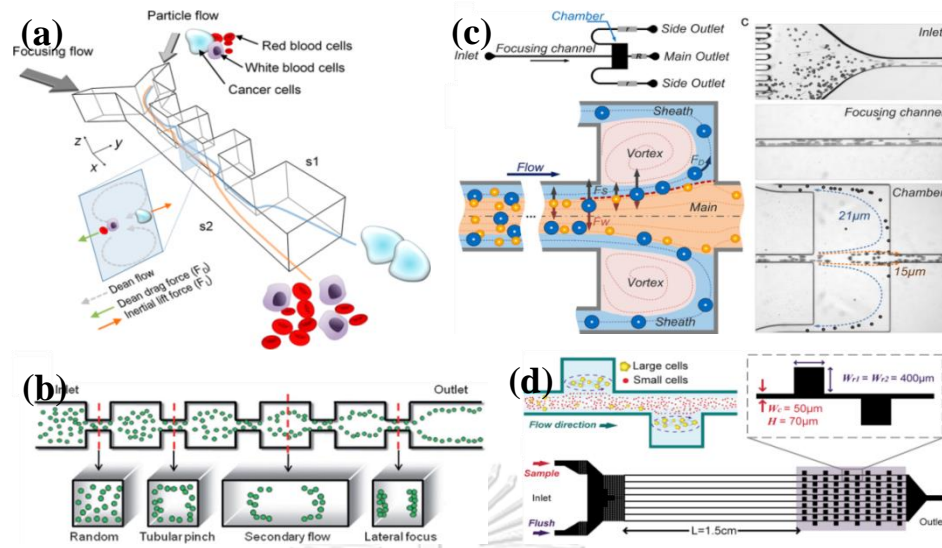


Figure 1.3 The contraction-expansion regions were designed with (a) rectangular structures placed along the side microchannel [68], (b) axisymmetric multi-orifice chambers [69], (c) symmetric chambers with siphoning channels [71] and (d) alternating pattern of reservoirs for rare cell isolation [74].

To extend the applications of the alternative pattern of contraction-expansion regions, some studies proposed a novel design of contraction-expansion cavity arrays. Zhang et al. (2013) illustrated the contraction-expansion arrays with asymmetrical patterned reservoirs. The expansion-contraction cavity array geometries were designed several shapes including triangular, half circular and diamond cavity arrays. As for triangular cavities, the right angled isosceles triangular cavities had the width of  $900\ \mu\text{m}$  with  $45^\circ$ . According to other shapes, asymmetrically patterned half circular cavities had the diameter of  $900\ \mu\text{m}$  with  $90^\circ$  while asymmetrically patterned diamond cavities had the diagonal length of  $900\ \mu\text{m}$  with  $135^\circ$ . The results showed that at flow rate of  $0.7\ \text{ml/min}$ , three different focusing patterns occurred during the separation and the efficiency of separation had good focusing performance [75]. Two years later, inertial microfluidics with asymmetrical expansion-contraction cavity arrays was utilized by Yuan et al. (2015). In this study, the demonstration of particle focusing in expansion-contraction cavity arrays under Newtonian and non-Newtonian fluids was presented. The right angled isosceles triangular cavities were designed with the longest edge of the triangle of  $900\ \mu\text{m}$ . According to the results, under non-Newtonian fluids, the addition of viscoelastic force was induced and acting on particles. In this way, the performance of particle focusing in visco-elastic fluid was improved by the addition of viscoelastic force. In other word, particles in non-Newtonian fluid tend to be more easily and better focused [76]. Recently, Liu et al. (2019) proposed inertial microfluidic separation using contraction-expansion array (CEA) with varieties of channels and cavity designs. There four designs of CEA were introduced in this work—High-rectangle cavity arrays, Low-rectangle cavity arrays, Circle cavity arrays and Streamline cavity arrays. The results showed that RBCs affected by separation process was not significant that had little effect on cell viability. Additionally, using Circle channel to separate for plasma provides efficiency of 96.0% with high cell viability [77].

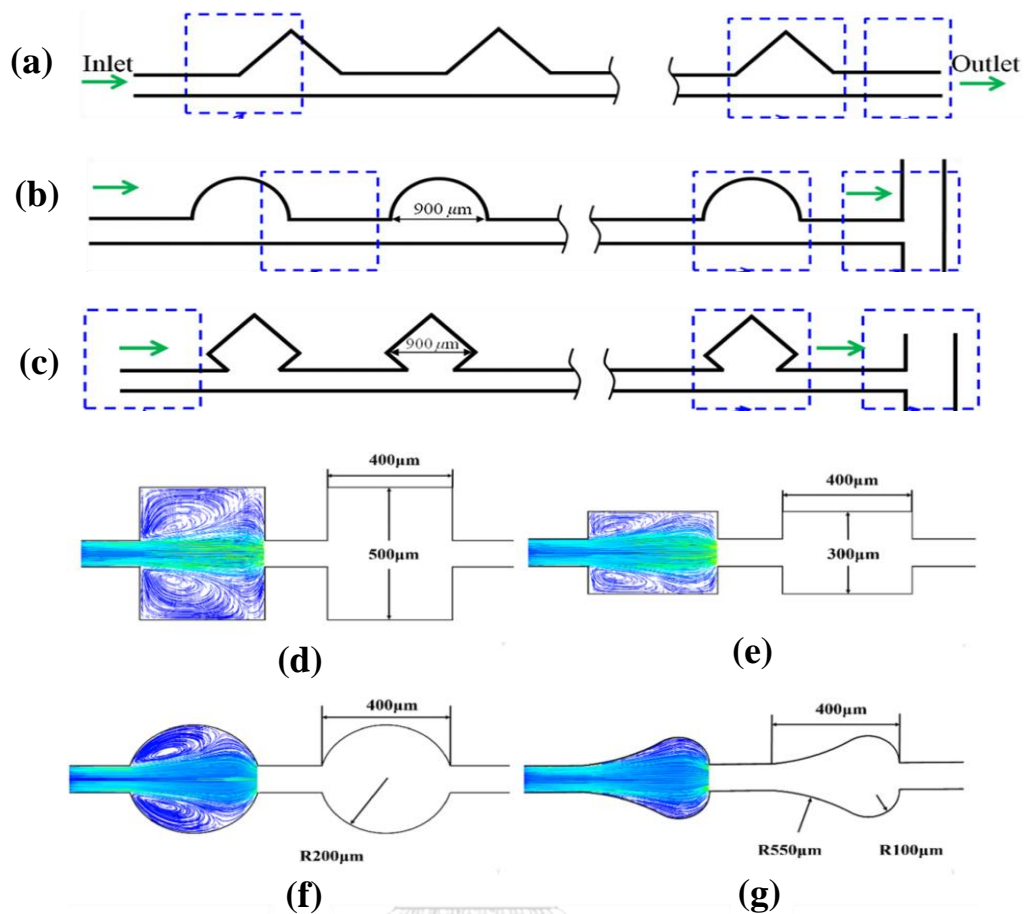


Figure 1.4 The contraction-expansion regions were designed with (a) right angled isosceles triangular cavities (b) asymmetrically patterned half circular cavity arrays (c) asymmetrically patterned diamond cavity arrays [75], (d) High-rectangle (e) Low-rectangle (f) Circle and (g) Streamline cavity arrays [77].

A summary of contraction-expansion arrays studies is demonstrated in Table 1.6 with available information reported in recent years. As seen in the data, although the optimum flow rate to sort particles/cells for these approaches are lower than spiral microchannel approaches. However, the cross-section of CEA channel is smaller which induces the velocity of fluid to be higher which exerts more stresses in the system. According to the study of stresses, the stresses are directly proportional to the velocity of fluid. As a result, the exerted shear stress in CEA may cause cell to die in the system. Therefore, it is really needed to consider not only the optimum of flow rate but also the approaches, types of sample and velocity of fluid for microfluidic separation.

Table 1.6. Progress in several designs of contraction-expansion arrays for specific applications

Authors/ Year	Cross Section ( $\mu\text{m}$ )	Dimensions	Shape Size of Sample ( $\mu\text{m}$ )	Flow Rate	Max Velocity (m/s)	Cell Viability	Special Remarks
<b>Park et al. 2008</b>	Con. W=40 $\mu\text{m}$ L=100 $\mu\text{m}$ Expan. W=200 $\mu\text{m}$ L=200 $\mu\text{m}$	CEA= 80 Length= 24mm	Microbeads= ~7	200 $\mu\text{l}/\text{min}$	2.083	—	Multi-Orifice-channels
<b>Lee et al. 2011</b>	Main. W=350 $\mu\text{m}$ H=38 $\mu\text{m}$ Con. W=50 $\mu\text{m}$ H=38 $\mu\text{m}$ L=300 $\mu\text{m}$	Interval=300 Windows=6	Microbeads=4,10 ,15	22ml/h	3.219	—	Reservoirs Placed Along Side Microchannel
<b>Hur et al. 2011</b>	Main W= 50 $\mu\text{m}$ H=70 $\mu\text{m}$ L= 4.5 cm Con. W=400 $\mu\text{m}$ H= 400 $\mu\text{m}$		Microbeads=1,5, 10 HeLa=12.4 MCF7=20 Blood cell=2-15	4.5 ml/min	21.429	High	Reservoirs Placed in an Alternating Pattern
<b>Lee et al. 2013</b>	Main W=350 $\mu\text{m}$ H=63 $\mu\text{m}$ Con. W=50 $\mu\text{m}$ H=63 $\mu\text{m}$ L=1200 $\mu\text{m}$	Interval=700 Windows=6	Microbeads=4,10 ,15 MCF-7=15-30 Blood cells=2-15	12.4 ml/h 6ml/h	1.095 0.529	High	Reservoirs Placed Along Side Microchannel
<b>Wang et al. 2013</b>	Main W=50 $\mu\text{m}$ H=100 $\mu\text{m}$ L=10mm Chamber W=500 $\mu\text{m}$ H=500 $\mu\text{m}$		Microbeads=18.5 , 21 Microbeads=21 RBCs= 7	0.5 ml/min	1.667	—	Symmetric Chambers with Siphon
<b>Zhang et al. 2013</b>	Triangular W= 50 $\mu\text{m}$ H= 70 $\mu\text{m}$ L=900 $\mu\text{m}$ Half Circular D=900 $\mu\text{m}$ Diamond L=900 $\mu\text{m}$	Length=31m m CEA Cavities=17	Microbeads=3.2, 4.8,9.9 $\mu\text{m}$	700 $\mu\text{l}/\text{min}$	3.333	—	Triangular, Half Circular and Diamond Shape
<b>Wu et al. 2015</b>	Main W=120 $\mu\text{m}$ H=21 $\mu\text{m}$ L=2.5cm Con. W=45 $\mu\text{m}$ H=21 $\mu\text{m}$	Length= 2 cm	Microbeads=5.5, 9.9 RBCs,WBCs	150 $\mu\text{l}/\text{min}$	2.646	—	Symmetrically Square Microstructure

<b>Wang et al. 2015</b>			Microbeads=11,15,18.5,21,23	0.5 mL/min		—	Siphon
<b>Yuan et al. 2015</b>	Triangular W= 100 $\mu$ m H= 40 $\mu$ m L=900 $\mu$ m	Total Length=48m CEA Cavities=26	Microbeads=3.2, 4.8, 13	300 $\mu$ L/min	1.25	—	Isosceles Triangular Cavities
<b>Wang et al. 2016</b>	Main W=30 $\mu$ m H=50 $\mu$ m Chamber W=500 $\mu$ m L=500 $\mu$ m		Microbeads=7,18.5 Microbeads=18.5 RBCs= $\sim$ 7 HuSLCs=12 to 22 RBCs= $\sim$ 7	190 $\mu$ L/min 200 $\mu$ L/min	2.111 2.22	—	Symmetric Chambers with Siphon
<b>Liu et al. 2019</b>	High-Rectangle W= 500 $\mu$ m L= 400 $\mu$ m Circle R= 400 $\mu$ m Streamline R=550,100 $\mu$ m L=400 $\mu$ m	Length=47m m CEA Cavities=66	Microbeads=5,10,15,20 NCI-H1299= 20 $\mu$ m RBCs= 6–9 $\mu$ m	400 $\mu$ L/min	1.333	—	Several Designs

## 1.7 Reviews of Microfluidic Integration

The recent advancement in microfluidics research is the implementation and integration of several microfluidic techniques onto a single chip which is known as Lab-On-a-Chip. Over the past years, the microfluidic systems requiring assembly and fluidic interconnection among other components have been produced in a number of applications and they have been proven to be appropriate for a variety of biological and chemical applications [78].

Several microfluidic devices would be integrated with other techniques which requires less flow rates but still provides a high efficiency by combining other active techniques for example optics, magnetophoresis, dielectrophoresis, acoustophoresis and hybrid techniques. These techniques are applied by external force field to achieve the goals with several functions such as trapping, sorting, imaging, switching, monitoring, culturing, detection and automation.

In this review, we demonstrate the overviews and the examples of successful applications of microfluidic devices combined with other active and passive techniques, known as microfluidic integration. Furthermore, we also show the classification of different types of integrated microfluidic platform including brief research, progress, operations, achievements as well as advantages, disadvantages and technical and biological challenges in clinical applications.

### 1.7.1 Optics

Several integrations of optics with microfluidics have been researched for facilitating detection and automation of biological analysis. In 2003, optical and microfluidics were integrated as a sorter based on the size and refractive index. This device could successfully sort silica and polymer beads with the efficiency of >96% [79]. One year later, Wang et al. 2004 presented the integration of microfluidics with optical force switching for mammalian cell separation. The device was achieved

with sorting HeLa cells expressing a fused histone green fluorescent protein from non-expressing cells with high-throughput, purities and recovery rates [80]. Droplet microfluidics integrating electrowetting-on-dielectric (EWOD) and optoelectronic tweezers (OET) was examined. The device was successfully experimented the automated concentration of HeLa cell sample into droplets. However, the limitation of this work was the positive DEP case causing cells to be attracted to the substrate and adhesion [81]. Another study of the integrated device with optical tweezers and microfluidics was showed the implementation of a cytometer based on refractive optical tweezers for cell trapping, sorting and imaging. The experiment tested on yeast viability with pH. The data confirmed that all the cells under the investigation were viable (pH=6-7) or even after 15 minutes of laser exposure [82]. In the same year, Wang et al. 2011 presented the integration of cell sorting, manipulation, optical tweezers and imaging processing for the separation of rare cells. The device successfully sorted with high recovery rate of >94% and 90% and purity of >96% and 90% for yeast cells and hESC, respectively [83]. The most recent research of optical tweezers for cell isolation was presented by Keloth et al. The combination of optical tweezers and PDMS chip achieved with the isolation of three different types of cells—yeast, single bacteria and cyanobacteria cells and still viable after isolation [84]. In 2012, the technique of optical and cell sorting was integrated as an optofluidic device for analysis and sorting single cells with high selectivity [85]. The use of 3D microfluidic pulsed laser-triggered fluorescence-activated cell sorter was demonstrated by Chen et al. Laser-induced cavitation bubbles in a 3D PDMS microfluidic channel was generated by a high power laser. This device provided a high throughput of 23,000 cells per second and could achieve 90% purity of sorting [86]. In addition, several strategies were adopted to optics and microfluidics recently. The use of the surface enhanced Raman scattering (SERS) coupled with microfluidic channel for the measurements of the sensitivity was presented by Li et al 2013. However, this approach had a lack of scattering intensity of the Raman signal [87]. As can be seen, optical separations by themselves are limited by optical differences. For example, the refractive index of individual cells and size and shape differences. These issues make the separation more difficult. However, optical method that was implemented on microfluidic chip can address these problems by the study of Bates and Lu [88].

### 1.7.2 Magnetophoresis

Magnetophoresis—positive and negative based on microfluidic devices has been also implemented for trapping, focusing, separation, and switching. However, the drawback of this approach is the requirement of using magnetically responsive particles and antibodies as experimental particles [89]. In 2005-2006, magnetophoresis and microfluidics combined for separation of red and white blood cells was presented by the group of Han et al. The group successfully demonstrated the diamagnetic capture (DMC) mode using high-gradient magnetic separation (HGMS) [90] and the single-stage and three-stage cascade paramagnetic capture (PMC) mode [91] to sort red and white blood cells from diluted whole blood. Later on, the development of integration where magnetic particles separated and concentrated into a split droplet using permanent magnet and EWOD was demonstrated. The concentration of magnetic particles was achieved with an



efficiency of over 91%. The separation of magnetic particles was over 94% whereas non-magnetic particle was successfully achieved with 92% [92]. Droplet magnetic particle separation in microfluidics was presented in 2012. The device consisted of two parts—electrocoalescence and magnetic manipulation. The device provided more simplicity and robust compared to other electrocoalescence methods [93]. Similar to Lee et al., Brouzes and his team illustrated the magnetic separation in droplet microfluidic method. The team successfully characterized the efficiency of marginalization of magnetic beads and discovered the efficiency of splitting droplets—magnet strength and droplet velocity [94]. The separation of diamagnetic micro-particles in ferrofluid using the multiphase fluid interface and microscale magnets was presented by Zhou and Wang 2016. The data showed that increasing concentration of ferrofluid resulted in the greater of particle deflections. Moreover, higher magnetic field could be generated by the smaller gap distance and using smaller channel width helped better particle focusing [95]. The advancement of 3D structures of microfluidic technology integrated with Halbach array was presented Wu et al. 2018. The performance of separation was achieved with high efficiency using diamagnetic polystyrene beads in ferrofluids [96]. Another study of integration of magnetic separator with 3D structures of micro copper coil and magnetic tips was demonstrated by Zhi et al. 2019. The data showed that magnetic particles was separated successfully with the sorting ratio of 92.5% at 200 mA [97].

### 1.7.3 Dielectrophoresis

Dielectrophoresis (DEP) causes the movement of cells/dielectric particles or carrier fluid by generating polarization forces within in a non-uniform electric field. Dielectrophoresis (DEP) is another approach of an external force field that often used as particle/cell separation or manipulation. The technique of DEP is also used in the varieties of sample for cell separation or manipulation such as cancer cells [98, 99], yeast cells [100], Neural stem cells [101], bacteria [102], parasites [103]. This technique is often integrated with microfluidics. In an example of this, the technique of dielectrophoresis (DEP) and microfluidics was implemented as an integrated device for accumulation and separation of microparticles. The paired electrode array were aligned vertically, on the top and bottom wall of the channel. The results showed that the device successfully separated the particles of 4.8-8  $\mu\text{m}$  at 2  $\mu\text{l}/\text{min}$  with the purity of 98% [104]. Another study of Dielectrophoresis and microfluidics presented by Moon et al. 2009 also demonstrated the integration for the separation of airborne microbes containing pathogenic microorganisms and dust particles [105]. In 2017, microfluidic actuator using dielectrophoresis for cell separation was presented. The experimental results suggested that in the optimum condition, channel height and electrodes pitch should be located as near as possible while the applied voltage should be high as maximum. The data of efficiency showed that the device provided a high recovery of 93% and purity of 100% for k562 cell separation [106]. The separation of droplets was also experimented using dielectrophoresis for the separations of oil droplets and electrically induced Janus droplets (EIJ) in microfluidic channel. The separation of samples could be achieved by adjusting the applied voltages to the system [107]. Recently, separation of microalgae cells using AC dielectrophoresis in ballast water was proposed by Wang et al. 2018. The device was designed with the integration of 3D electrodes and

the insulated triangle structure into the microchannel while microalgae cells—*Platymonas* and *Closterium* and microplastics were examined to analyze the related parameters and efficient separation. The results indicated that using negative and positive DEP force could successfully isolate *Platymonas* and *Closterium* with a high efficiency [108]. However, using DEP is quite limited because many characteristics can cause cellular sample to change their properties including size of cells and cell membrane as well as impacts permeability, capacitance, and conductivity. In worst case, DEP can potentially cause cells to die and damage since positive DEP causes adhesion between cells and electrodes and hinders the release of cells. Furthermore, the efficiency of cells/particle separation is required a high conductivity and dielectric properties of cells depending on the stage of cell cycle and DEP force as well as the physical properties of cells such as internal polarizability, cell shapes and sizes. Normally, DEP force is quite weak compared to the hydrodynamic force when they are integrated [98]. Therefore, externally applied field that integrated to microfluidics must be considered carefully.

#### 1.7.4 Acoustophoresis

Acoustophoresis was applied to many microfluidic application known as hydrodynamic acoustic sorter (HAS). In 2009, the group of Lenshof engineered the integrated microfluidic device with acoustophoresis an ultrasonic standing wave (USW) and microfluidic separation for preparing diagnostic plasma from whole blood. The results showed that the USW separator could clean plasma of 12.5% from whole blood [109]. Similar to Lenshof et al. 2009, Augustsson et al. 2012 used ultrasonic resonances to separate Circulating tumor cells (CTC) from WBCs. The results indicated that the device provided a high recovery rate of 93.6% to 97.9% with the purity of 97.4% to 98.4% while cell loss and cell proliferation affected from acoustophoresis was not found [110]. The integration of separation with acoustic forces generated by ultrasonic standing waves and gravitational field in split-flow lateral-transport thin (SPLITT)-like fractionation channels was proposed by the study of Ratier and Hoyos. The integrated microfluidic device was achieved with separating 5 and 10  $\mu\text{m}$  of microparticles and could be extended to biomimetic particles and blood cells [111]. One year later, study of microfluidics using ultrasound in a microfluidic channel was demonstrated. This novel method was the use of the first and third modes of the standing waves for particle separation with positive acoustic contrast factors. The results showed the separation efficiency of 100% and purity of 90% of 10 and 5  $\mu\text{m}$  microbeads [112]. The use of travelling surface acoustic waves (TSAW) was also implemented for separating particles of 3 and 10  $\mu\text{m}$  with a high efficiency of 100% [113].

#### 1.7.5 Hybrid techniques

There have been several researches focusing on the development of integrated microfluidic devices with multiple operations into a single chip. The techniques of hybrid that integrate with other techniques—passive and active were demonstrated over the past years. In 2014, the integration of deterministic lateral displacement and magnetophoresis were invented as a sorter for separating CTCs from blood samples [114]. The same technique of separation, deterministic lateral displacement, automatic purifying device and a capturing platform were integrated by the group of Jiang [115].

In 2014, the technique of inertial flow separation and micromixer was integrated for detection and separation in a centrifugal [116]. The combination of acoustic operation for particle preconcentration and dielectrophoretic operation for single particle focusing in microfluidic system was introduced in 2008. The characterizations of acoustic and DEP forces were discovered for the optimization of frequency, height of levitation and lateral confinement [117]. Similarly, the group of Cetin et al. 2016 presented a microfluidic device combining the acoustophoresis and dielectrophoresis techniques for particle wash and separation. Separation part is based on dielectrophoresis while washing part is based on acoustophoresis [118]. In 2017, Chen et al. demonstrated a novel hybrid method consisting of the technique of electroosmosis (ICEO) and dielectrophoresis for prefocusing particles and separating particles with different dielectric properties. The mixtures of yeast cells and silica particles were successfully separated with the efficiency of >96% [119]. A novel hybrid technique combining dielectrophoresis (DEP) and inertia microfluidics for particle tunable separation was proposed by Zhang et al. 2018. The efficacy of device depends on adjusting the electric voltage [120]. Hybrid magnetic and deformability integrated microfluidics for CTCs isolation was presented by Chen. The device had two functions—capturing cells based on size and isolating cells based on magnetic. Introducing with a high flow rate, the integrated device showed a high efficiency of cell capture (>90%) with a high viability (96%) [121].

#### 1.7.6 Integrated microfluidics for monitoring and detection.

In some studies, microfluidics has been integrated to other techniques for monitoring and detection. The detection and separation technique was integrated onto a single chip for complete analysis [122]. The integration of separation and purification was achieved for microbial monitoring for detection and identification [123]. The technology of Electrophoresis (CE) and microfluids was employed for microbial detection and other bio-analysis [124]. The electrochemical sensor and mobile interface were integrated for detection of water-borne pathogens. This device could detect bacterial pathogens [125]. In 1998, the integration of fiber optic biosensor with an automated fluidic system and a radio transceiver was designed for identify specific bacteria in an aerosol and transmit the data to an operator on the ground [126]. As seen in the data of microfluidic integration with other approaches, they provide several advantages such as increase the efficiency in specific applications, reproducibility of experiment and automation for monitoring and detection. However, they have suffered a major drawback of microscale detection. Because microfluidic channel are susceptible to pressure by inducing fluid flow and blockage by particle matter or bubble occurring in the system, these issues are not suitable for the use of microfluidic devices for developing in-situ sensing systems for detection [127]. Furthermore, the automated rapid detection is required to improve for further development of integrated microfluidic detection.

#### 1.7.7 Integrated microfluidics with other techniques.

The integration of optics and microfluidic chips which provide small and inexpensive way to interrogate biological systems was proposed [88]. The integration of microfluidic channel and electronic circuits chip was demonstrated by Yang et al. in 2017. The results could be developed with high density and functionality in small

packages [128]. Recently, the integration of microfluidics with microvalves was engineered for identifying and sorting cells using image processing algorithms and optical imaging [129].

### **1.8 Summary and Approach**

As the above mentioned studies, the integrated microfluidic devices have been intensively studied and invented for several purposes over the past decades. They have a high potential to be successful in several applications by integrating other passive or active techniques. As for sorting and trapping techniques, the potential techniques for integration would be hydrodynamics, optics, magnetophoresis, dielectrophoresis, acoustophoresis. With these potentials, we have studied these techniques over the past years and ended up with the integrated microfluidic device with the hydrodynamic technique. The main reason that hydrodynamic technique was chosen to be utilized because this technique is a passive based the size of samples which is not required an external force field that may affect cell biological property and the complexity of external equipment for operation. However, some studies show that utilizing hydrodynamic approach may exert stresses in our system resulting cell loss and damage during the operation. Therefore, it is so important to consider and investigate cell loss and damage in microfluidic system and find the way to maintain the efficiency of the device while maintain cell viability as much as possible using the knowledge of the past studies. However, the past studies still have a lack of information of how much cell loss and damage related to magnitude of stress, exposure time and type of samples which are significantly important to the applicability of devices for clinical and biological applications. For this reason, we cannot applied or use those information to predict or evaluate how much damages would occur to cells in our system. With these limitations, we have to test the device experimentally, theoretically and computationally and collect all data by ourselves with the particular samples.

One of the biggest challenges in this integrated microfluidic work is to maintain the efficiency of integrated microfluidic device as well as prolong the viability of cells. In general, using a high flow rate is required for increasing the efficiency of microfluidics. However, the increase of fluid flow results in the mismatched velocity, increase of high pressure, deformation of cross section and leaks of microfluidic channel. These issues could decrease the efficiency of operation instead. It should be noted that integrating with a microvalve to control the flow rate in our system would not be practical in terms of complex fabrication process, slow responses and high fabrication cost. Moreover, stresses—extensional and shear stress in the system become stronger as flow rate increased leading to cell biological/physical changes, cell damage and cell loss. Therefore, it is important to consider the negative effects of using a high flow rate in the integrated microfluidic system.

Ultimately, after the integrated microfluidic device is designed and fabricated, the device will have to be examined repeatedly to ensure that this device will be able to operate properly with a high efficiency of sorting, trapping and culturing with either single cells, clusters or spheroid as well as prolonging cell viability and preventing cells from damage by stresses in our new system.

## Chapter 2

### Spiral Microchannel and Contraction-Expansion Array

According to the preliminary experiment, it obviously found that the loss of cell viability was appeared after the cellular sample flowing through the sorting device. There was a severity of cell damage causing cell death and other changes of cells during the process of cell separation. This chapter presents the investigation of a spiral microchannel and contraction-expansion microchannel array (CEA) affecting cell viability and damage. The chapter starts with the system fabrication of a sorting device—spiral microchannel and CEA. Next, the experiment also demonstrates the complete setup—spiral microchannel and contraction-expansion microchannel array that were analyzed in each components while varying flow rates under different conditions. After the experiment, cellular samples were investigated under three methods: cell viability, cell morphology and intracellular structures with Trypan Blue, SEM and Wright-Giemsa stain, respectively and compared percentage of cell viability and normal cells after flowing through both devices. Finally, a computational simulation was also employed to give the explanation of the causes of cell loss and damage during the operation of separation.

#### 2.1 Design and Fabrication

Spiral microchannel was designed as an Archimedean spiral microchannel, consisting of five loops with two inlets. The width of 500  $\mu\text{m}$  and the height of 130  $\mu\text{m}$  were fixed with the average radius of curvature of 750  $\mu\text{m}$  and increasing at a constant rate of angle. The outlet consisted of two parts; the straight channel with a length of 10 mm and a gradual expansion with  $9^\circ$  connected to the 10 outlets. Each outlet was designed with a width of 200  $\mu\text{m}$  with the same height (Figure 2.1a).

As for CEA, there were two contraction-expansion chambers, namely the upstream and downstream microchamber. The CEA consisted of the square channel of 50  $\mu\text{m}$  connected to the expansion chamber downstream with the width of 500  $\mu\text{m}$ . On both sides of the upstream microchamber, there were two side outlets connected to the downstream microchamber (Figure 2.1b).

According to the sorting fabrication, the process began with a silicon mold. A 6-inch silicon wafer was cleaned by dipping it in a piranha solution to remove organic contaminations. Then, the mold was spin-coated with the Hexamethyldisilazane (HMDS) and baked at  $90^\circ\text{C}$  for 90 s to improve the photoresist, PR (Soho Sumitomo PFI27C9), adhesion to the oxidized silicon wafer surface. The photoresist was spin-coated at 1000 rpm for 20 s to obtain 2  $\mu\text{m}$  thickness. The pattern of spiral microchannel/CEA was constructed by photolithography method using a mask aligner (EVG 620, EV Group, Oberosterreich, Austria). The spin-coated wafer was exposed with UV-light through a lithograph mask for 5 s. After that, the silicon wafer was baked at  $110^\circ\text{C}$  for 100 s and then developed with SD-W for 75 s, and hard baked at  $120^\circ\text{C}$  for 80 s. Finally, the wafer was etched using Deep reactive-ion etching (DRIE) (Figure 2.2) technique ( $\text{SF}_6/\text{C}_4\text{F}_8$  gases) to create the pattern of microchannels to the desired depth.

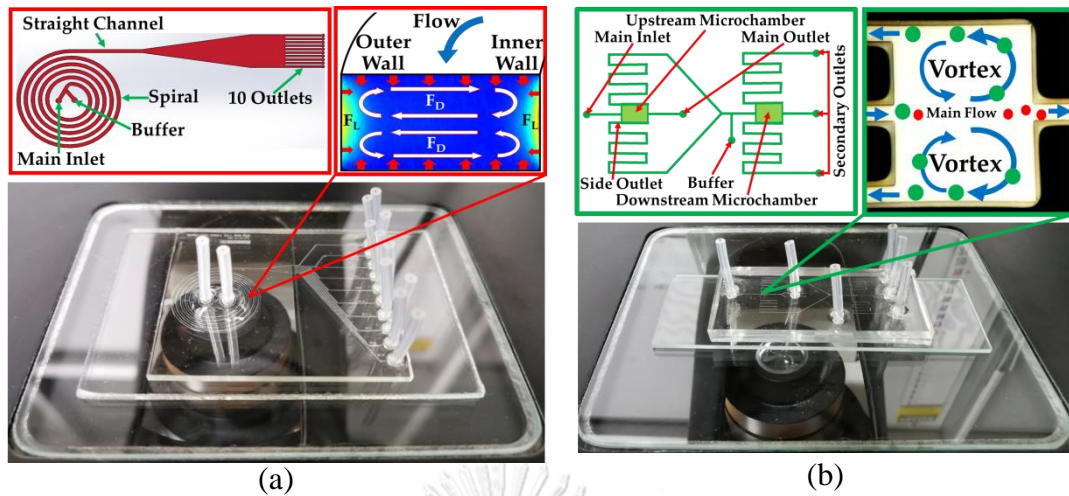


Figure 2.1 Schematic drawing (not drawn to actual scales) and actual device of (a) spiral microchannel and (b) contraction-expansion array.

Polydimethylsiloxane, PDMS (Sylgard 184 Silicone Elastomer, Dow Corning, Auburn, MI, USA) and a curing agent were mixed at the ratio of 10 to 1 by weight. PDMS structures were casted by pouring on the silicon mold. After that, PDMS was cured in an oven at 75 °C for 90 min to form a spiral microchannel/CEA, and then peeled off. Finally, inlet and outlet reservoirs were punched using a pin vise to connect silicone tubes. For the device assembly, the PDMS channel and glass microscope slide were exposed to oxygen plasma under 40 sccm of O<sub>2</sub> with 30 watts for 90 s and put in contact with one another to enclose the spiral microchannel/CEA chip (Figure 2.3).

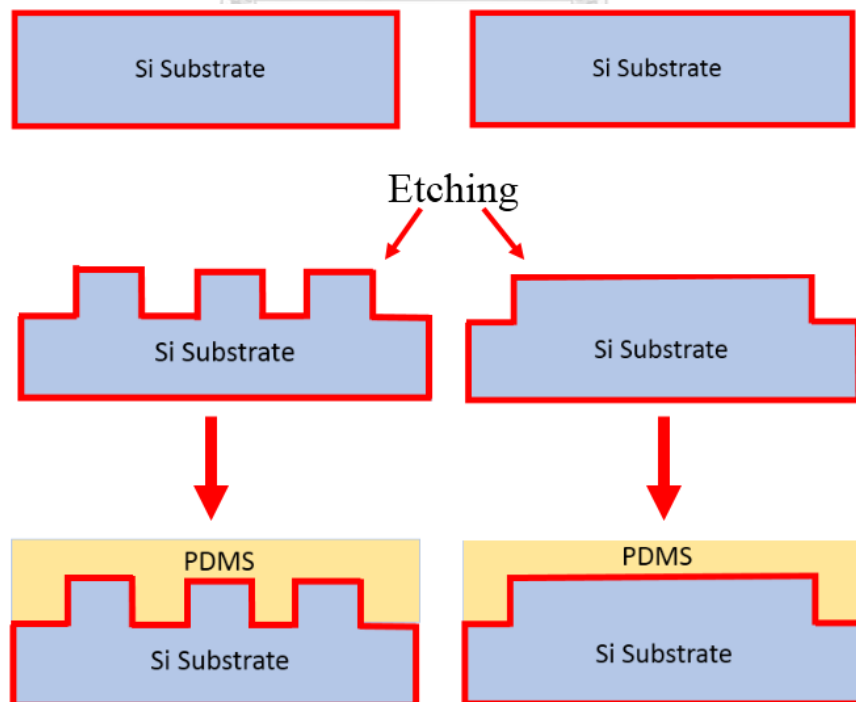


Figure 2.2 Process flow of PDMS fabrication by Etching

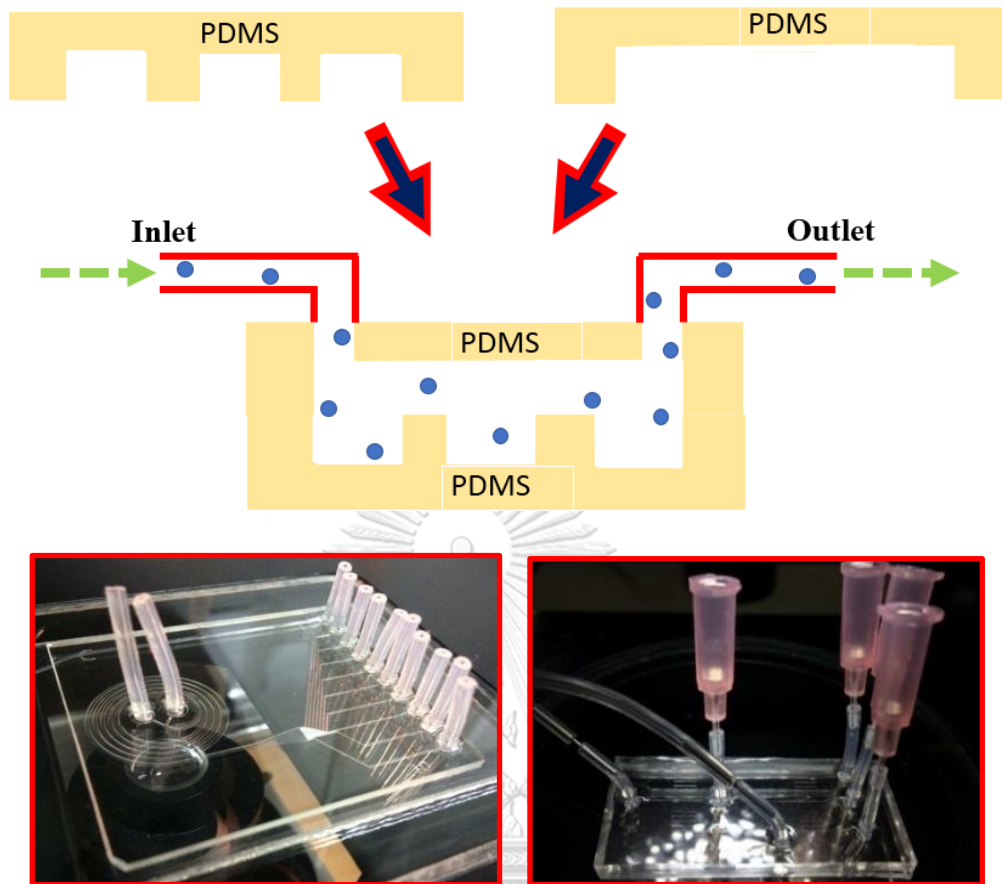


Figure 2.3 An assembled microfluidic device—spiral microchannel (left) and CEA (right) with bonding the PDMS on a slide glass or PDMS

## 2.2 Experiment

### 2.2.1 Test Methods

Whole blood (Canine) was acquired within one day of collection at Chulalongkorn University, Small-Animal hospital (Bangkok, Thailand). The cell preparation protocols were started with collecting canine blood using a pipette and mixed 3 ml of whole blood with 45 ml of RBC lysing buffer into a 50 ml plastic centrifuge tube. The whole blood and lysis buffer were mixed well together using a biomixer for 5 min and then spun down at 3000 rpm and 4 °C for 20 min using centrifugation. We adapted the new protocols that could reduce the steps of washing that could reduce a risk of cell damage from centrifugation process using a pipette washing leukocytes with Phosphate-buffered saline (PBS) manually inside the plastic centrifuge tube to remove lysis buffer. They were then washed again by filling to a 50 ml plastic centrifuge tube with PBS and then centrifuge. However, this technique might loss some leukocytes by washing manually, but it is significantly useful to prevent most leukocytes from the damage of centrifugation. This protocol took about one hour with >95% cell viability and ready to be used for testing. In this experiment, the initiated concentration was diluted down to  $1 \times 10^7$  cells/mL for all experiments. It should be noted that our sample is the mix of donated blood from healthy and

unhealthy dogs. To control the quality of sample, it will not be used in our experiment if cell viability of leukocyte is lower than 90%.

For the cell viability measurement, Trypan Blue assay (TB) (Hyclone™, GE Healthcare Life Sciences, Chicago, IL, USA) was used, since it is the gold standard for identification of the dead/alive cells. To verify cell death, Trypan Blue assay was performed under the standard protocols to test cell viability. The numbers of dead cells are visually inspected and enumerated using a hemocytometer (Blood Counting Chamber Bright Line and Cover glass) (Boeco, Hamburg, Germany). A dead cell appears as a dark feature with a circle, whereas alive cell appears as a bright feature with a circle (Figure 2.4). Cell suspension after the preparation is set aside as control condition. It showed that the percentage of leukocyte viability of the controls were about 96%. In this work, the samples were counted in three sets and examined three times for each condition. The percentage of cell viability was then calculated. The total number of cells counted for the Trypan blue test was about 35,000 cells.

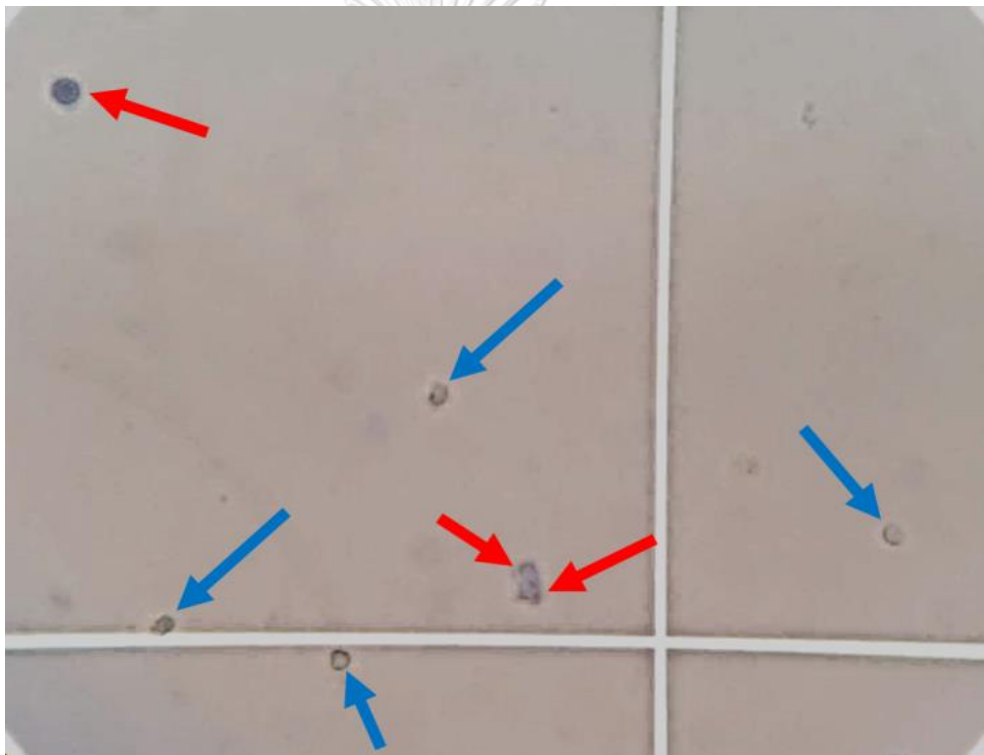


Figure 2.4 Cell features were observed under a light microscope—viable cells (blue arrows) and non-viable cells (red arrows)

For the cell deformation measurement, Scanning Electron Microscopy (SEM) (JSM-IT-500HR, JEOL Ltd., Tokyo, Japan) is used for investigating of cell morphology. The SEM protocol was started with preparing samples for Scanning Electron Microscopy using leukocyte suspension obtained from whole blood. One drop (50  $\mu$ l) of leukocyte suspension was gently placed with a pipette on a cover slip and left for 2 min at 25 °C. It is noted that the suspension should be all over the plate. Specimens were fixed with 2.5% glutaraldehyde in 0.1 M phosphate buffer pH 7.2 for 1 h. Specimens were washed twice with phosphate buffer to remove glutaraldehyde, and then once with distilled water for 5 min/each. Dehydrating specimen with a



graded series of ethanol (30%, 50%, 70%, 95% 5 min/each and 100% three times, 5 min/time, respectively). Fluid was removed from the specimens by evaporating with high-pressure heating to the critical point dryer (Leica model EM CPD300, Austria). The specimen was mounted onto stubs with conductive tape and coat with gold (sputter coater, Balzers model SCD 040, Germany). Finally, they were observed by means of SEM. In this study, we define “normal cell” to refer to cells in a circular shape (Figure 2.5). For the term “degenerated cells” refers to cell deformation, membrane damage and nucleus stretching (Figure 2.6). It should be noted that the Figure 2.5 (right-below picture with blebbing of cells) will be considered as a normal cell in this study. However, blebbing cells are the form of Apoptosis of cell death but in this case, Apoptosis was not caused by the effects of stress but by the unhealthy sample instead. Figure 2.7 demonstrates normal and degenerated cells in the field after flowing through the device. Six images were taken from four sets in each condition, and the numbers of normal cells and degenerated cells were counted. In this work, the samples were counted in three sets and examined three times. The total numbers of cells for SEM investigation were about 33,000 cells.

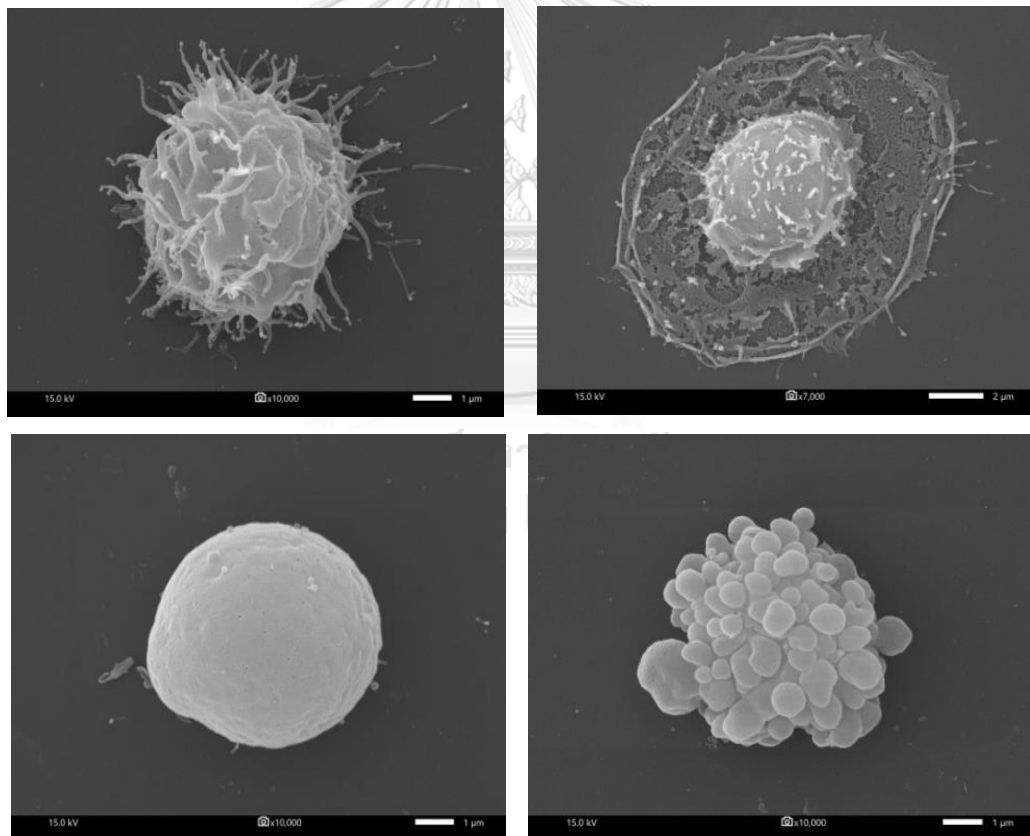


Figure 2.5 Normal cells observed using SEM

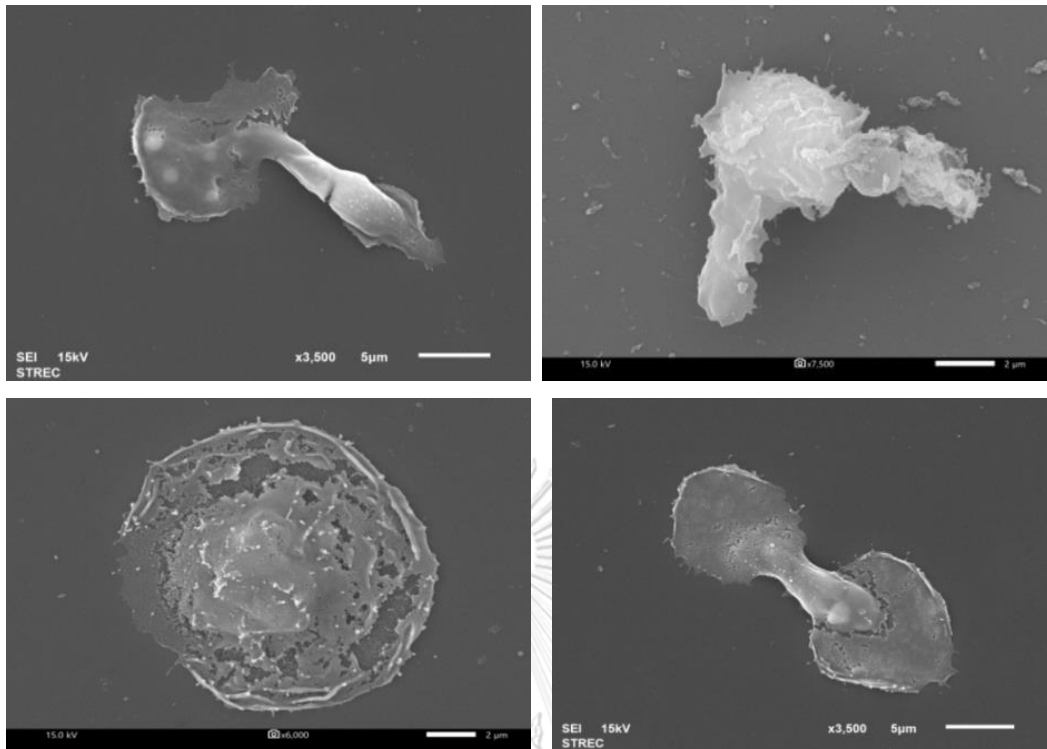


Figure 2.6 Degenerated cells observed using SEM

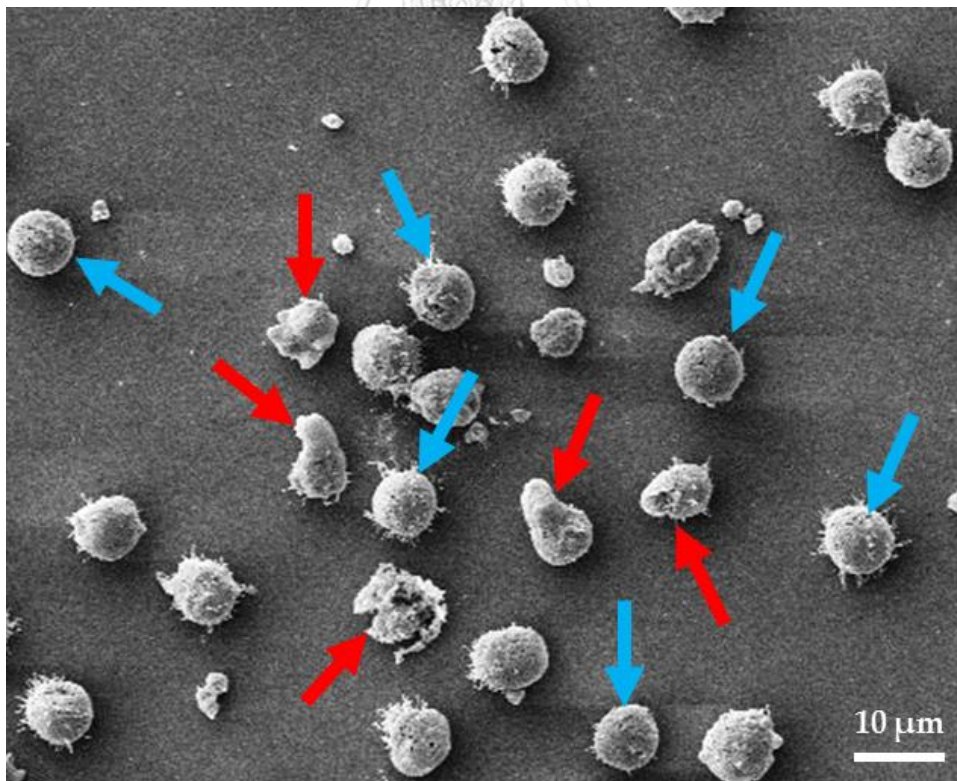


Figure 2.7 Example the image of normal (blue arrow) and degenerated cells (red arrow) observed using SEM

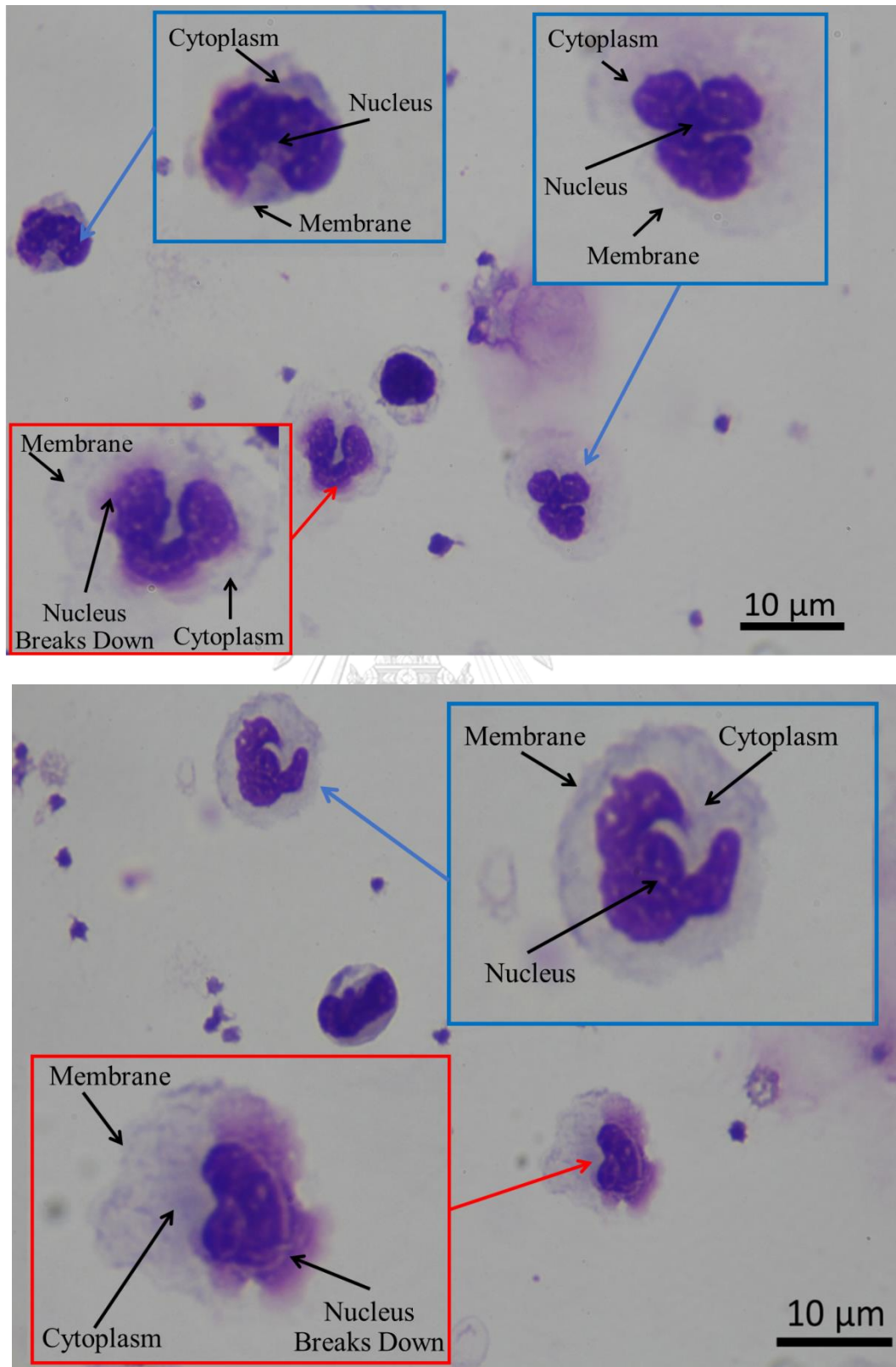


Figure 2.8 Normal cells (blue arrow) and degenerated cells (red arrow) observed using Wright-Giemsa stain

For the intracellular structure measurement, Wright-Giemsa stain (WG) is a tool that allows us to observe intracellular structures including cell membrane, cytoplasm and nucleus. The Wright-Giemsa stain protocol was started with smearing thoroughly leukocytes on glass slide and completely dried with dry air without heat. Placing Wright-Giemsa stain in a Coplin jar and filled another Coplin jar with phosphate buffer. Fixing smears in absolute methanol for 10-15 s and completely dried with dry air again. Staining smears in Wright-Giemsa stain solution for 10-15 s and rinsed stained smears with Phosphate Buffer for 10-15 s and dried the smears with dry air. Permanent mounts can be made. Finally, examining stained smears under a microscope. In order to avoid any confusion of interpretation, here, “normal cells” is used to refer to cells that are in a circular shape, and consist of three main structures—cell membrane, cytoplasm and nucleus. The term “degenerated cells” refers to cells that miss one of the three main structures (Figure 2.8). In the tests, leukocytes were spread thinly onto a glass slide, and then, 100 cells were randomly chosen and classified as normal or degenerated cells under a light microscope. The samples were counted in three sets and examined three times. The total number of leukocytes for Wright-Giemsa Stain investigation was about 17,000 cells.

### 2.2.2 Feeding System and Test Conditions

Generally, the experiments of all cases were set. The sample was loaded in the feeding system mounted on syringe pumps (F-100, Chemyx, Stafford, TA, USA) and injected through the setup of the devices. Furthermore, separation process was microscopically observed and recorded in a computer and then the samples were collected in microtubes to further investigation. In our investigation, the feeding system was examined without the sorting device.

One of the biggest challenges is to maintain and prolong cell viability on the site of delivery. Therefore, the possibility of cell damage or loss in feeding system including syringe, needle and silicone tube must be investigated initially. In this test, three different sizes of syringe—1, 2.5 and 5 ml—were tested with a length of 59.89 mm and an inner barrel’s diameter of 4.61, 7.29 and 10.30 mm attached to a 22 G needle with an inner diameter of 0.41 mm and a length of 1.5 cm. The tip of needle was also connected to a tube (Clear C-FLEX Tubing, Cole-Parmer Instrument Company, Vernon hills, IL, USA) with a length of 20 cm and with an outer and inner diameter of 0.72 and 0.41 mm. The feeding system was examined at various flow rates: 0, 0.3, 1, 5 and 8 ml/min (Figure 2.9).

### 2.2.3 Spiral Microchannel and Test Conditions

Spiral microchannel consisted of five loops with two inlets. The width of 500  $\mu\text{m}$  and the height of 130  $\mu\text{m}$  were fixed with the average radius of curvature of 0.75 cm and increasing at a constant rate of angle. The outlet was divided into two parts; the straight channel with a length of 10 mm with a gradual expansion connected to the 10 outlets (Figure 2.10). Each outlet was designed with the width of 200  $\mu\text{m}$  at the same height. The experiment was examined at two conditions: 2 and 10 ml/min. At the flow rate of 2 ml/min (1 ml/min at each inlet) was the optimum condition that provided the highest efficacy of cell separation (10, 15 and 20  $\mu\text{m}$  in diameter). At the flow rate of 10 ml/min (5 ml/min at each inlet), the spiral chip could withstand this

flow rate without leaking or ruining the device. The samples were collected in microtubes at the 10 outlets after flowing through the complete setup.

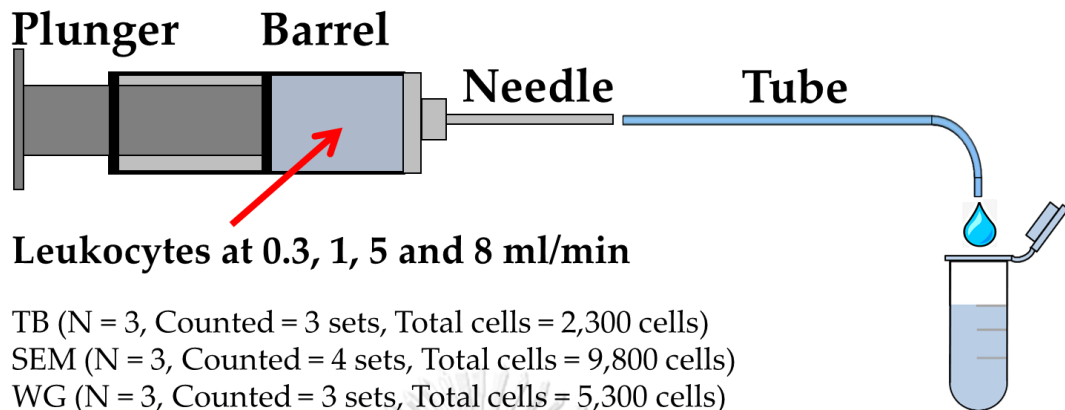
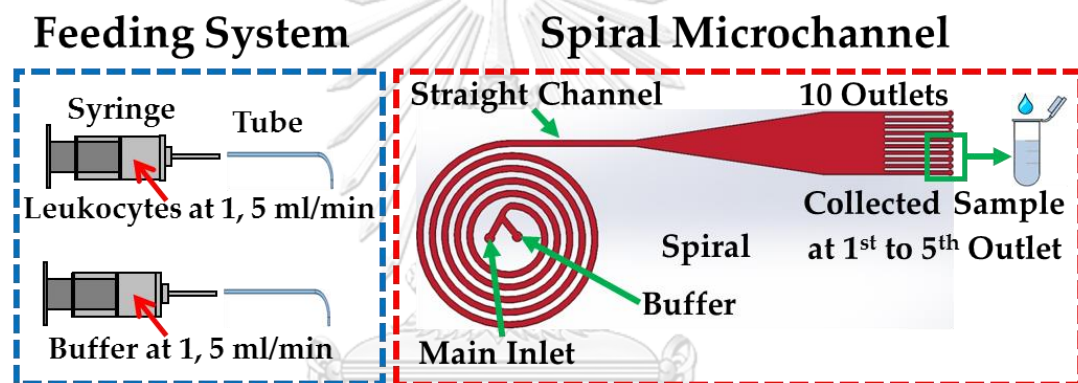


Figure 2.9 Schematic drawing of feeding system: syringe, needle and silicone tubes.

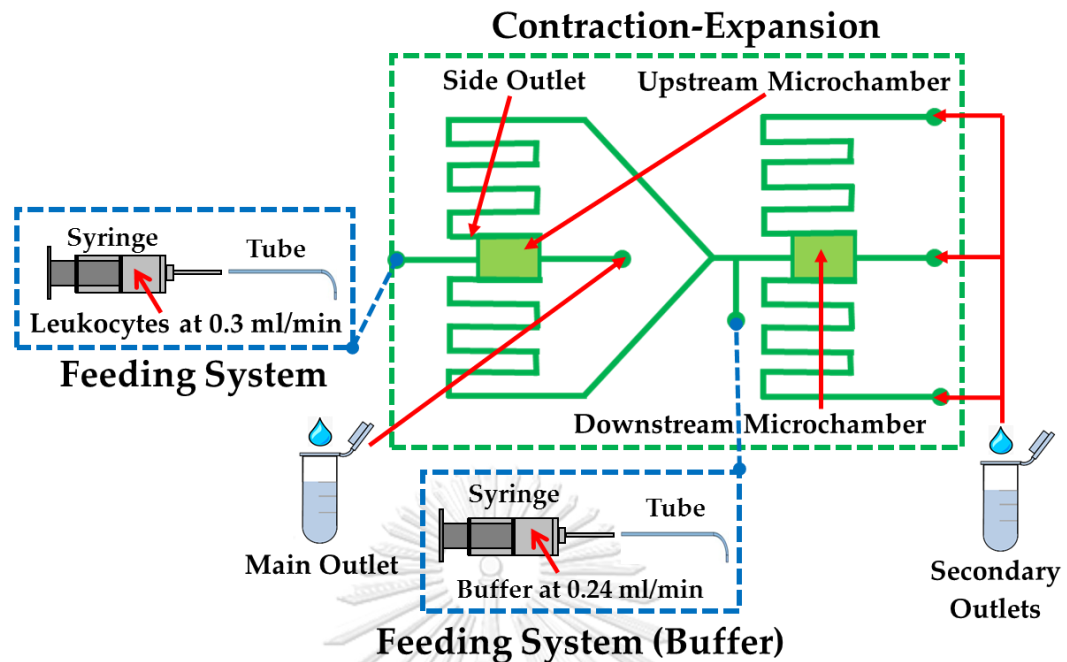


TB (N = 3, Counted = 3 sets, Total cells = 21,200 cells)  
SEM (N = 3, Counted = 4 sets, Total cells = 14,700 cells)  
WG (N = 3, Counted = 3 sets, Total cells = 4,800 cells)

Figure 2.10 Schematic drawing of complete setup of spiral microchannel devices and the setup of spiral microchannel including feeding system: syringe, silicone tubes, needle and spiral microchannel: straight channel and outlets.

#### 2.2.4 Contraction-Expansion Array (CEA) Systems and Test Conditions

For the CEA setup, there are two contraction-expansion chambers, namely the upstream and downstream microchamber. The CEA consisted of the square channel of 50  $\mu\text{m}$  connected to the expansion chamber downstream with the width of 500  $\mu\text{m}$  (Figure 2.11). On both sides of the upstream microchamber, there were two side outlets connected to the downstream microchamber to sort cells with a higher efficacy and purity. The experiment was examined at 0.3 ml/min in the main and 0.24 ml/min in the buffer inlet. These flow conditions were the optimal condition with which the system could separate the cells of 10, 15 and 20  $\mu\text{m}$  with a high efficacy. Similar to the other cases, the samples were also collected in microtubes after flowing through the complete setup.



TB (N = 3, Counted = 3 sets, Total cells = 7,600 cells)  
 SEM (N = 3, Counted = 4 sets, Total cells = 8,600 cells)  
 WG (N = 3, Counted = 3 sets, Total cells = 1,800 cells)

Figure 2.11 Schematic drawing of the complete setup of contraction–expansion microchannel array: feeding system and CEA

In this work, the experiments were divided into three examines (1) the feeding system by increasing volume syringe of 1, 2.5 and 5 ml and increasing flow rates at 0, 1 and 8 ml/min (2) the total setup of spiral microchannel at 2 and 10 ml/min and (3) the total setup of CEA at 0.3 and 0.24 ml/min in the main and secondary chamber, respectively. These three cases were examined under three methods: Trypan Blue, SEM and Wright-Giemsa stain to investigate cell viability, cell morphology and intra cellular structures.

## 2.3 Simulation

### 2.3.1 Simulation of Feeding System

Feeding system in this work refers to syringe, needle and tube which introduces sample to the sorting device. In cell therapy studies, sample or drug delivery is one of the most important parts through injection because fluid force acting on cells may lead to the cause of cell damage or death during injection. Consequently, feeding system is necessary to be considered to prevent and prolong cell viability as much as possible.

The medium (PBS) was assumed to be water with density of  $998 \text{ kg/m}^3$ , viscosity of  $0.001005 \text{ Pa}\cdot\text{s}$  [130], the flow was considered as laminar flow and temperature was set at 293 K. The steady state for incompressible fluids was defined. In addition, there is no slip boundary condition for the walls in all cases.

The computational model was set up with a 2D representation of a syringe and needle. The geometry of syringe was simulated from the glass syringe of Hamilton Gastight High-Performance with the volume of 5, 2.5 and 1 ml with a straight needle of 20G (Table 2.1). The length of syringe barrel was kept constant in all designs and the angle between the syringe barrel and attached needle was also kept at 90°. To ensure that all boundary and conditions are correct and proper, this simulation was validated with the simulation of Syntouka et al., Down et al. and Yen et al. [28, 30, 130] 2D axisymmetric simulation was used to reduce computational time consuming. Geometry of syringe was designed as two rectangles unionized and revolved to build a barrel's geometry and needle. The extremely fine mesh was created for all areas of syringe. Corner refinement and distribution were also employed in specific areas to provide more accurate data, especially at the corner between barrel and attached needle as shown in Figure 2.12. The inlet flow was defined as a uniform flow which Normal inflow velocity was chosen at the inlet 0.2 mm/s (1 ml/min) and 1.6 mm/s (8 ml/min). At the outlet, pressure at the cross section was uniform as well as no pressure differences and suppress backflow were assumed. The numbers of meshes were about 20 million for this design. Preliminary simulation, grid dependency analysis based on the maximum stress at the corner was implemented. However, WBCs are around 7-12  $\mu\text{m}$  in diameter which are smaller than initiated size of dependent grids. For this reason, it was decided to add more meshes ( $<1 \mu\text{m}$ ) at the corner in order to compare the size of high stress area to the size of WBCs. As reported by the study of Syntouka et al., Down ea al., Yen et al. and Aguado et al. [28-30, 130], they suggested that the extensional stress occurred when there was an abrupt change in cross section. This abrupt change from the syringe barrel to the attached needle caused a significant increase in linear velocity. According to our simulation, the numbers of meshes  $\sim 20$  million can help us to analyze and compare the sizes of WBCs to the size of maximum stress areas at the corner in our study. It is noted that four paths—1#, 2#, 3# and 4# were represented as streamlines in the syringe and the magnitude of stresses were represented in terms of total extensional and shear stress component of stress tensors across the same geometry including axial and radial extensional and shear components of stress tensors induced at the corner of syringe as display in Figure 2.13.

Table 2.1 Dimension of actual syringes of 1, 2.5 and 5 ml.

Syringe's Volume (ml)	Barrel's Length (mm)	Barrel Inner in Diameter (mm)	Needle's Length (mm)	Needle inner in Diameter (mm)
1 ml	59.89	4.61	51.00	0.41
2.5 ml	59.89	7.29	51.00	0.41
5 ml	59.89	10.30	51.00	0.41

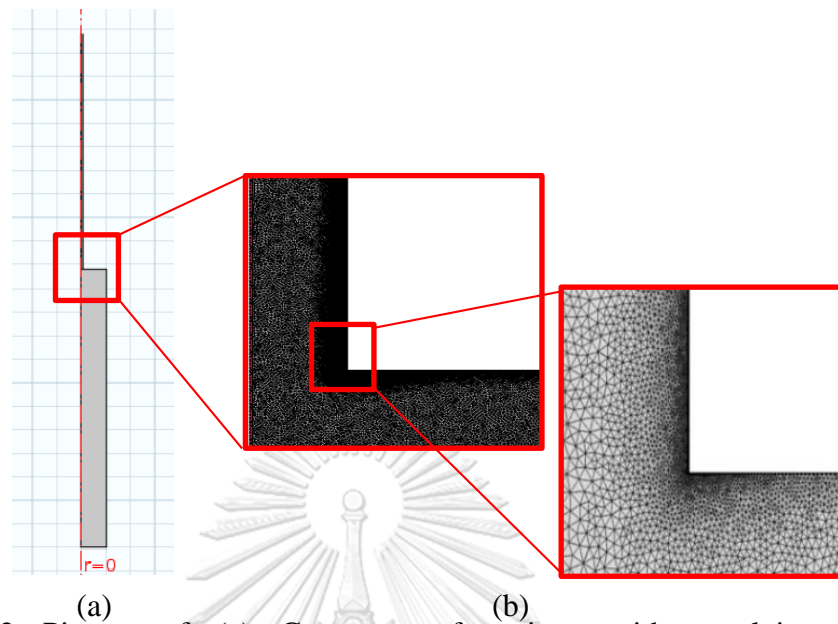
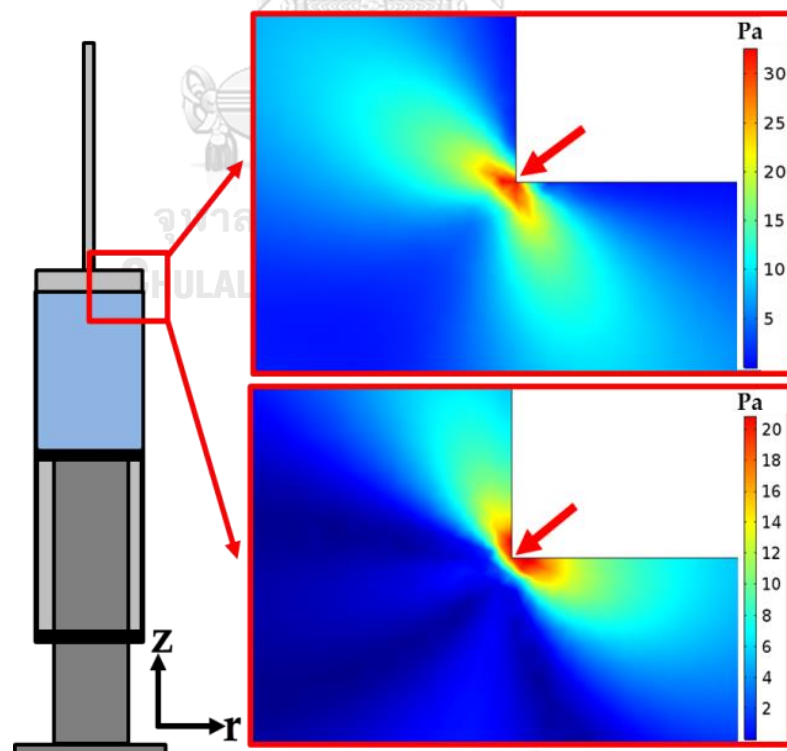


Figure 2.12 Picture of (a) Geometry of syringe with revolving and (b) Corner refinement and Distribution function.

## Maximum Extensional Stress



## Maximum Shear Stress

Figure 2.13 Example of contour—total extensional and shear component of stress tensors, the maximum stresses exerted at the corner of syringe.



### 2.3.2 Simulation of Spiral Microchannel

Spiral microchannel is the second main component of the device referring to spiral, straight channel and outlets in the assembly. The geometry of spiral microchannel and flow rate is the main factors that dominate the efficiency of separation. In general, introducing a high flow rate would create Dean drag force that helps focusing streamlines move separately and widely. However, using a high flow rate can exert extensional and shear stresses in the sorting device. In this reason, spiral microchannel is also needed to investigate stresses that may affect cell viability.

The medium (PBS) was assumed to be water with density of  $998 \text{ kg/m}^3$ , viscosity of  $0.001005 \text{ Pa}\cdot\text{s}$ , the flow was considered as laminar flow and temperature was set at  $293 \text{ K}$ . No slip boundary condition function was selected. The steady state for incompressible fluids was defined.

In the actual spiral microchannel, it was designed with the width and height of about  $500$  and  $130 \text{ }\mu\text{m}$  and the radius of curvature was about  $750 \text{ }\mu\text{m}$  with 5 loops consisting of a straight channel and 10 outlets. However, due to the computational limitation and time consuming, it was simulated only 1 loop spiral as shown the computational domain in Figure 2.14a. The flow inlet was defined as a uniform flow which Normal inflow velocity was chosen at the inlet ( $0.2564 \text{ m/s}$ ). At the outlet, pressure at the cross section was uniform as well as no pressure differences and suppress backflow were selected. The outlets were modeled into two parts; the straight channel that was designed with the length of  $10 \text{ mm}$  to allow the flow to be fully developed and the length of the outlet was  $20 \text{ mm}$  followed by an expanding output diverging at an angle of  $9^\circ$  that splits into five symmetry outlet sub-channels as shown in Figure 2.14b. Grid dependency analysis based on the maximum stress in the middle of spiral channel was employed. The extra fine mesh was created for all areas in spiral microchannel and corner refinement function at the corners of spiral, inlets and outlets were selected in order to provide more accurate data. Finally, the maximum and minimum element sizes for spiral microchannel were  $13.90$  and  $0.91 \text{ }\mu\text{m}$  and for straight channel and outlets were  $2.5$  and  $2.5 \text{ }\mu\text{m}$ . The final number of meshes of spiral and straight channel was about 9 and 3 million meshes, respectively. Due to the visualization of stress in spiral microchannel, extensional and shear components of stress tensors were also represented with nine components in the middle of the channel. Figure 2.15 showed the example of total extensional and shear stress component of stress tensors.

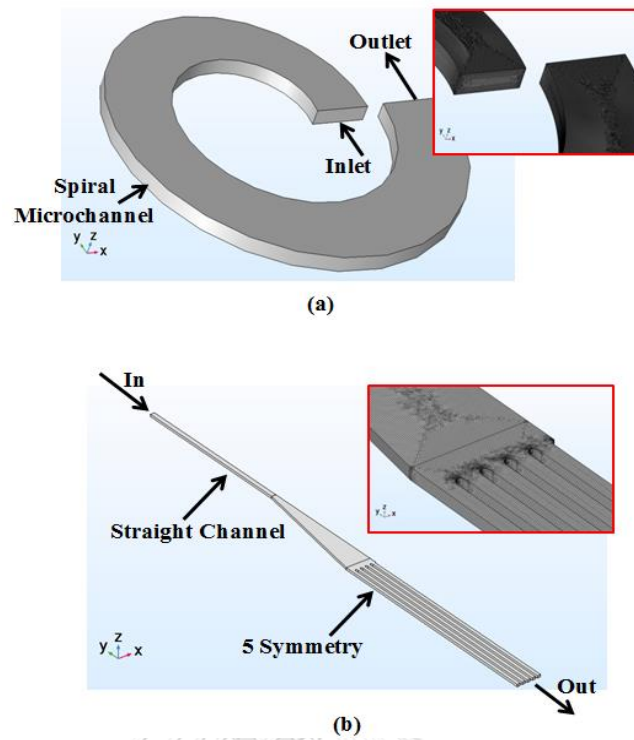


Figure 2.14 Picture of (a) Spiral microchannel and (b) straight and 10 outlets

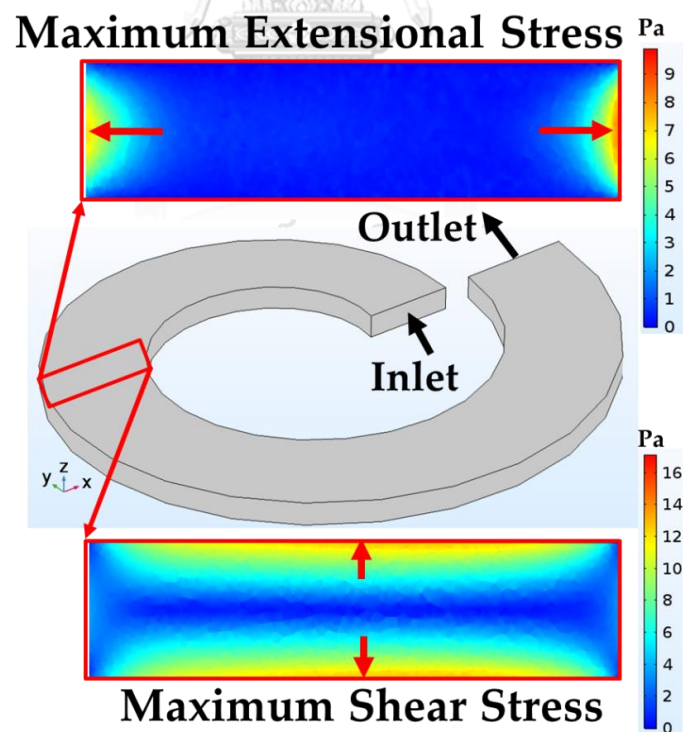


Figure 2.15 Example of contour—total extensional and shear component of stress tensors in the spiral channel, the maximum stresses exerted at the walls of the channel.

### 2.3.3 Simulation of Contraction-Expansion Microchannel Array

Contraction-Expansion microchannel array is another sorting device utilizing the balance of Dean drag and inertial lift forces that separate different size of cells. Using low flow rate, according to the experiment, there were some dead cells, deformation and intracellular damage slightly occurring during the process of separation. For this, the computational simulation was also implemented to investigate the magnitude of stresses, the size of stress areas and exposure time that may affect cell viability, extra and intracellular changes potentially.

Like syringe and spiral microchannel simulation, a steady state with a constant inlet was used in CEA simulation as well. The flow was considered as laminar and temperature was set at 293 K. There was no slip boundary condition at the walls. The medium was defined as water with density of  $998 \text{ kg/m}^3$  and viscosity of  $0.001005 \text{ Pa}\cdot\text{s}$ .

The main channel of CEA was designed as a straight channel with the width and height of about  $16,500$  and  $25 \text{ }\mu\text{m}$ . The main and secondary chamber had the same size of  $500$  and  $50 \text{ }\mu\text{m}$  in length and depth. However, to reduce time consuming, it was simulated as symmetry in x-y and x-z axis with  $250$  and  $25 \text{ }\mu\text{m}$  as shown the computational domain in Figure 2.16. The flow inlet was defined as a uniform flow which Normal inflow velocity was chosen at  $0.3 \text{ ml/min}$  ( $2 \text{ m/s}$ ). As for the velocity of outlet, the outlets were modeled into two parts: the main and secondary outlets. According to the secondary outlet, the velocity of fluid was fixed at  $0.14 \text{ m/s}$  by extending the length of secondary channel until the velocity became  $0.14 \text{ m/s}$  corresponding to the optimum condition in our experiment.

In order to obtain reliable data, it is important to do grid independence by increasing the number of meshes until the results do not depend on the grids. The grid size was customized which was smaller than extremely fine and corner refinement function also was chosen at the corners of CEA (Figure 2.17). The maximum and minimum element sizes were  $6.225$  and  $0.096 \text{ }\mu\text{m}$  for all domains of CEA. The final number of meshes of CEA was about 9 million meshes. Due to the visualization of stress in CEA, total extensional and shear component of stress tensors were illustrated with nine components at the main chamber as shown in Figure 2.18.

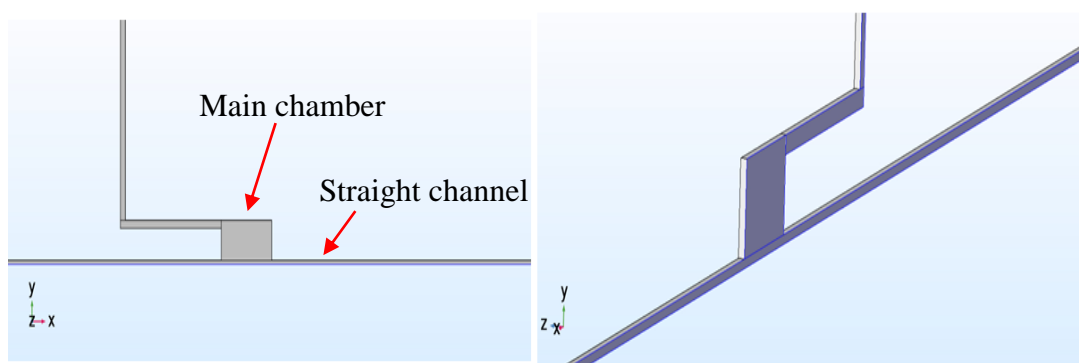


Figure 2.16 Picture of CEA: symmetry domain in x-z axis (left) and symmetry domain in y-z axis (right)

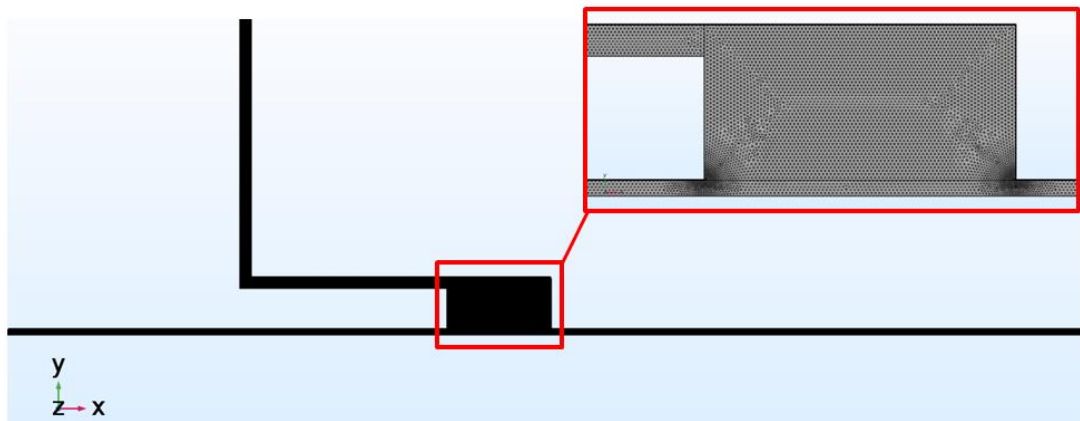


Figure 2.17 Geometry of CEA's chamber with corner refinement and distribution function.

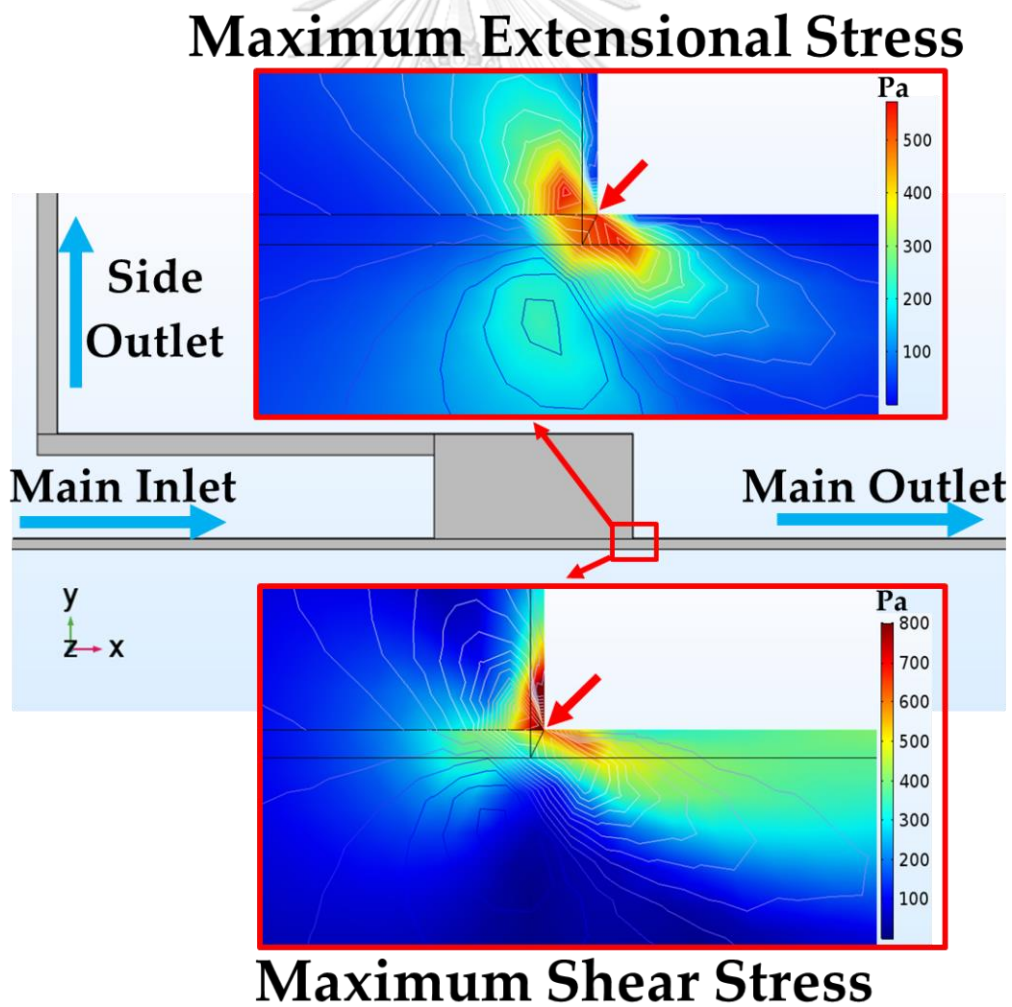


Figure 2.18 Example of contour—total extensional and shear component of stress tensors in the CEA's chamber, the maximum stresses exerted at the corner of CEA.

To gain insight into the effect of stresses on cells in each component, the results of each experiment will be analyzed by using a computational simulation including the evaluation of the extensional and shear components of stress tensor, exposure time and the critical areas. For these advantages of simulation, we will be able to understand the causes of cell damage and loss in each component including feeding system, spiral microchannel and CEA.

## 2.4 Results

### 2.4.1 The Results of Feeding System

The experimental results showed that, in the feeding system, increasing the ratio of the abrupt change in cross section between barrel and nozzle by increasing the volumes of syringe of 1, 2.5 and 5 ml but the flow rate was fixed at 1 ml/min, the percentage of normal cells was  $96.6\% \pm 1.6\%$  (control), resulted in  $96.7\% \pm 1.7\%$ ,  $98.7\% \pm 0.8\%$  and  $93.7\% \pm 2.9\%$  of cell viability. Likewise, increasing extensional stress by increasing flow rates of 1, 5 and 8 ml/min but the 5 ml syringe fixed, the percentage of normal cells was  $96.0\% \pm 1.5\%$  (control), resulted in  $96.8\% \pm 0.7\%$ ,  $96.5\% \pm 1.6\%$  and  $96.8\% \pm 1.6\%$  cell viability. Therefore, either increasing the volumes of syringe or increasing flow rates, cell viability in these both conditions were not significantly different from the controls under a light microscopy with a trypan blue assay. The data of SEM showed that normal cells were decreased from  $97.6\% \pm 1.3\%$  to  $94.5\% \pm 2.4\%$ ,  $93.8\% \pm 2.2\%$ ,  $90.2\% \pm 2.8\%$  and  $87.4\% \pm 5.3\%$  at 0.3, 1, 5 and 8 ml/min, respectively. This results also agreed with the study of Bea et al. [32], they found that cells were more deformed as the flow rate increases in the extensional flow. In addition to Wright-Giemsa stain test, it was found that the percentage of normal cells was decreased from  $96.8\% \pm 3.0\%$  to  $95.6\% \pm 1.6\%$ ,  $94.1\% \pm 2.0\%$ ,  $91.2\% \pm 2.3\%$  and  $89.0\% \pm 3.2\%$  at 0.3, 1, 5 and 8 ml/min, respectively (Figure 2.19).

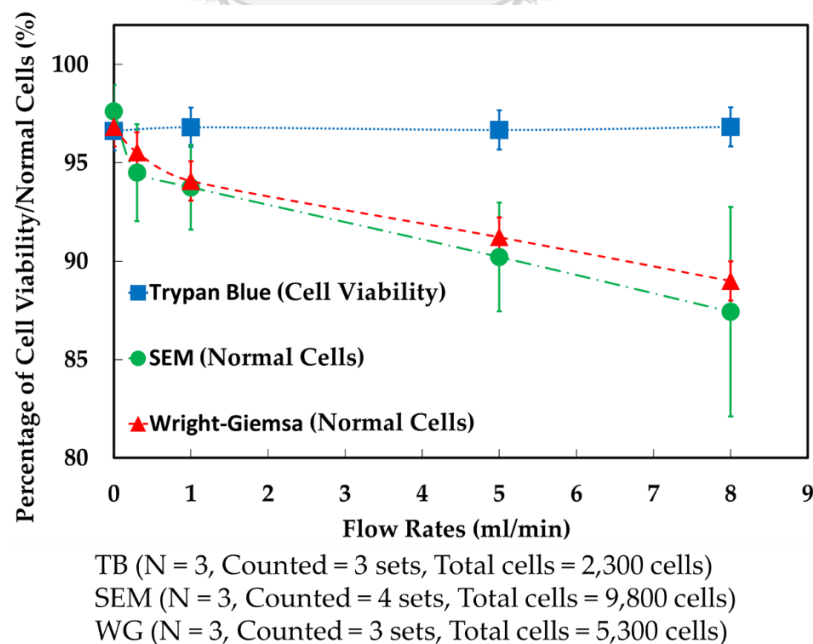


Figure 2.19 Percentage of cell viability, cell morphology and intracellular structures in feeding system with increasing flow rates.

In this study, the magnitude of stresses was represented as stress tensor. However, for ease of understanding the types of stress, we divided the stress tensor into two types of stress: total extensional components of stress tensor (the root sum squared of all extensional components of stress tensor) and total shear components of stress tensor (the root sum squared of all shear components of stress tensor).

The results showed that the magnitude of the total extensional components of the stress tensor was about 24 Pa (Figure 2.20a), while total shear components of stress tensor decreased to 5 Pa at the corner (along path 1 at 1 ml/min), but exposure time was only 0.25 ms (exposure time was calculated, i.e.,  $2.5 \mu\text{m}/0.01 \text{ m/s} \approx 0.25 \text{ ms}$ ) at the corner between a barrel and needle— $2.5 \times 2.5 \mu\text{m}^2$  (for path 1) and about 0.175 ms (exposure time was calculated, i.e.,  $3.5 \mu\text{m}/0.02 \text{ m/s} \approx 0.175 \text{ s}$ )— $3.5 \times 3.5 \mu\text{m}^2$  (for path 2). As can be seen from the stress area, highest stress area of  $2.5 \times 2.5 \mu\text{m}^2$  was smaller than the size of leukocytes. Therefore, the small area of high stresses ( $>24 \text{ Pa}$  for extensional stress and  $>5 \text{ Pa}$  for shear stress) may not affect cell viability after cells flowing through in this area. In addition, the needle size is around  $410 \mu\text{m}$  in diameter; therefore, only small groups of cell could flow through in this high stress area.

In addition to have a better understanding of which type of stress is dominant throughout the part of device, the average total stress components of stress tensor were also calculated by averaging the root sum squared of all extensional or shear components of stress tensor along the streamline of all four paths (Figure 2.20c). In this way, we will be able to understand which types of stress is dominated in each streamline. Figure 2.20c shows that average total extensional was higher than shear components of stress tensor for all four paths at 1 ml/min. This implied that extensional stress was dominant throughout all streamlines especially at the corner of the syringe.

In the case of increasing the flow rate to 8 ml/min, the data showed that the total extensional components of the stress tensor increased to 500 Pa at the corner, while exposure time was significantly reduced to 0.0125 ms (exposure time was calculated, i.e.,  $2.5 \mu\text{m}/0.2 \text{ m/s} \approx 0.0125 \text{ ms}$ ) (Figure 2.19b) and it was higher than the total extensional components of stress tensor at 1 ml/min by 20 times. In contrast to the flow rate of 1 ml/min, when increasing the flow rate to 8 ml/min, average total shear components of stress tensor became higher and some paths had similar magnitude to average total extensional components of stress tensor and higher by 25 times compared to the flow rate of 1 ml/min (Figure 2.20d). As a result, shear stress became significant in the feeding system when increasing the flow rate.

Additionally, the material and length of tubing were considered as well. The tubing with good biocompatibility, excellent chemical resistance and smooth surface was used to transfer the sample from a syringe to a sorting device. Furthermore, according to simulation of tubing, only shear stress was exerted about 2 Pa and extensional stress was about 0 Pa with an exposure time of 2.43 s. Cell viability, cell morphology and intracellular structures were also examined after flowing through a syringe with two cases—with and without a 20 cm tube. The result showed that tubing had no effect on cell viability and damage. Therefore, the effect of the length of tubing might be ignored in this work.

Again, cell loss was not discovered at either 0.3, 1, 5 and 8 ml/min. The results demonstrated that in the maximum stress condition (8 ml/min), cells were still viable.

Despite the high stresses, the maximum stress area was so small and even smaller than the size of leukocytes at the corner. In other words, cells experienced the maximum stress area with a short exposure time of 0.0125 ms and the paths of most cells were far away from the corner, which could be another important factor that caused the cell not to die. Therefore, the loss of cells was not found in the feeding system in our experiments. However, cell morphology and intracellular structures were slightly damaged as the flow rate increases. It is important to note that a single leukocyte can experience a wide range of stress value depending the path of the streamline in a syringe. It is reasonable to assume that the major contributor causing cell deformation and intracellular damage is the maximum stress area which covers only in a small area at the abrupt change in cross section between syringe's barrel and attached needle.

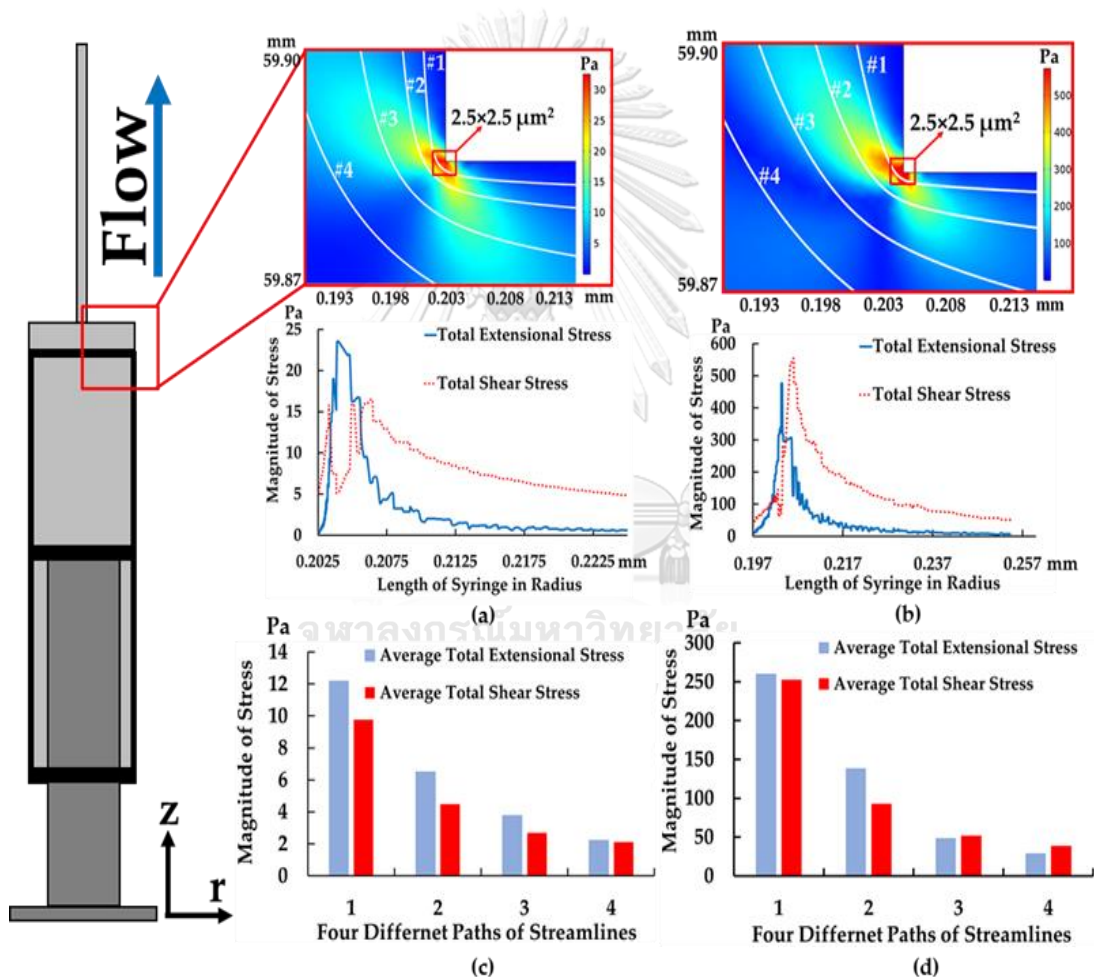


Figure 2.20 Paths of cell movement with the magnitude of extensional and shear in r-axis: total extensional and shear components of stress tensor (path 1) at (a) 1 ml/min (b) 8 ml/min and average total extensional and shear components of stress tensor along with four different paths at (c) 1 ml/min and (d) 8 ml/min ( $r = 0$  at the centerline of syringe and  $Z = 0$  at the bottom of syringe's barrel).

#### 2.4.2 The Results of Spiral Microchannel

The examination of cell viability in a complete setup of spiral microchannel, i.e., the feeding system connected with the spiral microchannel, samples were collected in microtubes and measured at only the 1<sup>st</sup> to 5<sup>th</sup> outlets. It is noted that an extremely small number of cells came out at the 6<sup>th</sup> to 10<sup>th</sup> outlets, resulting in a higher statistical error. Therefore, the 6<sup>th</sup> to 10<sup>th</sup> outlets were ignored for cells counting. The data showed that the percentage of cell viability decreased from  $95.6\% \pm 1.2\%$  to  $85.3\% \pm 6.2\%$  at 2 ml/min and comparably from  $95.3\% \pm 1.9\%$  to  $88.2\% \pm 3.3\%$  at 10 ml/min. For SEM, the statistics indicated that the percentage of normal cells decreased from  $92.2\% \pm 3.1\%$  to  $58.3\% \pm 3.2\%$  at 2 ml/min and comparably from  $94.2\% \pm 0.1\%$  to  $58.3\% \pm 10.1\%$  at 10 mL/min. For Wright-Giemsa stain, we found that the percentage of normal cells was decreased from  $95.9\% \pm 1.5\%$  to  $89.7\% \pm 3.5\%$  at 2 ml/min and further decreased from  $93.6\% \pm 1.6\%$  to  $79.0\% \pm 6.6\%$  at 10 ml/min. This implied that cell loss would majorly occur in the spiral microchannel, not in the feeding system.

According to the spiral simulation, it was discovered that, assuming that the cells started moving along the streamline in the middle of the channel, cells then migrated along the streamline in the middle of the channel and moved laterally. After that, they swirled toward the outer walls due to dean vortices on both sides of the upper half and lower half of the channel in the direction of the two counters, rotating clockwise (Figure 2.21). While travelling along the streamline, they tended to experience total extensional and shear stress components of the stress tensor. The magnitude of both stresses gradually increased and reached its maximum value. The maximum value of extensional stress was at the position of 2, 3, 5 and 6 (Figure 2.21a) on the side walls. Contrarily, the maximum value of the shear stress was at position 1 and 4 (Figure 2.21b) on the top and bottom walls.

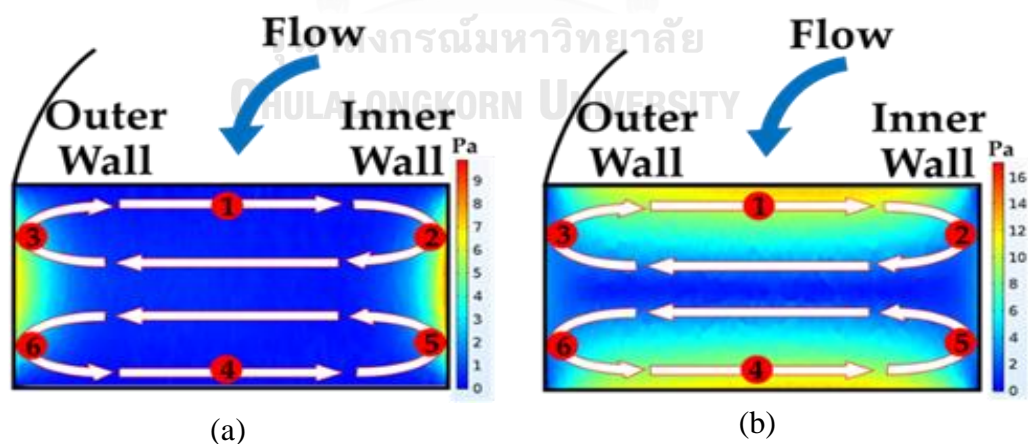


Figure 2.21 Vortices in a spiral microchannel drive cells travelling in six different locations leading to cell deformation (a) extensional stress and (b) shear stress at 2 ml/min.

According to the data for the flow rate of 2 ml/min, both total extensional and shear stress components of stress tensor gradually increased from 0 to 18 Pa in the first loop and then gradually decreased from 18 to 0 Pa in the second loop. This



movement pattern was repeated continuously until the streamline traveled to the end of fifth loop of spiral due to the secondary flow with a long exposure time of about 0.158 s (Figure 2.22a). As a result, the moderate magnitude of total extensional and shear stress components of stress tensor and a long exposure time in spiral had a possibility to cause cell loss and cell deformation during the separation process. This has a good agreement with the past work in Table 1 where the data suggest that low magnitude of shear stress but with long exposure time could cause cell damage in their experiments.

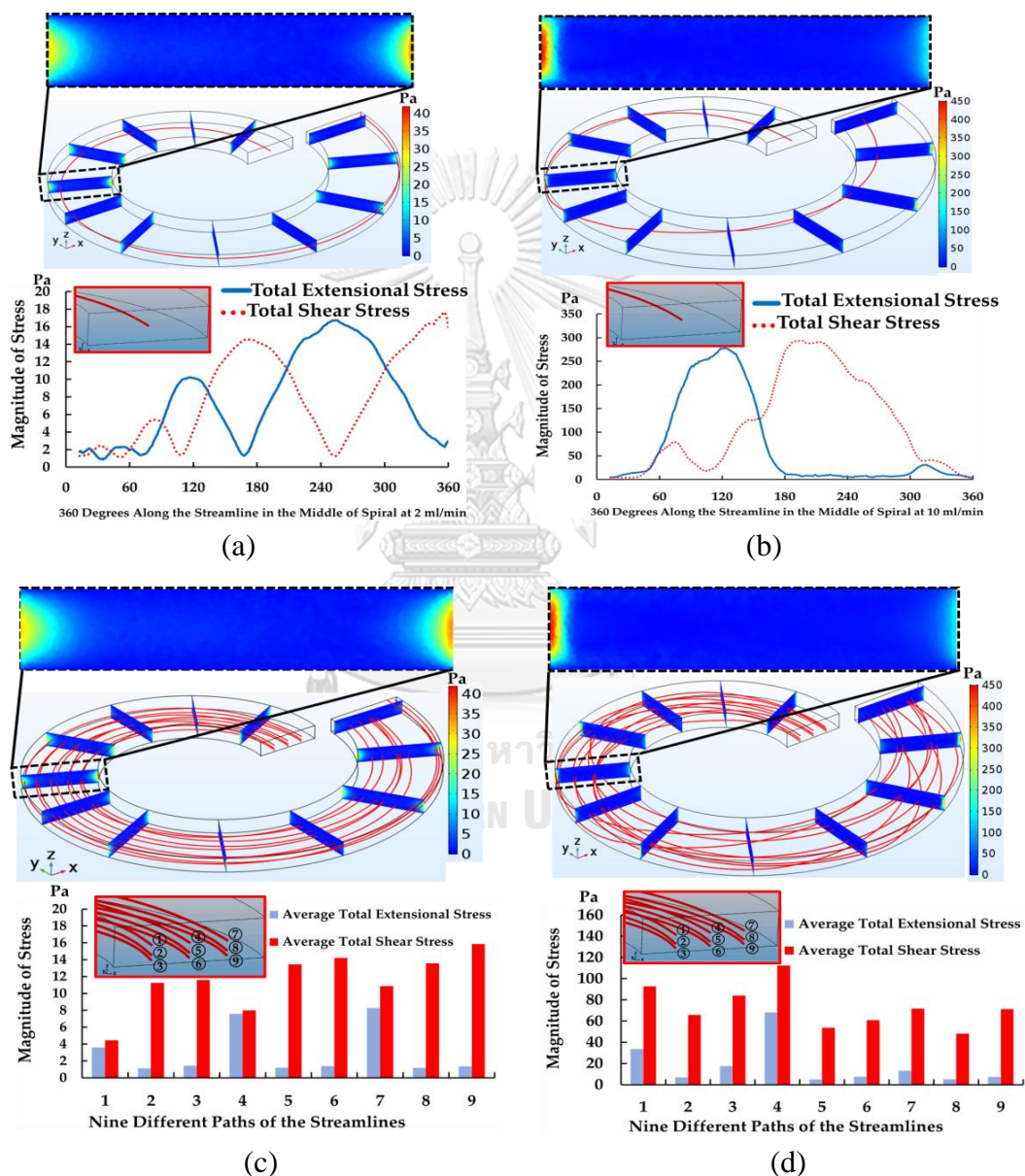


Figure 2.22 Magnitude of total extensional and shear components of stress tensor (a) at 2 ml/min (b) at 10 ml/min, along with a streamline in the middle of channel and average total extensional and shear components of stress tensor (c) at 2 ml/min and (d) at 10 ml/min along with nine different paths of the streamlines in one loop of spiral (0–360°).

In the case of increasing the flow rate to 10 ml/min, the streamline in the middle of the channel moved toward the outer wall, similar to the condition of 2 ml/min. Then, the streamline quickly moved from the outermost to the innermost wall of the channel in the first loop. This pattern of cell movement traveled more repeatedly and frequently than the condition of 2 ml/min in the same distance of the spiral microchannel. The magnitude of the total extensional and shear components of stress tensor increased from 0 to 300 Pa but the exposure time became shorter (0.032 s). Surprisingly, the magnitude of total extensional components of stress tensor began with 0 Pa at the inlet and went up to 300 Pa at 90° and went down to 0 Pa at 180° (half of a spiral). This happened because the streamline started moving from the middle of the channel and then moved toward the outer wall laterally in the streamwise direction and at the same time, it moved down to the lower half and then up to the upper half of the channel in the spanwise direction. This movement created the trends of the total extensional and shear components of stress tensor that was different from the condition of 2 ml/min. Likewise, the total shear components of stress tensor gradually increased from 0 to 300 Pa and then gradually decreased from 300 to 0 Pa at 360° (Figure 2.22b). Interestingly, two flow rates affected cell loss and the morphological change similarly.

For the simulation of the straight channel and 10 outlets, these parts connected to the spiral part as a spiral microchannel. Due to the extremely low magnitude of total extensional and shear components of stress tensor compared to magnitude of extensional and shear stress in the spiral, it is reasonable to assume that the major contributor causing cells to die is the spiral part, while the straight channel and 10 outlets were ignored.

In addition, Figure 2.22c-d demonstrated that average total extensional and shear components of stress tensor at 2 and 10 ml/min in different locations with nine streamlines were measured by averaging the root sum squared of all extensional or shear components of stress tensor along the nine streamlines. The data showed that the average total shear components of stress tensor was dominant in the spiral microchannel for all streamlines at both 2 and 10 ml/min, with exposure times of about 0.158 s and 0.032 s. Surprisingly, the average total extensional components of stress tensor in the streamline number 1, 4 and 7 at 2 ml/min and the streamline number 1 and 4 at 10 ml/min significantly increased because those streamlines moved towards the outer wall with a long exposure time. However, the average total extensional components of stress tensor of other streamlines was small due to the fact that those streamlines moved away from the walls and stayed close to the center of the channel.

To sum up, the spiral microchannel, either in the optimum condition (lower magnitude of stress with a long exposure time) or the maximum stress condition (higher magnitude of stress with a short exposure time), caused about 10% of cells to die and caused 30% cell deformation in the experiment, similarly. However, shear stress was dominant in the spiral microchannel. The data suggested that the magnitude of shear stress, the pattern of cell movement and long exposure time could be correlated with either cell damage or loss in spiral microchannel. For the damage of intracellular structures, that increased significantly when increasing the flow rate, it might be the results of the frequent occurrence of the event that cells move close to

the side wall (high extensional area) at 10 ml/min. Therefore, the possibility that cells experience high extensional stress increased and it caused the damage of intracellular in experiments became significant.

#### 2.4.3 The Results of Contraction-Expansion Microchannel Arrays

The complete setup of CEA showed that cell viability decreased from  $96.2\% \pm 2.1\%$  to  $89.3\% \pm 5.1\%$  for the main outlet and  $88.8\% \pm 10.1\%$  for the secondary outlet at 0.3 and 0.24 ml/min of the main and buffer inlet at optimum condition. SEM data also demonstrated that the percentage of normal cells decreased from  $94.9\% \pm 0.7\%$  to  $79.6\% \pm 3.8\%$  in the main outlet. For the Wright-Giemsa stain, the percentage of normal cells decreased from  $91.0\% \pm 2.7\%$  to  $75.6\% \pm 7.5\%$ .

According to the simulation of CEA, the highest extensional and shear components of stress tensor were developed during the abrupt change in cross section between the expansion and contraction region (Figure 2.23a). When cells entered this area, cells tended to be stretched suddenly at the corner and then contracted after passing through the stress area, similar to the abrupt change in the feeding system. The contour demonstrated that the total extensional components of stress tensor reached to 550 Pa while shear components of stress tensor was about 700 Pa (Figure 2.23b) and exposure time was 0.0125 ms (exposure time was calculated, i.e.,  $10 \mu\text{m}/0.8 \text{ m/s} \approx 0.0125 \text{ ms}$ ) at the upstream microchamber— $10 \times 10 \mu\text{m}^2$  (for path 1), while other paths, with an area of  $15 \times 15 \mu\text{m}^2$  (for path 3 and 4), had lower magnitude of stress compared to the path 1.

To compare with the data of CEA and the feeding system, both data showed that in CEA, the magnitude of total extensional and shear components of stress tensor were higher (550 and 700 Pa at optimum condition in path 1) than the magnitude of stress in the feeding system (500 and 550 Pa at maximum stress condition in path 1), while the maximum stress area of the upstream microchamber was larger ( $10 \times 10 \mu\text{m}^2$ ) than the area of the syringe's corner ( $2.5 \times 2.5 \mu\text{m}^2$ ) compared to leukocytes (7–12  $\mu\text{m}$ ) with the same exposure time of 0.0125 ms. Although CEA and the feeding system developed the extensional and shear stress in the same way, extensional and shear stress in CEA exerted more magnitude and a relatively larger area comparing to the entire flow channel than the feeding system in the maximum stress condition. Therefore, the higher magnitude of extensional and shear stress and larger high-stress area in CEA could cause more cell damage and loss than the feeding system in comparison.

Furthermore, the data of the Wright-Giemsa stain showed that CEA caused more intracellular damage than the spiral microchannel. This suggested that extensional components of stress tensor in CEA's microchamber caused cells to be stretched and contracted suddenly, resulting in more intracellular damage than the spiral microchannel. On the other hand, a short exposure time in the CEA's microchamber would cause less cell deformation due to the shear stress than the spiral microchannel.

According to the data of the average of total extensional and shear components of stress tensor in each path, the magnitude of both were quite similar—350, 325, 250 and 200 Pa, respectively (Figure 2.23c). It is reasonable to assume that both

extensional and shear stress are dominant equally throughout the streamlines in CEA at optimum condition.

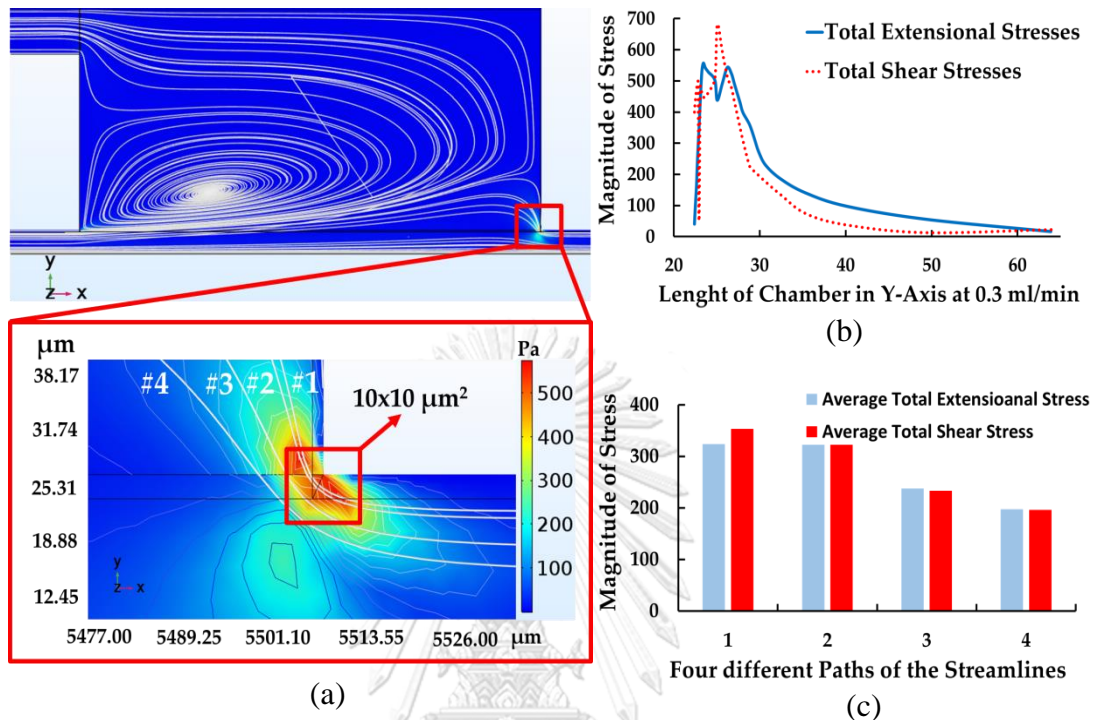


Figure 2.23 Contraction and expansion chamber at the corner. (a) Contour of extensional stress and high stress area, (b) the magnitude of total extensional and shear component of stress tensor and the height of chamber in Y-axis (path 1) and (c) the magnitude of average total extensional and shear components of stress tensor with four paths of streamlines ( $Y = 0$ , at the centerline of the main channel).

#### 2.4.4 The Summary of Spiral Microchannel and Contraction-Expansion Array

Three techniques such as Trypan Blue staining, Scanning Electron Microscopy (SEM) and Wright-Giemsa staining are employed in the experiments to evaluate cell loss, cell deformation and intracellular damage in feeding system, spiral microchannel and CEA. Furthermore, using computational simulation of flow dynamics at the same conditions, this could potentially help explain and interpret the results of stresses affecting cell viability and damage.

According to the data of feeding system, cells loss is not found in different volume of syringes or fixed the same syringe's volume but increasing flow rates because at the corner of syringe exerts extensional stress that dominates over shear stress with low magnitude, short exposure time and small high-stress area. As a result, flowing cells through in the feeding system under all conditions have no effect on cell viability. According to cell morphology and intracellular structures, degenerated cells such as the leak of membrane, stretched cytoplasm, and nucleus break down slightly increase as flow rate increases. This suggests that increasing magnitude of stresses by

increasing flow rate could possibly cause cell deformation and intracellular damage but not cell loss.

For the spiral microchannel's investigation, after flowing sample through the spiral microchannel at 2 and 10 ml/min, about 10% of cell loss is found in the device. As for cell damage, it is discovered that cell deformation significantly increases about 30% while cellular damage also increases about 2% of degenerated cells. This because shear stress dominates over extensional stress in the spiral microchannel covering the entire length of the channel close to the walls with long exposure time. This may cause cell death and significant deformation. It should be observed that in the case of 2 ml/min, spiral microchannel exerts less magnitude of shear stress with long exposure time while in the case of 10 ml/min, cells receives more magnitude of shear stress with sort exposure time due to increasing flow rate. The data of 2 and 10 ml/min provides similar results with 10% of cell loss and 30% of cell deformation. Therefore, it is believed that magnitude of stress and exposure time are relatively correlated in cell loss and damage.

Unlikely, the data of CEA shows that at 0.3 ml/min, about 7% of cell loss is found in this part while 12% of cell deformation and 14% of intracellular damage increase. According to the computational simulation, extensional stress in CEA dominates over shear stress exerting at the abrupt change in cross sectional area. Due to high flow rate, the extensional stress with extremely high magnitude covers almost entire the cross-section of the flow channel. This potentially causes intracellular damage leading to cell loss and cell damage. It should be noted that higher magnitude of extensional stress in CEA at the corner with a relatively high-stress area compared to the feeding system causes cells to receive more damage resulting the disruption of intracellular structures and consequence in cell loss.

To ease understanding of stresses affecting cell viability and damage, we summarized the data for each component of feeding system, spiral microchannel and CEA including percentage of cell loss, cell damage, type of stress, magnitude in maximum and average stress and exposure time in Table 2.2.

Table 2.2 Summarization of cell loss and damage for each component.

Component	Flow Rate (mL/min)	Cell Loss (%)	Cell Deformation (%)	Intracellular Damage (%)	Type of Stress	Maximum Stress (Pa)	Average Stress (Pa)	Time	Stress× Time (Pa•s)
Feeding System	0.3	0	3.1±3.7	1.2±4.6	Extensional	N/A	N/A	N/A	0.003
	1	0	3.8±3.5	2.7±5.0		24	12	0.25 ms	
	5	0	7.4±4.1	5.6±5.3		N/A	N/A	N/A	
	8	0	10.2±6.6	7.8±6.2		500	260	0.0125 ms	
Spiral	2	10.3±7.4	31.1±9.8	3.5±10	Shear	18	13	0.158 s	2.05
	10	7.1±5.2	28.5±14.3	9.0±13.5		300	55	0.032 s	1.76
Contractile-Expansion	0.3 (Main Inlet)	6.9±7.2 (Main Outlet)	12.2±8.2 (Main Outlet)	14.2±14.8 (Main Outlet)	Extensional and Shear	550 (Extensional)	350	0.0125 ms	0.004
	0.24 (Buffer)	7.4±12.2 (Secondary Outlet)	N/A (Secondary Outlet)	N/A (Secondary Outlet)		700 (Shear)			

\*N/A is an abbreviation in this table for the data which are not available.

As can be seen from the above data, both spiral microchannel and CEA cause cells to die about 7-10% which are not significantly different in cell loss for cell experiment. According to cell damage, cellular damage possibly cause cells to receive damage severely and even die after overtime due to the leak of cytoplasm and nucleus break down. However, cell deformation and cell death in spiral microchannel are expected that they may recover themselves as viable and normal cells after overtime and come back to viable again. Moreover, in terms of the design, spiral microchannel is less complicated than the CEA due to the complexity of calculation of the length of secondary channel for the optimum condition. Regarding these reasons, spiral microchannel is chosen to integrate with the equilateral triangular microwell array for an integrated microfluidic device in the second phase.

The second phase in chapter 3 is about the investigation of a novel microfluidic device which integrates sorting and trapping technique together. The sorting efficacy, trapping distribution, cell viability before and after flowing sample through the device and after culturing for three days will be discussed in the next chapter.



## Chapter 3

### Microfluidic Integration

The purpose of the integrated microfluidic study is to combine several techniques together with multiple functions. In this work, our integrated microfluidic device provides three functions including cell sorting, trapping and culturing in a single device which operates in one process, known as Lab-On-a Chip. According to our integrated microfluidic device, single cells are sorted based on their sizes and then they are transferred to the trapping part. Sorted cells are then trapped in this part by vortices in the equilateral triangular wells. Finally, these trapped cells are cultured continuously and formed themselves as clusters/spheroids. Therefore, the study of single cells/clusters/spheroids is necessary for further analyzing cell proliferation, division and differentiation utilizing the integrated microfluidic device.

#### 3.1 Design and Fabrication

The integrated microfluidic device was designed in an engineering program known as SOLIDWORKS. The design was divided into three main parts: spiral microchannel, expanded microchannel and trapping chambers as shown in Figure 3.1a. For spiral microchannel, it was design as an Archimedean spiral microchannel, consisting of five loops with two inlets. The width of 500  $\mu\text{m}$  and the height of 80  $\mu\text{m}$  were fixed with the average radius of curvature of 750  $\mu\text{m}$  and increasing at a constant rate of angle and connected to the expanded microchannel (Figure 3.1b). Archimedean spirals can be designed by calculating radius of curvature which is given by

$$R = r + b\theta = r + s\theta/2\pi \quad (3.1)$$

Where  $R$  is radius of curvature which is measured from the center of the channel to the inner-most wall,  $r$  is the inner-most channel radius,  $b = s/2\pi$  ( $s$  is the center-to-center spacing of spiral channels),  $\theta$  ( $\theta = \pi/4$ ) is the angle between each point where radius of the loop  $R$  is calculated. The device was developed and modified the size of microchannels based on the ratio of particle size and the height of the microchannel. After many trials, the common finding is that the ratio ( $a_p/h$ ) should be  $> 0.07$  in order to separate particles more efficiently and effectively.

The outlet was divided into two parts; the straight channel with the length of 5 mm with a gradual expansion with  $15^\circ$  connected to the five trapping chambers (Figure 3.1c). The five chambers were designed as a truncated hexagon. In order to sort particles/cells in each chamber accurately according to the previous study of spiral microchannel, all five chambers and outlets were designed with the same equality of pressure drop.

The trapping chamber was designed with the width of 9 mm, length of 11.6 mm and the height of 300  $\mu\text{m}$  for 21 microwells in each chamber (Figure 3.1d). The wells in each column were aligned as zigzag structure pattern. The well was designed

as an equilateral triangle with the length of 600  $\mu\text{m}$  and the height of 300  $\mu\text{m}$  (Figure 3.1.e) based on the size of fibroblast spheroid about 250-300  $\mu\text{m}$  in diameter (Figure 3.1.f).

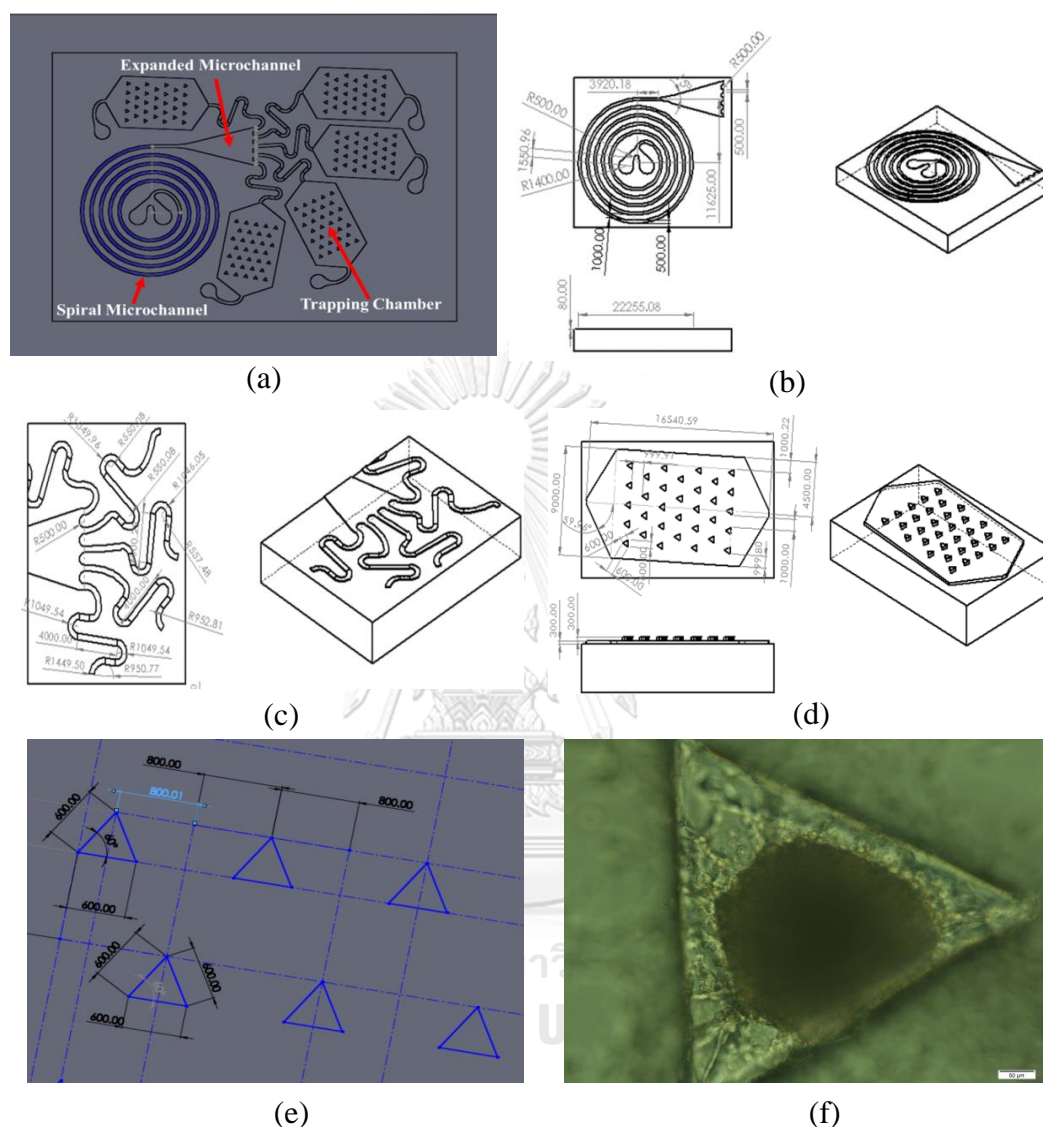


Figure 3.1 The schematics design of the device (a) the integrated microfluidic device (b) spiral microchannel part (c) expanded channel and outlets (d) trapping chamber with 21 microwells (e) microwells and (f) spheroid in a microwell

The initial flow rate was set at 0.2 ml/min as the minimal flow rate in this study. However, in order to trap particles/cells effectively, the flow rate should be 0.1 ml/h ( $V_{\text{avg}} \sim 0.0001$  m/s) in trapping chambers according to the previous study. Therefore, the initial flow rate must be decreased to be able to sort and trap particles/cells in the integrated microfluidic device. We increased the chamber area by 68 times to decrease the velocity of fluid by 68 times as well. The area of the chamber was expanded which reduced the velocity of fluid from 0.08 to 0.001 m/s. In addition, serpentine channels were created at the end of outlets to significantly increase pressure drop resulting the equivalent of pressure drop in each chamber.



After designing the geometry with SOLIDWORKS, the pattern was created on aluminum mold and then machined by computer numerical control, CNC as shown in Figure 3.2a. After that, pouring 13.2 g of PDMS (12 g of PDMS and 1.2 g of Curing Agent, 10:1) and using a hotplate with the temperature at 70 °C about 15 minutes to form the PDMS integrated chip. Finally, peeling the PDMS and pulling the PDMS gently and then bonding the PDMS with a slide glass to enclose the chip using air plasma as shown in Figure 3.2b.

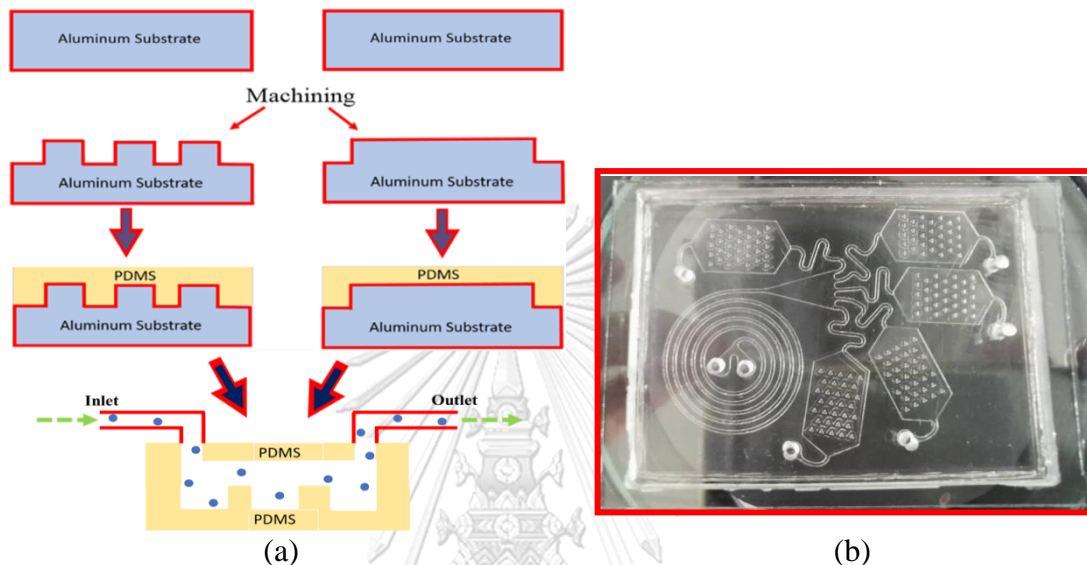


Figure 3.2 Schematic picture of (a) process flow of PDMS fabrication and (b) microfluidic assembly

Due to using a glass slide to enclose at the top of the chip, the inlets were connected at the bottom of the chip instead. As a result, it is really difficult to focus the objectives by using a light microscope. Therefore, using a stage for helping observation is really needed for this experiment. The stage was designed by engineering program with SOLIDWORKS. The designs were created on four acrylic plastic plates and then were cut by an acrylic cutting machine. After that, four acrylic plastic plates were assembled together at the corners as rectangular shape with a super glue (Figure 3.3). The integrated microfluidic device bonded with a glass slide was placed on this stage for helping focusing objectives easily under a light microscope (Figure 3.4).



Figure 3.3 The design of stage for helping focusing objectives

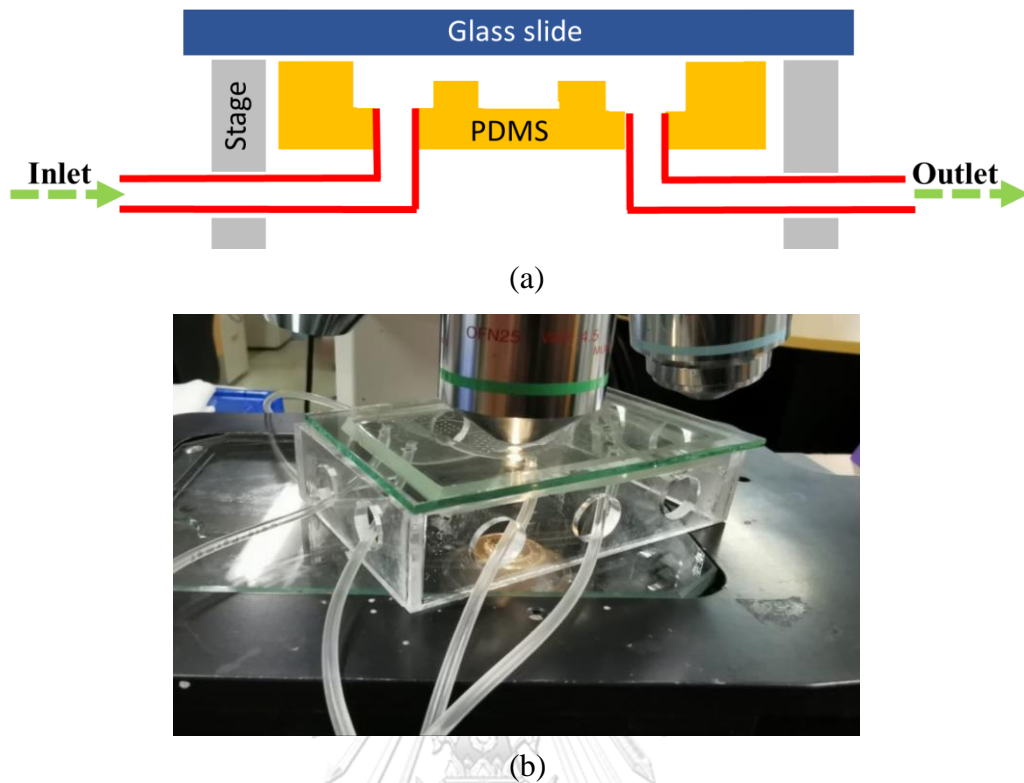


Figure 3.4 Setup of the integrated microfluidic device (a) schematic drawing setup and (b) actual setup under a light microscope

### 3.2 Experiment

The setup of integrated microfluidics consisted of two main parts: feeding system part and integrated microfluidic part as shown in Figure 3.5. In the feeding system, syringes (Nippro Disposable Syringe) of 10 ml with the needle (Nippro 20G) were connected with a silicone tube (C-Flex Tubing) of 0.05 cm in inner diameter and 10 cm long. The syringes were mounted on syringe pumps (F-100, Chemyx, Stafford, TA, USA). The experiments were examined with three types of sample including microparticles, mouse fibroblast cells (STO) and mast cell tumor cell line (LuMC). The integrated chip was microscopically observed and recorded in a computer and then the samples were collected in microtubes to further investigation.

First part, the system was tested with microbeads to obtain the optimum flow rate under different conditions. The mixture sample was loaded in a syringe and another was loaded with buffer (PBS) mounted on syringe pumps and injected through the setup of the device (Figure 3.6). Polystyrene beads of 10, 15 and 20  $\mu\text{m}$  were tested with different flow rate of 0.2, 0.5, 1 and 2 ml/min. As for the concentration of polystyrene beads, three different sizes of particles were mixed together with the same concentration of  $5 \times 10^4$  beads/ml. The number of microbeads in wells were counted and calculated in terms of the trapping distribution while the number of beads in wells, on the surface around well and at the outlets were calculated to determine the sorting efficacy.

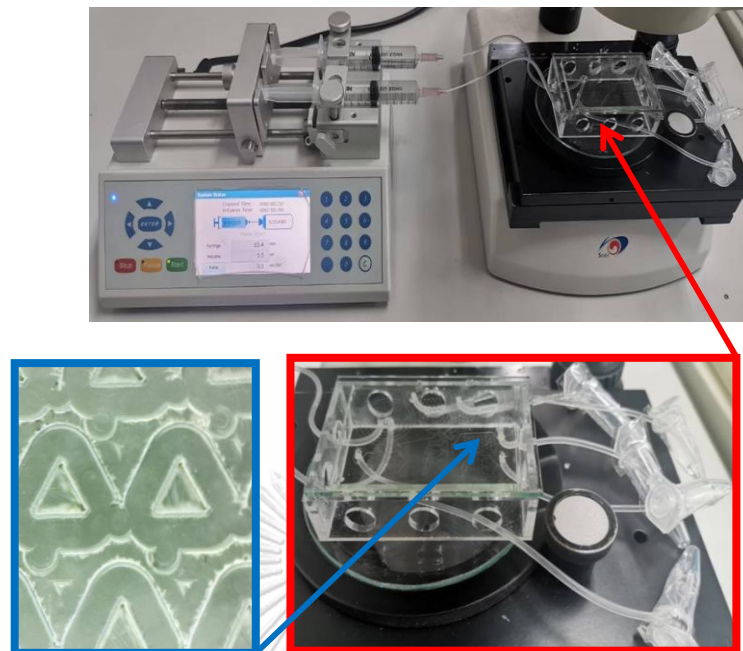


Figure 3.5 The setup of integrated microfluidics

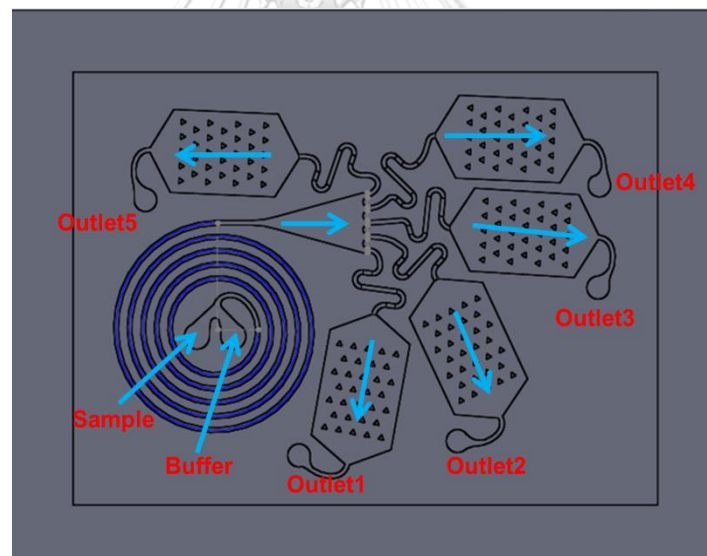


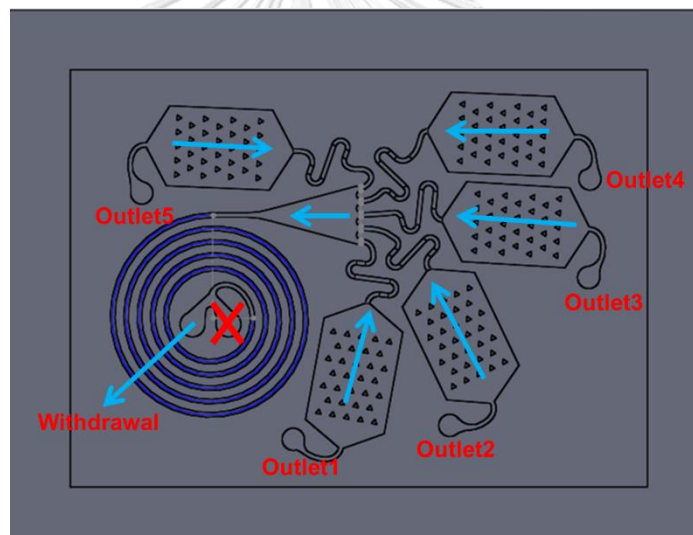
Figure 3.6 Experiment in the injection made for investigating trapping distribution and sorting efficacy

Note that, the percentage of trapping distribution is defined as the number of particles in the same size is trapped in five chambers and calculated in the percentage. For example, most particles of  $10\ \mu\text{m}$  were trapped at the 1<sup>st</sup> chamber with 90% compared to other chambers with 10%. So that, the maximal percentage of trapping distribution of  $10\ \mu\text{m}$  particles was 90% in the 1<sup>st</sup> chamber. In contrast, the percentage of sorting efficacy is defined as the number of particles is trapped in the chamber and added by the number of particles on the surface around the wells and the number of particles come out from outlets. For example, most particles are trapped in the wells, on the surface and outlets in the 1<sup>st</sup> chamber with 90% compared to other chambers

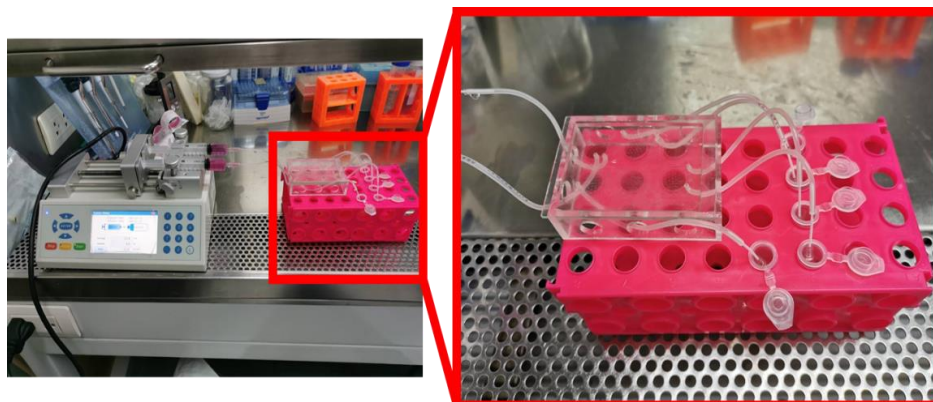
with 10%. Therefore, the maximal percentage of sorting efficacy of 10  $\mu\text{m}$  particles was 90% in the 1<sup>st</sup> chamber. For full information for cell enumeration protocols, see Appendix B4 and B5.

For cellular sample, mouse fibroblast cells (STO) were prepared as single cells. Regarding the size of STO cells (15  $\mu\text{m}$ ), the flow rate of 0.5 ml/min was chosen as the optimum condition for trapping 15  $\mu\text{m}$  particles with the concentration of  $1 \times 10^4$  cells/ml. Fibroblasts was recorded with the video recorder and then counted the number of cells in the wells and calculated them in terms of the trapping distribution as well as examined STO viability before and after flowing through the device and after culturing in the microwells for three days. Further, the images of STO culture were taken day1 and day3 in comparison.

Mast cell tumor cell line (LuMC) was also examined with the same flow rate of the previous experiment, since the size of MCT cells is also about 15  $\mu\text{m}$  with the concentration of  $5 \times 10^6$  cells/ml. In this experiment, cell viability was examined before and after flowing through the device and after culturing in the microwells for three days. Further, the images of LuMC were also taken day1 and day3 in comparison.



(a)



(b)

Figure 3.7 Experiment in the withdrawn mode for cell culture (a) schematic drawing (b) the actual setup of microfluidic integration

In every cell experiment, it was started with sterilization using an autoclave to sterilize equipment and chip. After the experiment, cell viability was tested by Trypan blue to evaluate the percentage of cell viability as well as taking images in cells in wells. After that, STO/LuMC cells were cultured for three days in an incubator at 37C° and 5% CO<sub>2</sub> and then evaluate cell viability again. To culture cells in the chip, the media was full filled in five eppendorf tubes at the outlets and then the media was withdrawn flowing through the chip (Figure 3.7a) while opening the cap of eppendorf tubes. In this way, cells could take both media and gases which interact with their surroundings, similar to how they grow in vivo condition (Figure 3.7b). For cell culture, the flow rate of 10 µl/hr was withdrawn the media from the eppendorf to the syringe in the incubator for three days.

In addition, we also examined three days of cell culture without flowing through the spiral part because according to the previous study, the results showed that spiral part could potentially cause cell to deform (~30% of total cells) and die during the sorting process. For this, the experiment of cell culture with and without passing through the spiral part allowed us to determine how much percentage of deformed and dead cells could recover themselves after three days of cell culture and how much percentage of cells loss occurred in the trapping part. We started introducing the sample through the device at the 4<sup>th</sup> and 5<sup>th</sup> outlets with the very low flow rate of 0.01 ml/min and blocked the fluid flow at the inlets. The cells slowly flowed through the chambers from the 4<sup>th</sup> and 5<sup>th</sup> outlets to the 1<sup>st</sup>, 2<sup>nd</sup> and 3<sup>rd</sup> outlets with the volume of 3 ml (Figure 3.8a). After that, switching and introducing the cells in the 1<sup>st</sup> and 2<sup>nd</sup> outlets at 0.01 ml/min with 3 ml passing through the 1<sup>st</sup> and 2<sup>nd</sup> outlets to the 3<sup>rd</sup>, 4<sup>th</sup> and 5<sup>th</sup> outlets (Figure 3.8b). Finally, trapped cells in wells were cultured in the device at the flow rate of 10 µl/hr for three days using withdrawn mode (Figure 3.7) and then the cells were taken out from the wells and checked cell viability afterward. Note that, the reason that we switched and introduced the cells from 4<sup>th</sup> and 5<sup>th</sup> to 1<sup>st</sup> and 2<sup>nd</sup> outlets because we needed cells to be trapped in all five chambers evenly. According to the study of triangular microwell, once cells move towards the wells, cells tend to be trapped at the apex but hypotenuse or adjacent of triangular microwells.

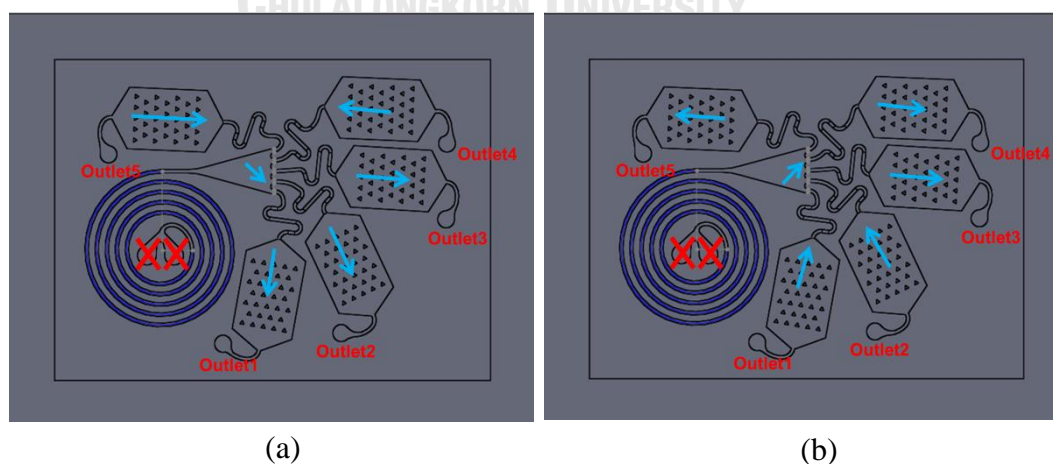


Figure 3.8 Introducing the cells without passing through the spiral part (a) flowing the cells with the volume of 3 ml at 5<sup>th</sup> and 4<sup>th</sup> outlets and (b) switching and introducing the cells with the another volume of 3 ml at 1<sup>st</sup> and 2<sup>nd</sup> outlets.

Note that, in order for trapping particles/cells in the proper chambers, all chambers were designed based on the equality of pressure drop in all chambers (calculation not shown). The pressure drop must be equal in all five chambers to receive the correct and precise data. We also tested the pressure drop in all chambers by collecting the volume of sample after flowing through the device for four sets as shown in Table 3.1.

Table 3.1 Volume of sample was collected at the five outlets for four sets

Chamber	1	2	3	4	5
set 1 (ml)	1.7	1.8	1.9	1.5	1.3
set 2 (ml)	2.1	1.5	1.9	1.8	1.0
set 3 (ml)	2.3	2.3	2.3	1.9	1.3
set 4 (ml)	2.1	2.3	2.2	1.9	1.3
Average	2.0±0.2	2.0±0.3	2.1±0.2	1.8±0.2	1.2±0.1

As you can see from the data, most chambers (1<sup>st</sup>-4<sup>th</sup> chamber) seem to have the pressure drop similarly. However, the 5<sup>th</sup> chamber may have more pressure drop than others. For this reason, the less volume of sample comes out at the 5<sup>th</sup> chamber. Note that, a small number of beads come out at the 5<sup>th</sup> chamber. It is reasonable to assume that the major contributor causing a high trapping distribution are chamber number 1<sup>st</sup> to 4<sup>th</sup> while the chamber number 5 can be ignored in this case.

Furthermore, machining with CNC process could cause the rough surface on PDMS. For this reason, surface roughness in the front of the equilateral triangular wells was also measured microscopically to ensure that fluid flow passing through in this area acting as laminar flow. Microscope with magnification of 50× was used to evaluate the different height of the area. It was found that the different height was about 15 μm in height as demonstrated in Figure 3.9. Regarding 15 μm height differences compared to the length of well of 600 μm, it might not affect the fluid flow.

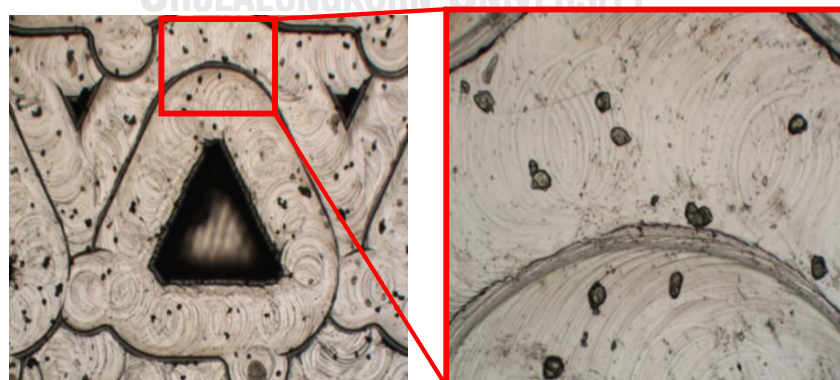


Figure 3.9 Surface roughness was caused by machining from CNC process on the side of equilateral triangular well.

### 3.3 Results

As we mentioned earlier, the experiments were divided into two parts. First part, microparticles were examined with the flow rate of 0.2, 0.5, 1 and 2 ml/min to obtain the optimum condition for trapping 10, 15 and 20  $\mu\text{m}$  microparticles. The number of particles—10, 15 and 20  $\mu\text{m}$  were counted in wells and calculated in terms of trapping distribution while the number of particles in wells added the number of particles on the surface around the wells and outlets were calculated in terms of the sorting efficacy. Second part, we picked up the flow rate with the maximal percentage of trapping distribution for fibroblasts (STO) and mast cell tumor cell line (LuMC) based on their sizes and then investigated cell viability before and after sample flowing through the device and after culturing cells for three days.

#### 3.4.1 The Results for Polystyrene Beads

Microparticles of 10, 15 and 20  $\mu\text{m}$  were examined (Figure 3.10) with three different flow rates of 0.2, 0.5, 1 and 2 ml/min and counted the number of trapped particles in wells and then calculated them in terms of the percentage of trapping distribution. For full information for cell enumeration protocols of trapping distribution, see Appendix B4. The results showed that at 0.2 ml/min, most of 10 and 15  $\mu\text{m}$  microparticles tended to be trapped in the 4<sup>th</sup> chamber ( $43.25\% \pm 6.03\%$  and  $50.62\% \pm 6.72\%$ ). However, some of those particles were trapped in the rest of the chambers as demonstrated in Figure 3.11a. Furthermore, at 0.2 ml/min, the majority of 20  $\mu\text{m}$  beads were trapped in the 2<sup>nd</sup>, 3<sup>rd</sup> and 4<sup>th</sup> chambers. This suggested that flow rate of 0.2 ml/min provided the maximal percentage of trapping distribution for the particles of 10 and 15  $\mu\text{m}$ .

At 0.5 ml/min, most particles of all sizes were trapped in the 3<sup>rd</sup> chamber ( $76.78\% \pm 12.50\%$ ,  $83.70\% \pm 7.32$  and  $51.37\% \pm 5.24\%$ ) as shown in Figure 3.11b. At this flow rate, the data showed the maximal percentage of trapping distribution as well as the highest number of particles that were trapped in 3<sup>rd</sup> chamber for all three different sizes of particles. This suggested that if the size of cells were about 15  $\mu\text{m}$ , there was a great possibility to trap the majority of cells at this flow rate.

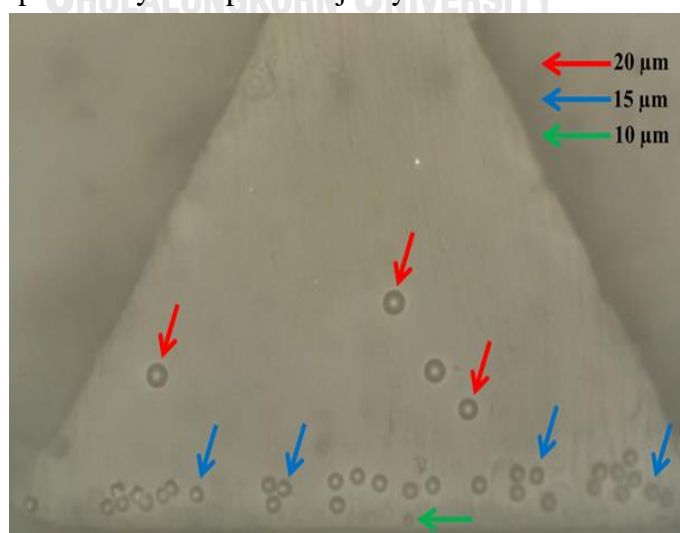
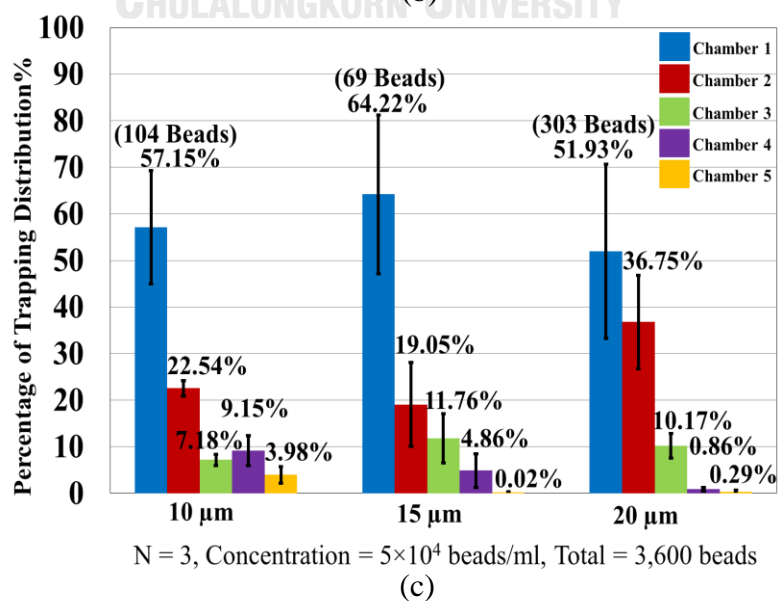
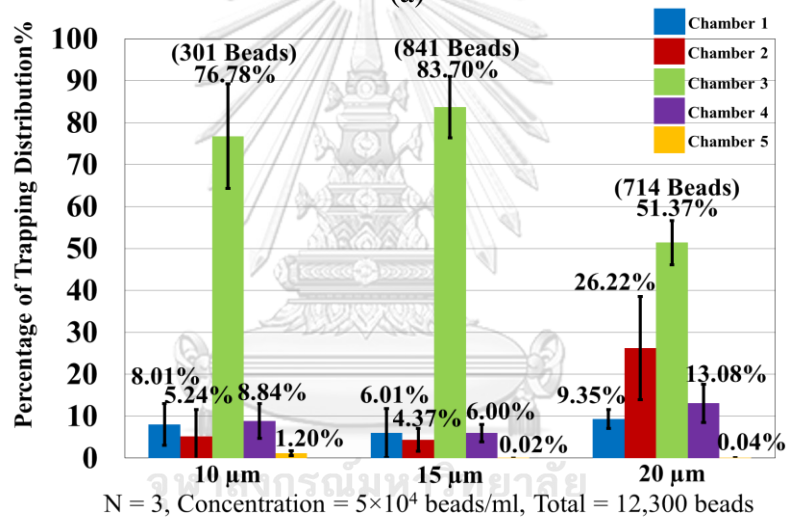
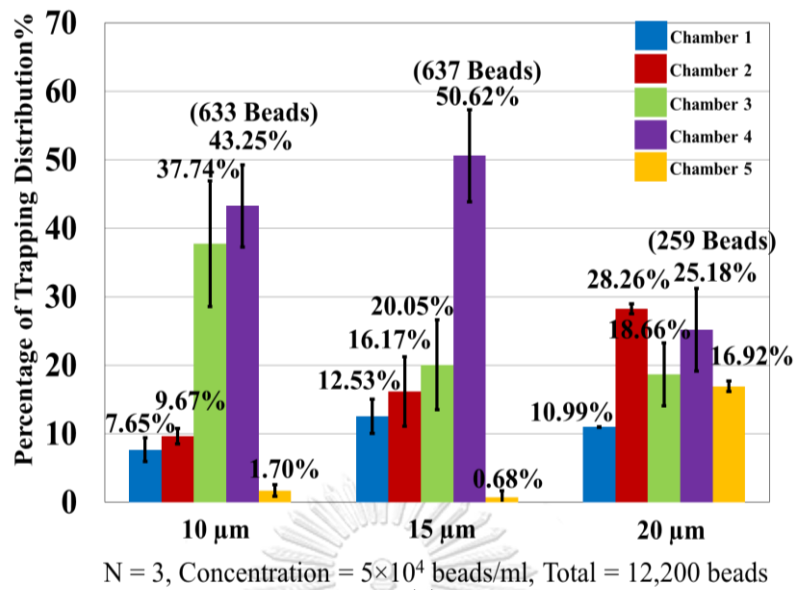


Figure 3.10 Observation of particles of 10, 15 and 20  $\mu\text{m}$  under a light microscope





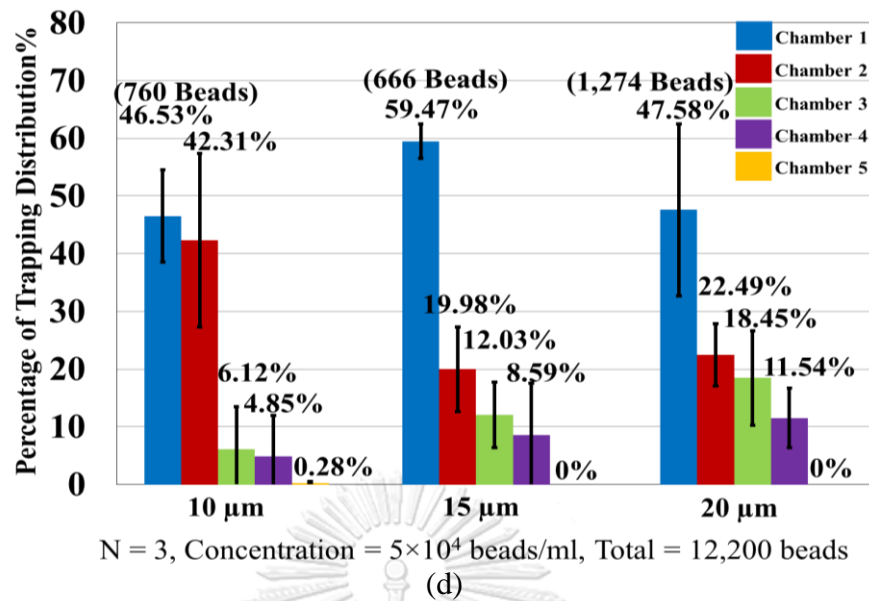


Figure 3.11 Percentage of trapping distribution in chambers at (a) 0.2, (b) 0.5 (c) 1 and (d) 2 ml/min.

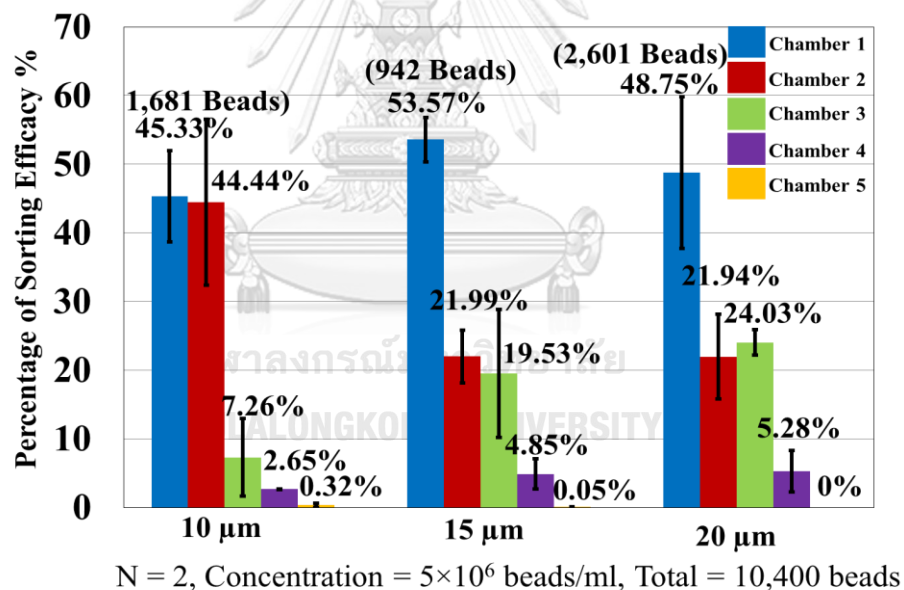


Figure 3.12 Percentage of sorting efficacy (counting particles—wells, surface and outlets) in chambers at 2 ml/min

At 1 ml/min, most particles of 10, 15 and 20  $\mu\text{m}$  were trapped in chamber number 1<sup>st</sup> ( $57.15\% \pm 12.16\%$ ,  $64.22\% \pm 17.04$  and  $51.93\% \pm 18.72\%$ ) and the minority of particles were captured in the 2<sup>nd</sup>, 3<sup>rd</sup>, 4<sup>th</sup> and 5<sup>th</sup> chamber, respectively. This suggested that at this flow rate, it provided the maximal percentage of trapping distribution for all sizes of particles in the 1<sup>st</sup> chamber as shown in Figure 3.11c.

Finally, at 2 ml/min, the data demonstrated that most particles of 10, 15 and 20  $\mu\text{m}$  were still trapped in the 1<sup>st</sup> chamber which were similar to the results of flow rate of 1 ml/min ( $46.53\% \pm 7.96\%$ ,  $59.47\% \pm 2.98\%$  and  $47.58\% \pm 14.92\%$ ). However, the

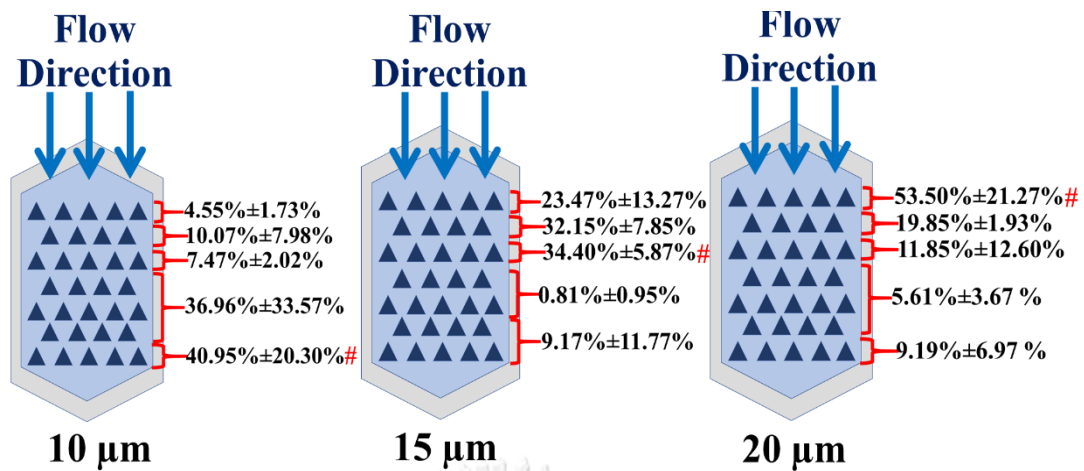
number of 10  $\mu\text{m}$  particles dramatically increased in the 2<sup>nd</sup> chamber at  $42.31\% \pm 15.01\%$  as shown in Figure 3.11d. Note that, the majority of particles flowed over the wells while a small number of particles were trapped in the wells. It may lead to incorrect results. Therefore, it was decided to increase the concentration of particles from  $5 \times 10^4$  to  $5 \times 10^6$ .

As can be seen from the above results, the flow rate of 0.5 ml/min provided the maximal percentage of the trapping distribution for 15  $\mu\text{m}$  particles about 80% in the 3<sup>rd</sup> chamber. Regarding this reason, this flow rate was used in the cell experiments since the size of STO and LuMC cells was about 15  $\mu\text{m}$ .

Beside the trapping distribution in each chamber, we also evaluated the percentage of sorting efficacy by counting the number of particles in the wells, the number of particles on surface around the wells and number of particles at the outlets at 2 ml/min (Figure 3.12). For full information for cell enumeration protocols of sorting efficacy, see Appendix B5. The sorting efficacy was examined only one condition of 2 ml/min. The results of sorting efficacy showed the similar results of trapping distribution at the flow rate of 2 ml/min because the majority of the particles were trapped in wells while the some of those particles were on the surface around wells and outlets. Therefore, it was reasonable to assume that the percentage of trapping distribution could indicate the percentage of sorting efficacy as well. According to this assumption, it implied that the particles of 10, 15 and 20  $\mu\text{m}$  particles started to gradually moved towards the inner wall of the outlet channel, and comes in the 4<sup>th</sup>, 3<sup>rd</sup>, 2<sup>nd</sup> and 1<sup>st</sup> chamber as the flow rate increases (0.2, 0.5, 1 ml/min). Further increasing flow rate at 2 ml/min, the 10  $\mu\text{m}$  particles moved separately from the 15 and 20  $\mu\text{m}$  particles in the 2<sup>nd</sup> chamber.

In addition, we investigated how many particles could be trapped in each row of the microwells in the 3<sup>rd</sup> chamber at flow rate of 0.5 ml/min. We selected this flow rate in the 3<sup>rd</sup> chamber because it provided the maximal percentage of trapping distribution for 15  $\mu\text{m}$  particles. In this experiment, we will be able to understand that how the weight of particles could affect the trapping distribution in each row of chamber. We counted the number of particles in well in each row with three sets and the experiment was performed with three times and then calculated in terms of the percentage of particle/cell trapping.

According to the results, it was discovered that in the 3<sup>rd</sup> chamber at 0.5 ml/min, most particles of 10  $\mu\text{m}$  flowed over the wells and then were trapped in the 7<sup>th</sup> row ( $40.95\% \pm 20.30\%$ ) by trajectory of projectile. For the particles of 15  $\mu\text{m}$ , the particles tended to be trapped around the 2<sup>nd</sup> and 3<sup>rd</sup> row ( $32.15\% \pm 7.85\%$  and  $34.40\% \pm 5.87\%$ ) while the particles of 20  $\mu\text{m}$  were trapped in the 1<sup>st</sup> row ( $53.50\% \pm 21.27\%$ ). As a result, the large particles which had more weight would be trapped in the front row while small particles which had less weight would flow over the front row and then trapped in the back rows of chamber (Figure 3.13).



N = 3, Concentration =  $5 \times 10^4$  cells/ml, Total = 5,500 beads

Figure 3.13 Percentage of particle trapping in each row of the 3<sup>rd</sup> chamber at 0.5 ml/min.

Furthermore, we observed the trapped particles in an individual well. It was found that the large particles were trapped in the front while the medium and small ones were trapped in the middle and back well by the trajectory of projectile. This suggested that the particles of 20  $\mu\text{m}$  that had more weight would be trapped in the front while the particles of 10 and 15  $\mu\text{m}$  went over the front and trapped in the back well as demonstrated in Figure 3.14.

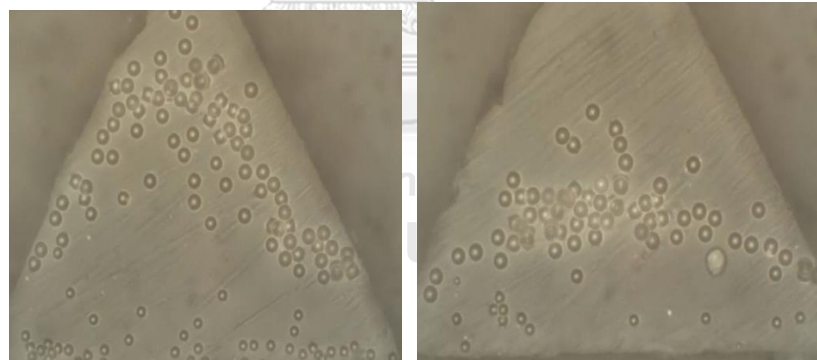


Figure 3.14 Example of mixtures of particle of 10  $\mu\text{m}$ , 15  $\mu\text{m}$  and 20  $\mu\text{m}$  were trapped in wells—the largest size of beads were trapped in the front and the smaller size were trapped in the back well.

As can be seen from the above data, apart from the weight of mass affecting the trajectory of projectile, drag force also plays an important role in the trajectory of projectile as well. Drag force is force acting opposite to the relative motion of particles/cells moving to a surrounding fluid. Therefore, drag force may be one of the factors resulting in trapping more particles in the front chamber/well Figure 3.15a.

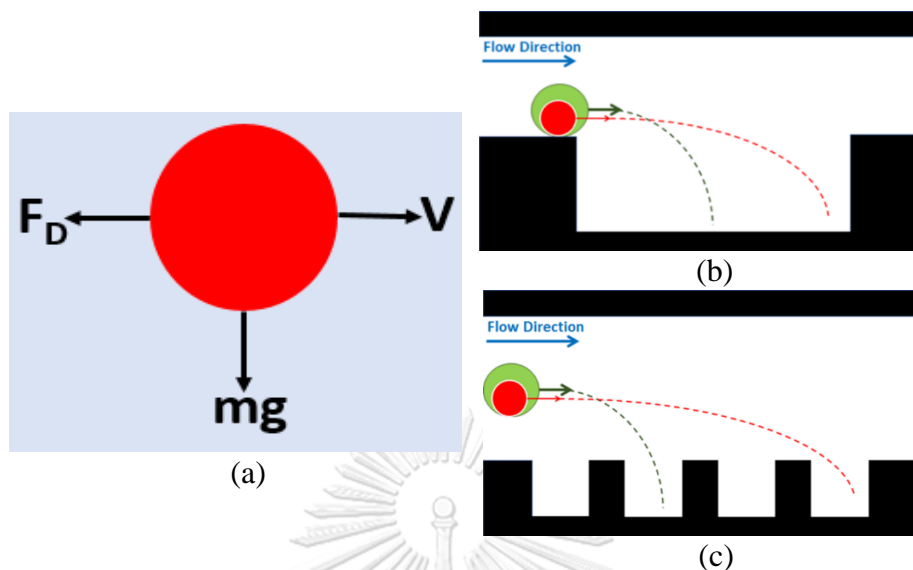


Figure 3.15 Schematic picture of (a) free body diagram of a particle moving to a surrounding fluid (b) trajectory of projectile in a well and (c) trajectory of projectile in a chamber

In order to find the relation of drag force and the trapping distribution, it is really needed to find the ratio of drag force and weight of mass. In this way, we will be able to understand how much drag force affecting the trapping distribution. For this, Drag force and weight of mass are given by

$$\frac{F_D}{mg} = \frac{0.5\rho V^2 C_D A}{\rho \forall g} \quad (3.2)$$

where  $F_D$  is drag force acting opposite direction of particle or cell motion,  $m$  is mass of particle/cell,  $g$  is the gravitational field strength,  $\rho$  is the water viscosity,  $C_D$  is the drag coefficient sphere,  $V$  is the velocity,  $A$  is the spherical area ( $\pi r^2$ ),  $r$  is the radius of the spherical particle,  $\forall$  is the spherical volume ( $\frac{4}{3}\pi r^3$ ) and then simplify formula by

$$\frac{F_D}{mg} = \frac{0.5V^2 C_D}{\frac{4}{3}rg} \propto \frac{V}{r} \quad (3.3)$$

The ratio of drag force and weight of mass is shown in formula 3.3. According to the ratio, drag force is relied on velocity of flowing fluid but the weight of mass is relied on the reciprocal of particle's radius. Therefore, drag force and the size of particles/cells have an effect on the trapping distribution in the individual well and the rows of chamber (Figure 3.15b-c).

#### 3.4.2 The Results for Fibroblast (STO Mouse Fibroblast Cells)

In this work, fibroblast (STO mouse fibroblast cells, ACTT) was acquired within one day of collection from Biotechnology Laboratory, Veterinary Science, Chulalongkorn University. We started with the evaluation of the size of STO cells on

a hemocytometer with microscopy measurement program as demonstrated in Figure 3.16. The size of STO cells were measured about 15-20  $\mu\text{m}$  in diameter. In this part, STO cells were examined with the flow rate of 0.5 ml/min since the size of STO cells is about 15  $\mu\text{m}$  with concentration of  $1 \times 10^4$  cells/ml.

The experiment of the investigation of trapping cells was examined by injecting STO cells through the device at 0.5 ml/min (Figure 3.6). After that, collected cells in microtubes at the outlets and checked cell viability. Later, the investigation of cell culture was also examined by withdrawing the media in the microtubes and flowing through the chambers at 10  $\mu\text{l/hr}$  for three days (Figure 3.7). In this way, STO cells could receive nutrients from the media and carbon dioxide from the incubator as cell culture in an opened system. To check cell viability after culturing for three days, the PDMS chip and glass slide were torn apart and then the trapped cells were withdrawn from the well using a 20  $\mu\text{l}$  pipette and then checked cell viability. Finally, we also tested cell culture after three days without flowing through the spiral part (Figure 3.8). According to this test, we will be able to investigate how many cells could recover themselves and check how many cells could be viable in the trapping part after culturing for three days.

It should be noted that it is really necessary to eradicate bubbles in the microfluidic system by introducing the media through the system first and then carefully connected tubes to inlets and outlets in the PDMS chip without bubbles going backward to the system. To control the quality of cell viability, it will not be used in our experiment if the wells are filled with air or bubbles because it may affect cell viability. The test of cell viability was examined with three sets and the total of STO cells were about 2,100 cells.

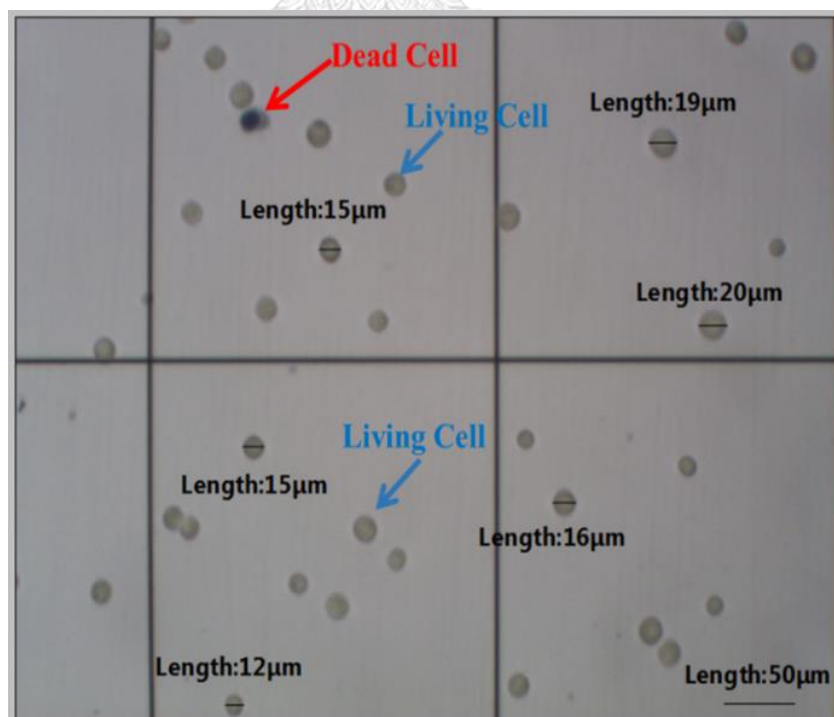
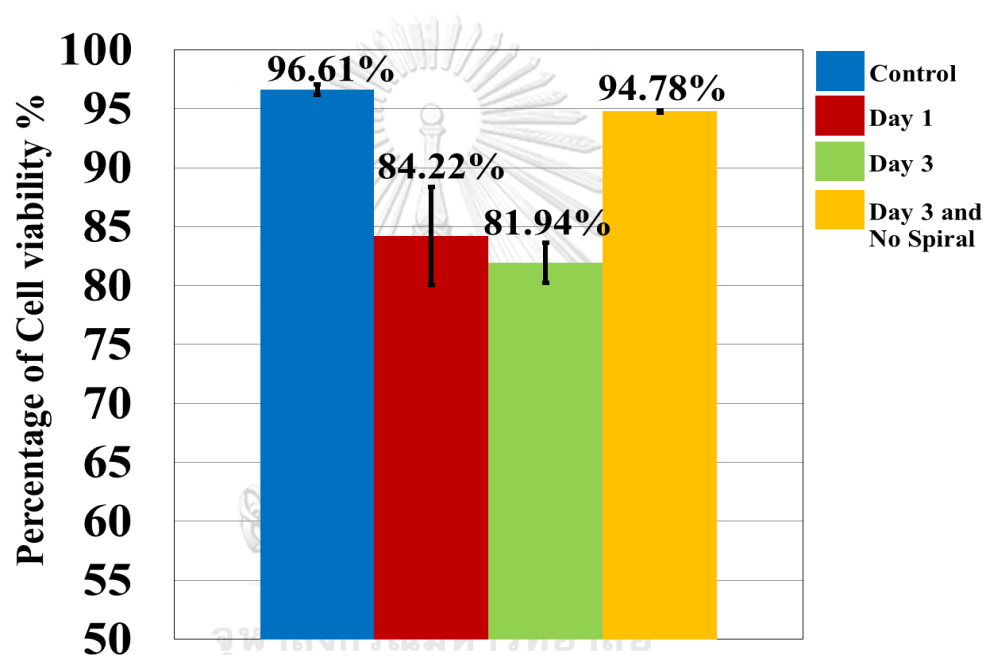


Figure 3.16 Measurement of fibroblast sizes on a hemocytometer with a microscopy program

The results of STO viability showed that control sample was measured about  $96.61\% \pm 0.45\%$  and then cell viability decreased to  $84.22\% \pm 4.18\%$  which were about 12.4% after flowing through the device and further decreases to  $81.94\% \pm 1.69\%$  after culturing for three days. According to the previous work of spiral experiment, at 2 and 10 ml/min spiral microchannel caused cells to die about 7-10%. This data reasonably implied that there were possibilities for cells to die in the sorting part in the integrated microfluidic device. Furthermore, the comparison of two cases—with and without passing through a spiral part implied that the dead cells were not recovered themselves back to viable cells after culturing cells for three days. In addition, there was no significant of cell loss after culturing three days without passing through the spiral and the controls as demonstrated in Figure 3.17. This indicated that trapping part barely affected cell viability after culturing for three days.



N = 3, Concentration =  $1 \times 10^4$  cells/ml, Total = 2,100 cells

Figure 3.17 Percentage of STO viability—Control (blue), Day1 (red), Day3 (green) and Day3 without passing through the spiral part (yellow).

The next experiment, we examined the trapping distribution by counting the number of STO cells in wells and calculating in terms of the percentage of the trapping distribution. In this experiment, the sizes of STO cells were categorized into three ranges— $<15 \mu\text{m}$ ,  $15\text{-}25 \mu\text{m}$ , and  $>25 \mu\text{m}$ . Furthermore, we also calculated how many STO cells were trapped in wells in each row of the chambers.

The results of trapping distribution showed that at 0.5 ml/min, most STO cells were trapped in the 3<sup>rd</sup> chamber with  $38.21\% \pm 8.17\%$ ,  $43.57\% \pm 8.13\%$  and  $35.48\% \pm 8.81\%$  for  $<15 \mu\text{m}$ ,  $15\text{-}25 \mu\text{m}$ , and  $>25 \mu\text{m}$ , respectively which was similar to the experiment of microparticles. This result indicated that the 3<sup>rd</sup> chamber provided the maximal percentage of trapping distribution for STO cells as shown in Figure 3.18.

According to the results of trapped cells in each row, the data demonstrated that  $<15\ \mu\text{m}$  STO cells were trapped in the back chamber (the 7<sup>th</sup> row) of  $34.56\% \pm 15.04\%$  while  $15\text{-}25\ \mu\text{m}$  STO cells were trapped in the 3<sup>rd</sup> row of  $29.31\% \pm 2.04\%$  and  $>25\ \mu\text{m}$  STO were trapped in the 2<sup>nd</sup> row of  $27.70\% \pm 19.94\%$ . This data suggested that the large cells tended to be trapped in the front row while the small cells were trapped in the back row of the chamber. This result agreed with the experiment of microparticles (Figure 3.19).

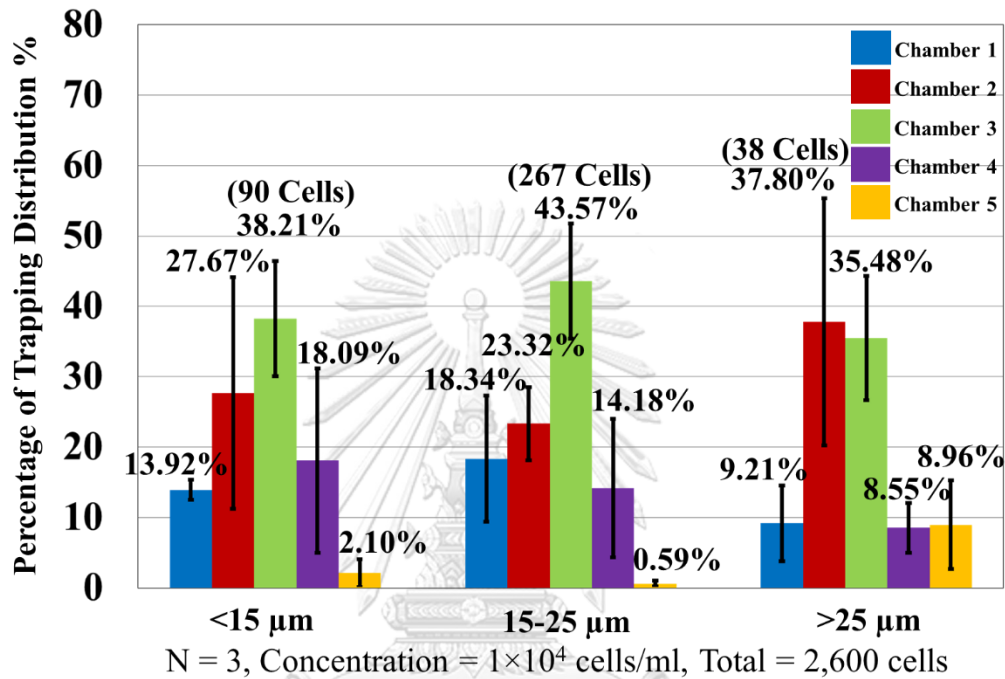


Figure 3.18 Percentage of ST0 trapping distribution in all chambers at 0.5 ml/min

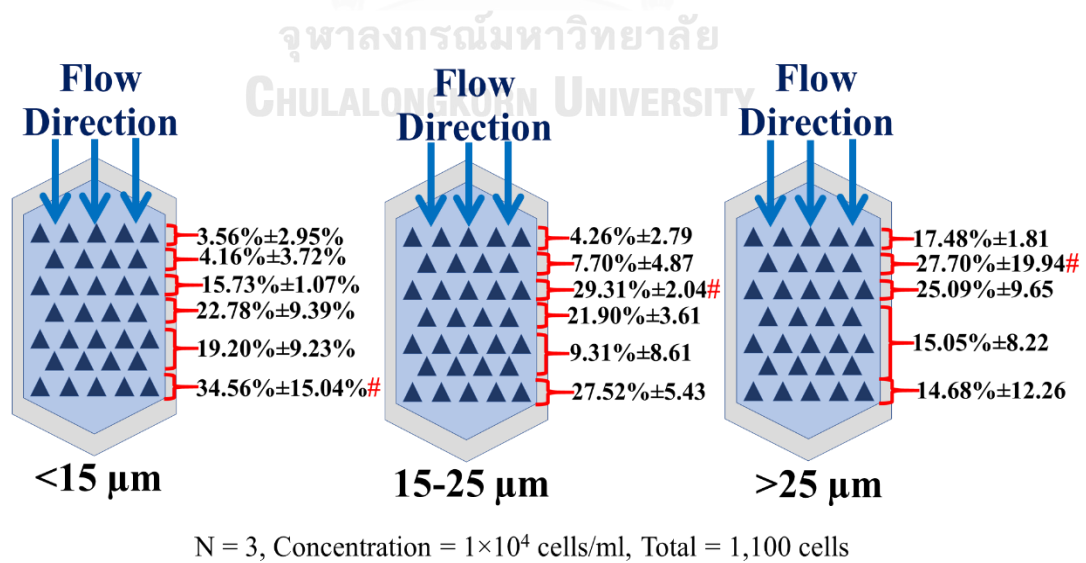


Figure 3.19 Percentage of cell trapping in the rows of the 3<sup>rd</sup> chamber at 0.5 ml/min.

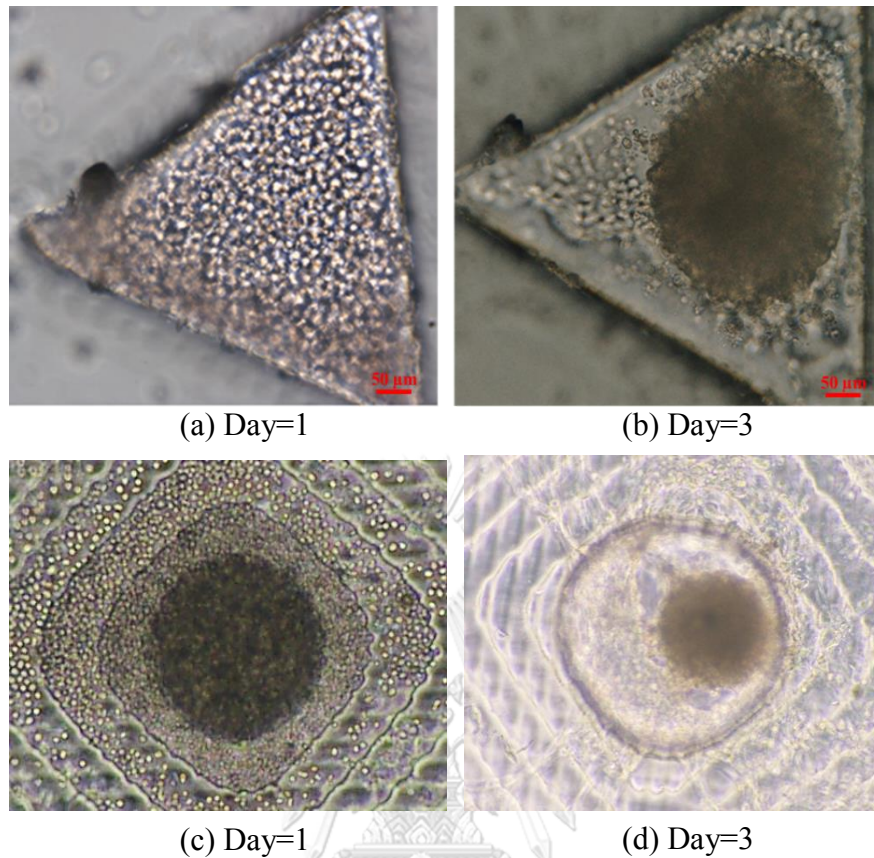


Figure 3.20 Spheroid formation of STO in well (a) Day1, (b) Day3 in equilateral triangular microwell and (c) Day1 and (d) Day3 in the diamond pyramidal microwell [Thanapat Chunfong]

The images of STO cells were taken under a light microscope in the first day and third day of cell culture. After three days of culture with flowing through the media at  $10 \mu\text{l/hr}$ , STO cells were formed as a spheroid similar to the study of T. Chunfong [131] that showed the formation of fibroblast (spheroid) in the diamond pyramidal microwell (Figure 3.20). This indicated that the integrated microfluidic device provided the high percentage of cell viability with 84% and had a good environment that allowed fibroblast cells to form themselves as a spheroid with 82% viability after culturing for three days.

Beside the trajectory of projectile and drag force affecting the trapping distribution, vortices in each row and structures of well in a chamber had the significant influence on the trapping distribution as well. According to the video recorder, the vortices in the 1<sup>st</sup> row of a chamber helped cells move slowly leading to a large number of cells were trapped in the 3<sup>rd</sup> row. After that, some of those captured cells in the 3<sup>rd</sup> row were escaped on the side well by vortices resulting in the small number of cells were trapped in 5<sup>th</sup> row. Finally, most cells were directed by the geometry of chamber at the outlets leading to the majority of cells were trapped in the 7<sup>th</sup> row of the chamber (Figure 3.21).



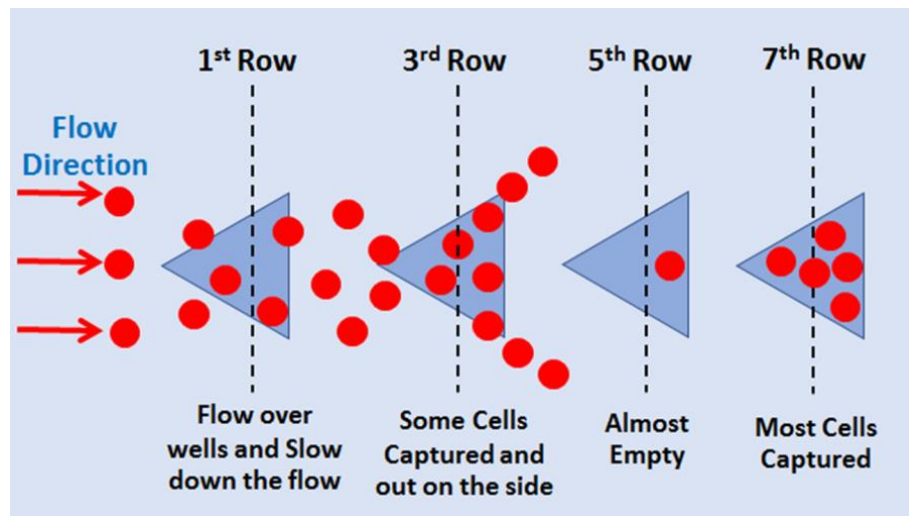


Figure 3.21 Influence of vortices in each row affecting the trapping distribution

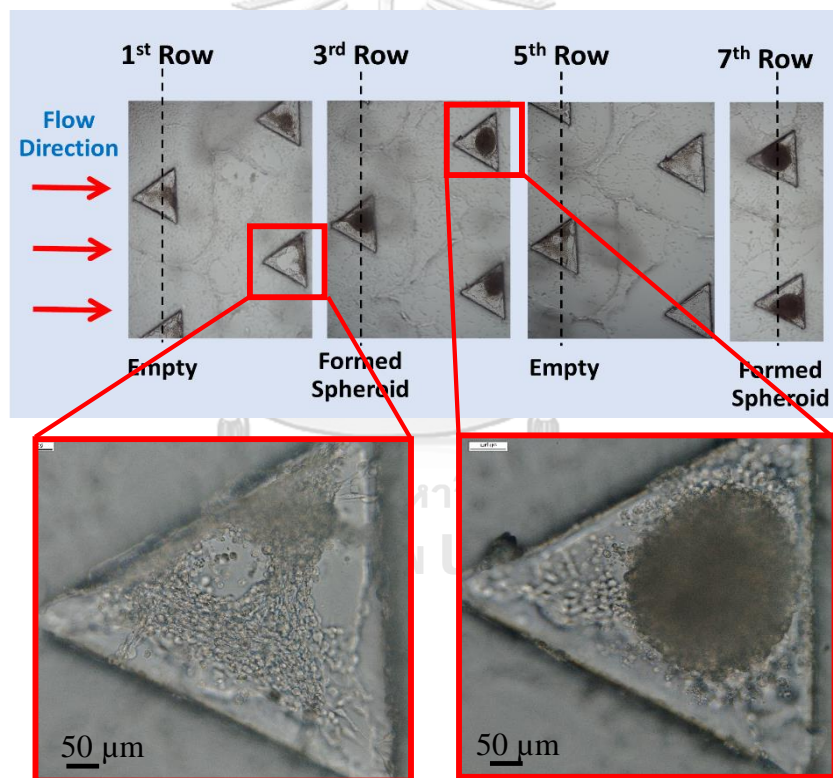


Figure 3.22 Influence of vortices in each row affecting STO formation

In addition, due to the cell formation in the wells, the number of cells in wells could potentially affect the cell formation after three days of cell culture. Figure 3.22 demonstrated the formation of STO cells in each row. As can be seen in the figure, it implied that after three days, the half full or empty well's bottom of STO cells barely formed themselves as a spheroid resulting the fragmental or incomplete formation of spheroids in the 1<sup>st</sup>, 2<sup>nd</sup>, 5<sup>th</sup> and 6<sup>th</sup> row where the small number of STO cells were trapped in those wells while the 3<sup>rd</sup>, 4<sup>th</sup> and 7<sup>th</sup> row, the microwell with full of STO

cells tended to form themselves as spheroids after three days of cell culture. This suggested that the number of cells trapped in wells influenced by trajectory of projectile and vortices had a huge effect on fibroblast formation.

### 3.4.3 The Results for Mast Cell Tumor Cell Line (LuMC)

In this work, mast cell tumor cell line (LuMC) was acquired from Laboratory of Veterinary Surgery, University of Tokyo, Takayuki Nakagawa. This experiment started with measuring the size of LuMC. The size is about 10-20  $\mu\text{m}$  in diameter (Figure 3.23) and then LuMC viability was tested with Trypan Blue before (Control) and after examining (Day1) and after culturing for three days (Day3). All experiments were examined and then calculated in terms of the percentage of cell viability as well as taking images of LuMC in the first and third day in comparison.

The results showed that the percentage of cell viability was  $84.66\% \pm 3.68\%$  for control sample. After introducing the sample in the device, cell viability slightly decreased to  $74.32\% \pm 2.72\%$  (Figure 3.24) which is similar to the experiment of STO cells. This suggested that the integrated microfluidic device could potentially cause about 10% of cell loss. Therefore, 10% of cell loss in our system is quite reasonable and the results agreed with the previous research.

After three days of culturing LuMC cells in an incubator, the results of cell viability indicated that cell viability was slightly decreased from  $74.32\% \pm 2.72\%$  to  $68.31\% \pm 1.98\%$ . This result implied that culturing cells for three days with flowing media continuously at 10  $\mu\text{l/hr}$ , most of LuMC cells were still alive in a chip of about 68.31%. To ease of understanding, Figure 3.24 showed the results of cell viability decreased before examining, after examining and after culturing for three days. Moreover, the experiment of cell culture for three days without passing through the spiral part also showed the similar results of STO cell experiment. Therefore, dead cells of LuMC were not recovered themselves after three days of cell culture and trapping part hardly caused cell loss which agreed with the experiment of STO cells.

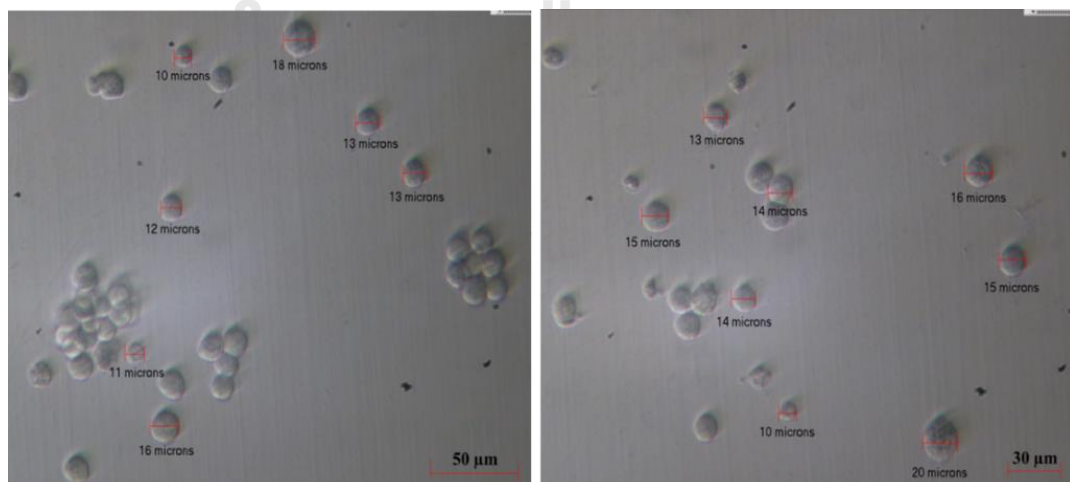
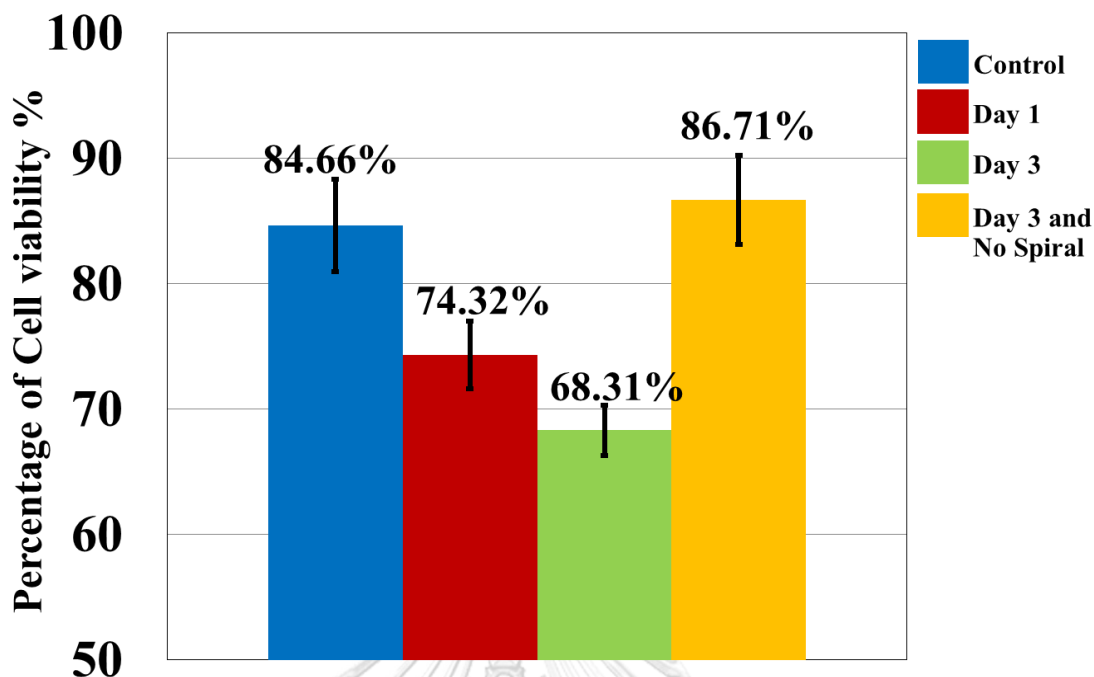


Figure 3.23 Sizes of LuMC cells are measured under a light microscope



N = 3, Concentration =  $5 \times 10^6$  cells/ml, Total = 2,500 cells

Figure 3.24 Percentage of LuMC viability—Control (blue), Day1 (red), Day3 (green) and Day3 without passing through the spiral part (yellow).

In addition, the images of LuMC were taken in the same well under a microscope in the first day and third day of cell culture. Flowing through the media at  $10 \mu\text{l/hr}$  for three days, there was nothing changes to LuMC cells (Figure 3.25a-b). This indicated that our device still provided a high percentage of cell viability after the sample flowing through the device which agreed with the experiment of STO cells. However, it may not be suitable for culturing LuMC cells as a good environment for cell culture. It is noted that, LuMCs are able to be formed themselves as clusters after culturing several days in a suitable environment but not form in the well of our device. This suggested that the microfluidic device was not a suitable environment for culturing LuMC but cells could be potentially viable in this environment.

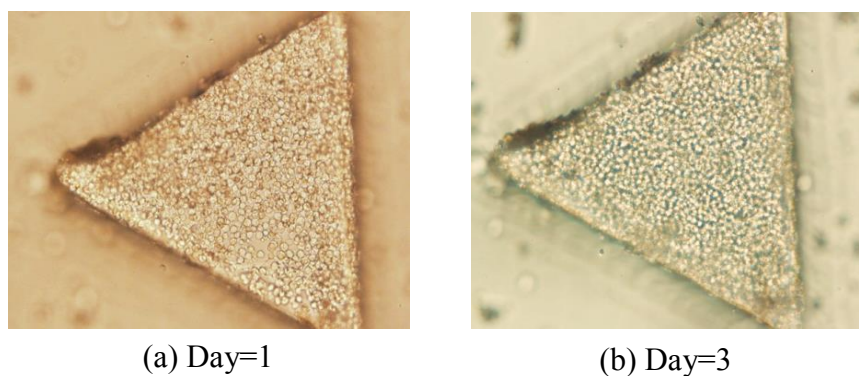


Figure 3.25 Mast cell tumor cells (LuMC) (a) Day1 and (b) Day3 and mouse fibroblasts (STO)

#### 3.4.4 The Summary of Integrated Microfluidic Device

To sum up, the integrated microfluidic device can trap the microparticle of 10  $\mu\text{m}$ , 15  $\mu\text{m}$  and 20  $\mu\text{m}$  potentially. At the flow rate of 0.5 ml/min, it provides the maximal percentage of trapping distribution for particles of 15  $\mu\text{m}$ . For this, the flow rate of was 0.5 ml/min is used in cell experiment since the size of fibroblasts and MCTs are about 15  $\mu\text{m}$ . Furthermore, according to the assumption of sorting efficacy and trapping distribution, cells tended to move towards the inner wall and came in the 4<sup>th</sup>, 3<sup>rd</sup>, 2<sup>nd</sup>, and 1<sup>st</sup> chamber, respectively and then started sorting the particles of 10  $\mu\text{m}$  from the 15 and 20  $\mu\text{m}$  at 2 ml/min.

Cell viability of STO and LuMC after flowing through the integrated microfluidic device decreases about 10-12%. The results agree with the previous experiment (result of spiral microchannel). Furthermore, the percentage of cell viability of STO and LuMC further slightly decreases after culturing for three days. However, in the case of three days of cell culture in STO and LuMC experiment, the data demonstrates that dead cells after flowing through the spiral part were not recovered back as viable cells and there is very few of cell loss in the trapping part that is not significant differences between the control sample and the cultured cells for three days without passing through the spiral part. Surprisingly, after culturing for three days, the STOs tend to form themselves as a spheroid but LuMC cells do not form as a cluster. This indicates that our integrated microfluidic chip possibly maintain cells with the high percentage of cell viability and contribute cells to form themselves in a certain kind of cells.

## Chapter 4

### Conclusions and Discussion

#### 4.1 Conclusion for Feeding System, Spiral Microchannel and CEA

The experiment of this phase, it is divided into three parts. First part is the experiment of feeding system with different flow rates of 0.3, 1, 5 and 8 ml/min. Second part, the setup of spiral microchannel is tested with the flow rate of 2 and 10 ml/min. In the final part, the setup of CEA is examined with the optimum flow rate of 0.3 ml/min in the main channel and 0.24 ml/min in the secondary channel. The experiments of all parts were compared in terms of the percentage of cell viability, cell morphology and intracellular structure.

According to data of feeding system, the data of cell loss is not found in all cases of the feeding system condition because exposure time is so short at 0.3, 1, 5 and 8 ml/min. Moreover, cell deformation and intracellular damage such as the leak of membrane, stretched cytoplasm, and nucleus break down are slightly found in all cases as well. This is confirmed by the investigation of SEM and Wright-Giemsa stain after passing through the syringe at 0.3, 1, 5 and 8 ml/min.

As for the spiral microchannel, the data demonstrates that there is no significantly different in cell loss using the flow rates of 2 and 10 ml/min. However, these two flow rates exerted total extensional and shear stress in a different order and pattern of cell's movement and exposure time due to increasing flow rates. As for SEM, no significantly different between the number of normal cells is found. However, ~30% of cell deformation significantly increases compared to ~4% in the feeding system and ~12% in CEA. This suggests that shear stress dominates over extensional stress in the spiral microchannel covering the entire length of the channel close to the walls with long exposure time that could cause cells to be sheared along the distance of five-loop spiral resulting in a significant number of cell deformation and death. As for the experiment of Wright-Giemsa stain, it is found that ~2 and ~9% of normal cells are decreased at flow rates of 2 and 10 ml/min. This confirms that stresses in the spiral microchannel also affect intracellular structures, and the stronger effects could be found at higher flow rates.

On the other hand, the data of CEA shows that the majority of cell loss is found in this part. As for SEM and Wright-Giemsa stain, the percentage of normal cells similarly decreases. Furthermore, the data indicate that extensional stress dominates in the CEA and occur at the abrupt change in cross section where the cross-section of the flow channel changes. The extensional stress with high magnitude at the corner area covering almost entire the cross-section of the flow channel. As a result, the majority of cells that travel in the larger high-stress area in CEA has a high potential to be damaged in this area. This could cause more cell damage and loss in CEA than the feeding system.

It should be noted that one of the biggest challenges in increasing the sorting efficacy is to increase flow rate while maintaining cell viability and preventing the cells from stresses. Once the flow rate increases, the efficacy of sorting would get better. However, exposure time that cells expose to stress would be short but the cells

could be damaged in terms of intracellular damage by a high stresses. In contrary, once the flow rate decreases, exposure time would be longer resulting in the damage to cells in terms of cell deformation. This is the tradeoff between flow rate, exposure time and type of cell damage—intracellular damage and cell deformation. It is significantly important to choose a sorting technique considering the type of cell damage, cell viability and applications.

#### **4.2 Conclusion for Integrated Microfluidic Device**

In this phase, the investigation is divided into three parts. First part, three different sizes of microparticles are investigated in terms of trapping distribution at 0.2, 0.5, 1 and 2 ml/min and sorting efficacy at 2 ml/min. The flow rate of 0.5 ml/min providing the maximal percentage of trapping distribution in the prior part will be selected to use for cell experiment (STO and LuMC). Secondly, fibroblasts (STOs) are examined with the flow rate of 0.5 ml/min regarding the size of STO about 15  $\mu\text{m}$  and then investigate cell viability after flowing through the device and culturing at 10  $\mu\text{l/hr}$  for three days. Finally, mast cell tumor (LuMC) is also tested with the same flow rate at 0.5 ml/min and then investigates cell viability in the wells after flowing through and culturing cells at 10  $\mu\text{l/hr}$  for three days in the device as well.

As for the integrated microfluidic experiment with microparticles, it is found that when the flow rate increases in the range of 0.2, 0.5, 1 and 2 ml/min, the 10, 15 and 20  $\mu\text{m}$  microparticles gradually move towards the inner wall of the outlet channel, and comes in the 4<sup>th</sup>, 3<sup>rd</sup>, 2<sup>nd</sup> and 1<sup>st</sup> chamber of microwells, respectively and then the particles of 10  $\mu\text{m}$  starts separating from other sizes of particles at the flow rate of 2 ml/min. Furthermore, the flow rate of 0.5 ml/min provides the maximal percentage of trapping distribution for 15  $\mu\text{m}$  of 80% in the 3<sup>rd</sup> chamber.

As for the integrated microfluidic experiment with STO cells, it is found that the size of STO cells is about 15 to 25  $\mu\text{m}$ . Regarding this reason, flow rate of 0.5 ml/min is used in the experiment since the size of STO cells is about 15  $\mu\text{m}$ . The results show that the integrated microfluidic device can provide the high percentage of trapping distribution of 43.57% with a high percentage of viability after flowing through the device. After culturing for three days, dead cells are not recovered back themselves to viable cells and there is a few of cell loss in the trapping part during cell culture. Furthermore, the number of STO cells are counted in each row of the chamber. The results demonstrate that the larger sizes of STO cells are captured at the front row while the small sizes are captured in the back row. These results agree with the experiment of microparticles that weight of particle/cells and drag force have the effect on cell trapping distribution. However, the percentage of cell trapping slightly decrease compared to the percentage of particle trapping. This happen probably because the weight of cells is lighter than microparticles.

As for the integrated microfluidic experiment with LuMC, it is also performed to investigate cell viability after flowing through the device and after culturing for three days. Similar to the experiment of STO cells, the flow rate of 0.5 ml/min is also used in this experiment since the size of LuMC is about 15  $\mu\text{m}$  as well. According to the data, cell viability decreases about 10% after flowing through the device. Similar to the experiment of STO cells, dead cells are not recovered back to viable cells after sorting and a few of cell loss occurs in the trapping part after culturing for three days.

As for the formation of LuMC cells, the cells are not changed in cell morphology or formation as they should be. This happens because the microfluidic device may not be suitable for culturing LuMC cells but they can survive in this environment.

### 4.3 Discussion

To increase the sorting efficacy of an integrated microfluidic device, it is really needed to increase Dean drag force by increasing the flow rate. Increasing Dean drag force, streamlines are separated widely as well as help forming and focusing particles/cells as a streamline more quickly. However, the device could not withstand a high pressure as flow rate increases. As a result, the integrated microfluidic device could be broken down and ruined at the area of pressure aggregation.

To reduce the length of spiral microchannel is also another option to increase the sorting efficacy by maintaining Dean drag force during sorting process. Once, spiral microchannel increases in radius of curvature, Dean drag force becomes decreasing because Dean drag force is a function of radius of curvature. Therefore, the length of spiral microchannel should not be too long to lose the sustainability of Dean drag force. However, if the length of spiral microchannel is not long enough, focusing streamlines will not be able to separate effectively because it requires a suitable length to form themselves and reach to the equilibrium position.

The number of outlet channels could potentially help particles separate more effectively as the increase of outlet number. According to the previous study of spiral microchannel, it could separate three different sizes of microparticles successfully at 2 ml/min (optimum condition) with 10 outlets. The length between one channel to another is 300  $\mu\text{m}$ . In contrast, due to the data of sorting efficacy, the integrated microfluidic device was not achieved with the separation of three different sizes of microparticles at the same flow rate with 5 outlets of the length between channel to channel about 1,500  $\mu\text{m}$ . If the length of channel to channel is too long, it may cause the overlapping of streamlines resulting in unsuccessful focusing and separation. However, this issue is still unclear and needed to be further investigated.

The weight of a particle causes the sediment of particles in a syringe leading to the misleading of trapping distribution and sorting efficacy's results. According to the experiment, the number of large particles (20  $\mu\text{m}$ ) that have more weight would come out at the outlet and be trapped in wells less than the number of other sizes of particles causing the misleading of the result's interpretation and a high deviation. On the other hand, cellular samples—STO and LuMC cells are less weight. Therefore, the number of cell samples would flow along the main stream and be trapped in wells more than microparticles. To address the issue of particle sediment, withdrawn mode of syringe pump could be a good option by clamping the sample's tube on the stand and withdraw the sample from outlets to inlets instead. However, our microfluidic chip is designed with five outlet channels. It is really needed to use a syringe pump with multiple channels to withdraw the sample of five outlets.

Adhesion between surface and particles is one of the most challenges for the experiment of particle sample. According to the video recorder, it shows that when particles are moving into the chambers, they are starting moving slowly on the surface, due to surface adhesion, especially the large particles (20  $\mu\text{m}$ ) and then stop

moving completely while the small particles (10  $\mu\text{m}$ ) with less weight tend to flow along the fluid flow and then stop moving at the back chamber. In contrast, STO and LuMC cells which are much less weight tend to flow along the main stream and then trapped in the back row of chamber.





## **Appendix A Sample Preparation**

### **A1. Preparation for RBC Lysing Solutions (10X concentration)**

1. NH<sub>4</sub>Cl (ammonium chloride) 8.02 gm
2. NaHCO<sub>3</sub> (sodium bicarbonate) 0.84 gm
3. EDTA (disodium) 0.37 gm

Storing RBC Lysing Solutions (10X concentration) at 4°C

### **A2. RBC Lysing Solutions (1X concentration) Procedure**

Red blood cell (RBC) lysing solution is a buffer supplied as a 10X solution and should be diluted to 1X in DI-water. In this experiment, Red blood cell (RBC) lysing solution (10x concentration) 40 ml is diluted with 400 ml DI water in 500 ml beaker.

### **A3. Leukocyte Preparation for Cell Suspension**

1. Preparing donated whole blood (Canine) for 3 ml and then mix with RBC lysis buffer to lyse RBCs from whole blood into a 50 ml plastic centrifuge tube
2. Using centrifugation at 4 °C and 3,000 rpm for 20 minutes to allow leukocyte to sediment at the bottom of the tube.
3. Taking out the RBC lysing solution (supernatant) from the sediment of sample and using a pipette withdraw PBS and rinse RBC remaining inside the plastic centrifuge tube slowly and carefully until the red color from blood is disappeared from the sediment of leukocyte
4. Adding sufficient quantity of DI water to 45 ml into a 50 ml plastic centrifuge tube again.

### **A4. Biological Specimen Preparation for SEM**

1. Placing 1 drop of WBC suspension on a cover slip. Make sure the suspension is all over the plate.
2. Fixing specimens with 2.5% glutaraldehyde in 0.1 M phosphate buffer pH 7.2 for 1 hour.
3. Washing specimens twice with phosphate buffer to remove glutaraldehyde and then once with distilled water for 5 min/each.
4. Dehydrating specimen with a graded series of ethanol (30%, 50%, 70%, 95% 5 min/each and 100% 3 times, 5 min/time, respectively).
5. Removing fluid from specimens by evaporating with high-pressure heating to the critical point dry (critical point dryer, Quorum model K850, UK).
6. Mounting the specimen onto stubs with conductive tape and coat with gold (sputter coater, Balzers model SCD 040, Germany).

7. Observing by means under a SEM (JEOL, model JSM 6610LV, JAPAN).

#### **A5. Blood Smear**

1. Picking up a coverglass (make sure the coverglass is clean prior) with your thumb and index finger on adjacent corners.

2. Dropping a specimen (40  $\mu$ l) and touch the specimen with the coverglass at an angle. By using capillary attraction, the sample should be all over the coverglass.

3. Drying the specimen with air completely.

#### **A6. Biological Specimen Preparation of Wright's Stain**

1. Thoroughly sample (WBCs) smears on glass slide and completely dry with dry air without heat.

2. Fixing smears in absolute methanol for 10-15 seconds and completely dry with dry air again.

3. Staining smears in Wright-Giemsa Stain Solution for 10-15 seconds.

4. Rinsing smears in Phosphate Buffer for 10-15 seconds.

5. Examining smears under a microscope.

#### **A7. Fibroblast Preparation of Cell Suspension**

1. Starting with removing old media in a Petri dish with a pipette.

2. Putting fresh PBS to remove media from fibroblast in a Petri dish.

3. Using trypsin to isolate fibroblast and then pipet up and down several times.

4. Stopping the isolation of trypsin with placing media in Petri dish and pipet up and down several times.

5. Transferring the cell suspension to a 50 ml tube and pipet up and down several times.

6. Using centrifugation with 1000 rpm, 4 °C and 5 minutes to sink fibroblast at the bottom of the tube and remove supernatant.

7. Adding fresh media in the tube and pipet up and down several times to allow cells and media to be mixed well as cell suspension.

8. Counting the number of cell concentration in a hemocytometer.

#### **A8. Media Preparation for Mast Cell Tumor Cell Line (LuMC)**

##### Reagents

1. Dulbecco's Modified Eagle Medium solution 85% (v/v)

2. FBS 10% (v/v)

3. Anti-Anti (1% of volume)

4. MEM Non-essential Amino Acid Solution 100×, 1% (v/v)
5. MEM Amino Acids 50× solution 1%, (v/v)
6. Nucleoside 1%, (v/v)
7. L-glutamine 1%, (v/v)

This protocol makes 100 ml of media solution

#### **A9. Media Solution Procedure**

1. Obtaining Dulbecco's Modified Eagle Medium solution by mixing Dulbecco's Modified Eagle Medium powder with 1,000 ml of Milli-Q water and sodium bicarbonate.
2. Using filter of 0.2  $\mu\text{m}$  to separate debris or sediment of solution.
3. Putting the solution into a 100 ml bottle
4. Filling Enrofloxacin in to the solution (0.5  $\mu\text{l}$  of Enrofloxacin: 1 ml of solution) and then mixes them well.
5. Storing the solution at 4°C

#### **A10. Mast Cell Tumor Cell Line (LuMC) Preparation for of Cell Suspension**

1. Using the pipette of 100/1000 and withdrawn LuMC from a petri dish that is already prepared and then put the sample into a 15 ml centrifuge tube.
2. Using centrifugation at 4 °C and 1,000 rpm for 5 minutes
3. Taking out the supernatant fraction from the precipitated fraction of LuMC.
4. Putting media solution into the 15 ml centrifuge tube and then mixes them well together.

Note that, resuspend cells with media should be swirled and flaked to ensure that the resuspend cells with media is evenly distributed.

## Appendix B Cell Enumeration

### B1. Cell Enumeration Protocols for Hemocytometer

1. Use a pipette, withdraw 0.5 ml of cell suspension and 0.5 ml of Trypan Blue and put in a 2 ml eppendorf and then mixes together with bio-shaker for 5 minutes. After that, withdrawing 10  $\mu$ l of solution from the eppendorf and apply to the hemocytometer with both sides of chambers.

2. Try to find the grid lines by using a light microscope and focus with magnification of 10x, 20x and 40x, respectively.

3. Use a hand tally counter to count live and dead cells. Live cells are appeared as bright feature in circle, whereas the dead cells are appeared as a blue feature in circle.

4. Counting cells in 4 main areas (1 main area contains 16 small square areas). Cells are counted only in square areas and within on the right-hand or bottom boundary line.

### B2. Cell Concentration Formula

Cell concentration can be calculated from this following formula:

$$\text{Cell concentration} = \frac{\text{Total cells counted} \times \text{dilution factor} \times 10^4}{\text{numbers of squares}}$$

Example: In this experiment, total cells in 4 main areas are 200 cells. If you dilute cell suspension with Trypan Blue 1:1. The concentration (Cells/ml) will be:

$$\text{Cell concentration} = \frac{200 \times 2 \times 10^4}{4} = 10^6 \text{Cells/ml}$$

### B3. Percentage of Cell Viability Formula

Percentage of cell viability can be calculated from this following formula:

$$\text{Percentage of Cell viability} = \frac{(\text{Live cells}) \times 100}{(\text{Live cells} + \text{Dead cells})}$$

Example: In this experiment, live cells are 180 cells and dead cells are 20 cells. Percentage of cell viability will be:

$$\text{Percentage of Cell viability} = \frac{(180) \times 100}{(180 + 20)} = 90\%$$

PS. You can apply this formula to find the percentage of cell death also.

#### B4. Percentage of trapping distribution in a chamber

Percentage of trapping distribution can be calculated from this following formula:

1. Percentage of trapping distribution in a chamber

$$= \frac{W_n \times 100}{W_1 + W_2 \dots W_5}$$

Defined: Trapped particles with the same size in all wells of a chamber = W

Number of well = n

Example: In an experiment, 10  $\mu\text{m}$  particles are trapped for 800 particles in the 1<sup>st</sup> chamber ( $W_1$ ) and total particles in the five chambers are 1,000 particles. Percentage of trapping distribution will be:

$$\begin{aligned} \text{Percentage of trapping distribution} &= \frac{W_1 \times 100}{W_1 + W_2 \dots W_5} \\ &= \frac{(800) \times 100}{(1,000)} = 80\% \text{ for } 10 \mu\text{m particles} \end{aligned}$$

#### B5. Percentage of sorting efficacy in a chamber

Percentage of cell sorting efficacy in a chamber can be calculated from this following formula:

1. Percentage of sorting efficacy in a chamber

$$= \frac{(W_n + S_n + O_n) \times 100}{(W_1 + W_2 \dots W_5) + (S_1 + S_2 \dots S_5) + (O_1 + O_2 \dots O_5)}$$

Defined: Trapped particles with the same size in all wells of a chamber = W

Particles are on the surface around wells = S

Particles comes out at the outlet = O

Number of well = n

Example: In an experiment, 10  $\mu\text{m}$  particles are trapped for 600 particles in the 1<sup>st</sup> chambers, the number of particles on the surface is 100 particles and the number of particles of the outlets is 100 particles and total particles in all chambers are 1,000 particles. Percentage of sorting efficacy for 10  $\mu\text{m}$  particles will be:

$$\begin{aligned} \text{Percentage of sorting efficacy} &= \frac{(W_1 + S_1 + O_1) \times 100}{(W_1 + W_2 \dots W_5) + (S_1 + S_2 \dots S_5) + (O_1 + O_2 \dots O_5)} \\ &= \frac{(800) \times 100}{(1,000)} = 80\% \text{ for } 10 \mu\text{m particles} \end{aligned}$$

## REFERENCES

- [1] <http://www.who.int/news-room/fact-sheets/detail/cancer>. (2018).
- [2] <https://www.thairath.co.th/content/456247>. (2014).
- [3] <https://mgronline.com/around/detail/9560000155737>. (2013).
- [4] P. M. Kieran, D. M. Malone, and P. F. MacLoughlin, "Effects of Hydrodynamic and Interfacial Forces on Plant Cell Suspension Systems," in *Influence of Stress on Cell Growth and Product Formation*, 2000, pp. 139-177.
- [5] S. Fulda, A. M. Gorman, O. Hori, and A. Samali, "Cellular Stress Responses: Cell Survival and Cell Death," *International Journal of Cell Biology*, vol. 2010, p. 23, 2010, Art. no. 214074.
- [6] T. Tanzeglock, M. Soos, G. Stephanopoulos, and M. Morbidelli, "Induction of mammalian cell death by simple shear and extensional flows," *Biotechnol Bioeng*, vol. 104, no. 2, pp. 360-70, Oct 1 2009.
- [7] Z. Zhang, M. Al-Rubeai, and C. R. Thomas, "Estimation of Disruption of Animal Cells by Turbulent Capillary Flow," *Biotechnology and Bioengineering*, vol. 897-993, 1993.
- [8] A. McQueen, E. Meilhoc, and J. E. Bailey, "Flow Effects on the Viability And Lysis of Suspension Mammalian Cells " *Biotechnology Letters*, vol. 9, no. 831-836, 1987.
- [9] C. G. Smith, P. F. Greenfield, and D. H. Randerson, "A Technique For Determining The Shear Sensitivity of Mammalian Cells In Suspension Culture " *Biotechnology Technique*, vol. 1, 1987.
- [10] N. Ma, K. W. Koelling, and J. J. Chalmers, "Fabrication and use of a transient contractional flow device to quantify the sensitivity of mammalian and insect cells to hydrodynamic forces," *Biotechnol Bioeng*, vol. 80, no. 4, pp. 428-37, Nov 20 2002.
- [11] K. K. Chittur, L. V. McIntire, and R. R. Rich, "Shear Stress Effects on Human T Cell Function," *Biotechnology Progress*, vol. 4, no. 2, 1988.
- [12] J. Trampler, J. B. Williamst, and D. Joustra, "Shear sensitivity of insect cells in suspension," *Enzyme Microb. Technol*, vol. 8, 1986.
- [13] S. Goldblum, Y. K. Bae, W. F. Hink, and J. Chalmers, "Protective Effect of Methylcellulose and Other Polymers on Insect Cells Subjected to Laminar Shear Stress," *Biotechnol*, vol. 6, pp. 383-390, 1990.
- [14] J. F. Petersen, L. V. McIntire, and E. T. Papoutsakis, "Shear sensitivity of cultured hybridoma cells (CRL-8018) depends on mode of growth, culture age and metabolite concentration," *Journal of Biotechnology*, vol. 7, pp. 229-246, 1988.
- [15] M. Sato, M. J. Levesque, and R. M. Nerem, "Micropipette Aspiration of Cultured Bovine Aortic Endothelial Cells Exposed to Shear Stress," *Arteriosclerosis*, vol. 7, pp. 276-286.
- [16] I. Abu-Reesh and F. Kargi, "Biological responses of hybridoma cells to defined hydrodynamic shear stress," *Journal of Biotechnology*, vol. 9, pp. 167-178, 1989.
- [17] J. Hua, L. E. Erickson, T. Y. Yiin, and L. A. Glasgow, "A review of the effects of shear and interfacial phenomena on cell viability," *Crit Rev Biotechnol*, vol. 13, no. 4, pp. 305-28, 1993.

- [18] C. G. NEVARIL, E. C. LYNCH, C. P. ALFREY, JR., and J. D. HELLUMS, "Erythrocyte damage and destruction induced by shearing stress," *Lab. & Clin. Med.*, vol. 71, 1968.
- [19] L. B. Leverett, J. D. Hellums, C. P. Alfrey, and E. C. Lynch, "Red Blood Cell Damage By Shear Stress CELL " *Biophysical Journal* vol. 2, 1972.
- [20] S. P. Suter and M. H. Mehrjardi, "Deformation and Fragmentation of Human Red Blood Cell In Turbulent shear Flow," *Biophysical Journal* vol. 15, 1975.
- [21] A. M. Sallam and N. H. C. Hwang, "Human Red Blood Cell Hemolysis In A Turbulent Shear Flow : Contribution of Reynolds Shear Stresses " *Biorheology* vol. 21, pp. 783-797, 1984.
- [22] R. P. Bacher and M.C. Williams, "Hemolysis in capillary flow," *J Lab Clin Med*, vol. 76, pp. 485-96, 1970.
- [23] U. Schurch, H. Kramer, A. Einsele, F. Widmer, and H. M. Eppenberger, "Experimental evaluation of laminar shear stress on the behaviour of hybridoma mass cell cultures, producing monoclonal antibodies against mitochondrial creatine kinase," *Journal of Biotechnology*, vol. 7, pp. 179-184, 1988.
- [24] D. C. Augenstein, A. J. Sinskey, and D. I. C. Wang, "Effect of Shear on the Death of Two Strains of Mammalian Tissue Cells," *Biotechnology and Bioengineering* vol. XIII, pp. 409-418, 1971.
- [25] T. S. Dewitz, L. V. McIntire, and R. R. Martin, "Alteration of Human Leukocyte Chemotaxis, Chemiluminescence, and HMP Shunt Activity Caused By Mechanical Trauma," *Mechanical Trauma - Induced Leukocyte Dysfunction*, vol. 4, no. 4, 1980.
- [26] G. Kretzmer and K. Schiigerl, "Response of mammalian cells to shear stress," *Appl Microbiol Biotechnol*, vol. 34, pp. 613-616, 1991.
- [27] A. Ludwig, J. Tomeczkowski, and G. Kretzmer, "Influence of Shear Stress on Adherent Mammalian Cells During Division " *Biotechnology Letters* vol. 14, no. 10, pp. 881-884, 1992.
- [28] L. A. Down, D. V. Papavassiliou, and E. A. O'Rear, "Significance of extensional stresses to red blood cell lysis in a shearing flow," *Ann Biomed Eng*, vol. 39, no. 6, pp. 1632-42, Jun 2011.
- [29] B. A. Aguado, W. Mulyasmita, J. Su, K. J. Lampe, and S. C. Heilshorn, "Improving viability of stem cells during syringe needle flow through the design of hydrogel cell carriers," *Tissue Eng Part A*, vol. 18, no. 7-8, pp. 806-15, Apr 2012.
- [30] J.-H. Yen, S.-F. Chen, M.-K. Chern, and P.-C. Lu, "The Effects of Extensional Stress on Red Blood Cell Hemolysis," *Biomedical Engineering: Applications, Basis and Communications*, vol. 27, no. 05, p. 1550042, 2015.
- [31] Y. B. Bae *et al.*, "Microfluidic assessment of mechanical cell damage by extensional stress," *Lab Chip*, vol. 16, no. 1, pp. 96-103, Dec 15 2015.
- [32] A. A. Bhagat, S.S.Kuntaegowdanahalli, and I. Papautsky, "Continuous particle separation in spiral microchannels using Dean flows and differential migration," *Lab Chip*, vol. 8, no. 11, pp. 1906-14, Nov 2008.
- [33] A. ElHasni, K. Göbbels, A.L. Thiebes, P. Bräunig, W. Mokwa, and U. Schnakenberg, "Focusing and Sorting of Particles in Spiral Microfluidic Channels," *Procedia Engineering*, vol. 25, pp. 1197-1200, 2011.
- [34] J. M. Martel and M. Toner, "Inertial focusing dynamics in spiral microchannels,"

- Physics of Fluids*, vol. 24, 2012.
- [35] N. Xiang, K. Chen, D. Sun, S. Wang, H. Yi, and Z. Ni, "Quantitative characterization of the focusing process and dynamic behavior of differently sized microparticles in a spiral microchannel," *Microfluidics and Nanofluidics*, vol. 14, no. 1-2, pp. 89-99, 2012.
- [36] N. Xiang, K. Chen, Q. Dai, D. Jiang, D. Sun, and Z. Ni, "Inertia-Induced Focusing Dynamics of Microparticles Throughout a Curved Microfluidic Channel," *Microfluid Nanofluid*, vol. 18, pp. 29-39, 2015.
- [37] I. D. Johnston, M. B. McDonnell, C. K. L. Tan, D. K. McCluskey, M. J. Davies, and M. C. Tracey, "Dean flow Focusing and Separation of Small Microspheres within a Narrow Size Range," *Microfluid Nanofluid*, vol. 17, pp. 509-518, 2014.
- [38] S.S. Kuntaegowdanahalli, A.A. Bhagat, G. Kumar, and I. Papautsky, "Inertial microfluidics for continuous particle separation in spiral microchannels," *Lab Chip*, vol. 9, no. 20, pp. 2973-80, Oct 21 2009.
- [39] A. Thanomsridetchai *et al.*, "Focusing and sorting of multiple-sized beads and cells using low-aspect-ratio spiral microchannels," *Journal of Mechanical Science and Technology*, vol. 31, no. 11, pp. 5397-5405, 2017.
- [40] N. Nivedita and I. Papautskya), "Continuous Separation of Blood Cells in Spiral Microfluidic Devices," *Biomicrofluidics* vol. 7, 2013.
- [41] N. Xiang and Z. Ni, "High-throughput blood cell focusing and plasma isolation using spiral inertial microfluidic devices," *Biomed Microdevices*, vol. 17, no. 6, p. 110, Dec 2015.
- [42] N. Nivedita, P. Ligrani, and I. Papautsky, "Dean Flow Dynamics in Low-Aspect Ratio Spiral Microchannels," *Sci Rep*, vol. 7, p. 44072, Mar 10 2017.
- [43] E. Guzniczak, O. Otto, G. Whyte, N. Willoughby, M. Jimenez, and H. Bridle, "Deformability-induced lift force in spiral microchannels for cell separation," *Lab Chip*, vol. 20, no. 3, pp. 614-625, Feb 7 2020.
- [44] S. S. Nathamgari *et al.*, "Isolating single cells in a neurosphere assay using inertial microfluidics," *Lab Chip*, vol. 15, no. 24, pp. 4591-7, Dec 21 2015.
- [45] H. Song *et al.*, "Spiral-shaped inertial stem cell device for high-throughput enrichment of iPSC-derived neural stem cells," *Microfluid Nanofluid*, vol. 21-64, 2017.
- [46] J. Son, O. Badamjav, T. Jenkins, B. Gale, J. Hotaling, and D. Carrell, "Active Higher Quality Sperm Separation Using a Spiral Channel," in *19th International Conference on Miniaturized Systems for Chemistry and Life Sciences*, Gyeongju, KOREA, 2015.
- [47] A. Schaap, J. Dumon, and J. Toonder, "Sorting algal cells by morphology in spiral microchannels using inertial microfluidics," *Microfluid Nanofluid*, p. 20:125, 2016.
- [48] J. Son, K. Murphy, R. Samuel, B. K. Gale, D. T. Carrell, and J. M. Hotaling, "Non-motile sperm cell separation using a spiral channel," *Analytical Methods*, vol. 7, no. 19, pp. 8041-8047, 2015.
- [49] J. Son, R. Samuel, B. K. Gale, D. T. Carrell, and J. M. Hotaling, "Separation of sperm cells from samples containing high concentrations of white blood cells using a spiral channel," *Biomicrofluidics* vol. 11, 2017.
- [50] L. Wu, G. Guan, H.W. Hou, A. A. Bhagat, and J. Han, "Separation of leukocytes from blood using spiral channel with trapezoid cross-section," *Anal Chem*, vol.



- 84, no. 21, pp. 9324-31, Nov 6 2012.
- [51] G. Guan *et al.*, "Spiral Microchannel with Rectangular and Trapezoidal Cross-Sections for Size Based Particle Separation," *Sci Rep*, vol. 3, p. 1475, 2013.
- [52] M. E. Warkiani *et al.*, "Slanted spiral microfluidics for the ultra-fast, label-free isolation of circulating tumor cells," *Lab Chip*, vol. 14, no. 1, pp. 128-137, 2014.
- [53] T. Kwon *et al.*, "Microfluidic Cell Retention Device for Perfusion of Mammalian Suspension Culture," *SCIENTIFIC Reports*, vol. 7, p. 6703, 2017.
- [54] A. Al-Halhouli, W. Al-Faqheri, B. Alhamarneh, L. Hecht, and A. Dietzel, "Spiral Microchannels with Trapezoidal Cross Section Fabricated by Femtosecond Laser Ablation in Glass for the Inertial Separation of Microparticles," *Micromachines (Basel)*, vol. 9, no. 4, Apr 9 2018.
- [55] A. S. Rzhavskiy *et al.*, "Rapid and Label-Free Isolation of Tumour Cells from the Urine of Patients with Localised Prostate Cancer Using Inertial Microfluidics," *Cancers (Basel)*, vol. 12, no. 1, Dec 29 2019.
- [56] S. Ghadami, R. K. Esfahan, M. S. Saidi, and K. Firoozbakhsh, "Spiral microchannel with stair-like cross section for size-based particle separation," *Microfluid Nanofluid*, pp. 21-115, 2017.
- [57] J. Sun *et al.*, "Double spiral microchannel for label-free tumor cell separation and enrichment," *Lab Chip*, vol. 12, no. 20, pp. 3952-60, Oct 21 2012.
- [58] X. Wang *et al.*, "Efficient fractionation of cellulose nanofibers using spiral microchannel," *Cellulose*, 2020.
- [59] T. H. Kim, H. J. Yoon, P. Stella, and S. Nagrath, "Cascaded spiral microfluidic device for deterministic and high purity continuous separation of circulating tumor cells," *Biomicrofluidics* 2014.
- [60] A. Abdulla, W. Liu, A. Gholamipour-Shirazi, J. Sun, and X. Ding, "High-Throughput Isolation of Circulating Tumor Cells Using Cascaded Inertial Focusing Microfluidic Channel," *Anal Chem*, vol. 90, no. 7, pp. 4397-4405, Apr 3 2018.
- [61] H. Chen, "A Triplet Parallelizing Spiral Microfluidic Chip for Continuous Separation of Tumor Cells," *Scientific Reports*, vol. 8, p. 4042, 2018.
- [62] B. L. Khoo *et al.*, "Clinical validation of an ultra high-throughput spiral microfluidics for the detection and enrichment of viable circulating tumor cells," *PLoS One*, vol. 9, no. 7, p. e99409, 2014.
- [63] M. E. Warkiani *et al.*, "Ultra-fast, label-free isolation of circulating tumor cells from blood using spiral microfluidics," *Nat Protoc*, vol. 11, no. 1, pp. 134-48, Jan 2016.
- [64] M. E. Warkiani, A. K. Tay, G. Guan, and J. Han, "Membrane-less microfiltration using inertial microfluidics," *Sci Rep*, vol. 5, p. 11018, Jul 8 2015.
- [65] A. Mihandoust, N. Maleki-Jirsaraei, S. Rouhani, S. Safi, and M. Alizadeh, "Improvement of size-based particle separation throughput in slanted spiral microchannel by modifying outlet geometry," *Electrophoresis*, vol. 41, no. 5-6, pp. 353-359, Mar 2020.
- [66] J. Zhang *et al.*, "Fundamentals and applications of inertial microfluidics: a review," *Lab Chip*, vol. 16, no. 1, pp. 10-34, Jan 7 2016.
- [67] M. G. Lee, S. Choi, and J. K. Park, "Inertial separation in a contraction-expansion array microchannel," *J Chromatogr A*, vol. 1218, no. 27, pp. 4138-43, Jul 8 2011.

- [68] M. G. Lee, J. H. Shin, C.Y. Bae, S. Choi, and J. K. Park, "Label-free cancer cell separation from human whole blood using inertial microfluidics at low shear stress," *Anal Chem*, vol. 85, no. 13, pp. 6213-8, Jul 2 2013.
- [69] J. S. Park, S. H. Song, and H. I. Jung, "Continuous focusing of microparticles using inertial lift force and vorticity via multi-orifice microfluidic channels," *Lab Chip*, vol. 9, no. 7, pp. 939-48, Apr 7 2009.
- [70] Z. Wu, Y. Chen, M. Wang, and A. J. Chung, "Continuous inertial microparticle and blood cell separation in straight channels with local microstructures," *Lab Chip*, vol. 16, no. 3, pp. 532-42, Feb 7 2016.
- [71] X. Wang, J. Zhou, and I. Papautsky, "Vortex-aided inertial microfluidic device for continuous particle separation with high size-selectivity, efficiency, and purity," *BIOMICROFLUIDICS*, vol. 7, 2013.
- [72] X. Wang and I. Papautsky, "Size-based microfluidic multimodal microparticle sorter," *Lab Chip*, vol. 15, no. 5, pp. 1350-9, Mar 7 2015.
- [73] X. Wang, X. Yang, and I. Papautsky, "An integrated inertial microfluidic vortex sorter for tunable sorting and purification of cells," *Technology*, vol. 04, no. 02, pp. 88-97, 2016.
- [74] S. C. Hur, A. J. Mach, and D. Di Carlo, "High-throughput size-based rare cell enrichment using microscale vortices," *Biomicrofluidics*, vol. 5, no. 2, p. 22206, Jun 2011.
- [75] J. Zhang, M. Li, W. H. Li, and G. Alici, "Inertial focusing in a straight channel with asymmetrical expansion-contraction cavity arrays using two secondary flows," *Journal of Micromechanics and Microengineering*, vol. 23, no. 8, p. 085023, 2013.
- [76] D. Yuan *et al.*, "Dean-flow-coupled elasto-inertial three-dimensional particle focusing under viscoelastic flow in a straight channel with asymmetrical expansion-contraction cavity arrays," *Biomicrofluidics*, vol. 9, no. 4, p. 044108, Jul 2015.
- [77] L. Liu, L. Han, X. Shi, W. Tan, W. Cao, and G. Zhu1, "Hydrodynamic separation by changing equilibrium positions in contraction-expansion array channels," *Microfluidics and Nanofluidics*, vol. 23, no. 52, 2019.
- [78] C. H. Hsu, D. D. Carlo, C. Chen, D. Irimiaa, and M. Toner, "Microvortex for focusing, guiding and sorting of particles," *Lab Chip*, vol. 8, pp. 2128-2134, 2008.
- [79] M. P. MacDonald, G. C. Spalding, and K. Dholakia1, "Microfluidic sorting in an optical lattice," *NATURE* vol. 426, 2003.
- [80] M. M. Wang *et al.*, "Microfluidic sorting of mammalian cells by optical force switching," *NATURE BIOTECHNOLOGY*, vol. 23, no. 1, 2005.
- [81] G. J. Shah, A. T. Ohta, E. P. Y. Chiou, M. C. Wu, and C. J. C. Kim, "EWOD-driven droplet microfluidic device integrated with optoelectronic tweezers as an automated platform for cellular isolation and analysis," *Lab Chip*, vol. 9, pp. 1732-1739, 2009.
- [82] M. Werner, F. Merenda, J. Piguet, R. P. Salathe, and H. Vogel, "Microfluidic array cytometer based on refractive optical tweezers for parallel trapping, imaging and sorting of individual cells," *Lab Chip*, vol. 11, no. 2432, 2011.
- [83] X. Wang *et al.*, "Enhanced cell sorting and manipulation with combined optical tweezer and microfluidic chip technologies," *Lab Chip*, vol. 11, no. 3656, 2011.

- [84] A. Keloth, O. Anderson, D. Risbridger, and L. Paterson, "Single Cell Isolation Using Optical Tweezers," *Micromachines*, vol. 9, no. 434, 2018.
- [85] F. Bragheri *et al.*, "Optofluidic integrated cell sorter fabricated by femtosecond lasers," *Lab Chip*, vol. 12, no. 19, pp. 3779-84, Oct 7 2012.
- [86] Y. Chen, T. H. Wu, Y. C. Kung, M. A. Teitell, and P. Y. Chiou, "3D pulsed laser-triggered high-speed microfluidic fluorescence-activated cell sorter," *Analyst*, vol. 138, no. 24, pp. 7308-15, Nov 12 2013.
- [87] Q.-l. Li, B.-w. Li, and Y.-q. Wang, "Surface-enhanced Raman scattering microfluidic sensor," *RSC Advances*, vol. 3, no. 32, p. 13015, 2013.
- [88] K. E. Bates and H. Lu, "Optics-Integrated Microfluidic Platforms for Biomolecular Analyses," *Biophysical Journal*, vol. 110, no. 8, pp. 1684-1697, 2016.
- [89] J. J. Lee *et al.*, "Synthetic ligand-coated magnetic nanoparticles for microfluidic bacterial separation from blood," *Nano Lett*, vol. 14, no. 1, pp. 1-5, Jan 8 2014.
- [90] H. Ki-Ho and A. B. Frazier, "Diamagnetic capture mode magnetophoretic microseparator for blood cells," *Journal of Microelectromechanical Systems*, vol. 14, no. 6, pp. 1422-1431, 2005.
- [91] K. H. Han and A. B. Frazier, "Paramagnetic capture mode magnetophoretic microseparator for high efficiency blood cell separations," *Lab Chip*, vol. 6, no. 2, pp. 265-73, Feb 2006.
- [92] Y. Wang, Y. Zhao, and S. K. Cho, "Efficient in-droplet separation of magnetic particles for digital microfluidics," *Journal of Micromechanics and Microengineering*, vol. 17, no. 10, pp. 2148-2156, 2007.
- [93] H. Lee, L. Xu, B. Ahn, K. Lee, and K. W. Oh, "Continuous-flow in-droplet magnetic particle separation in a droplet-based microfluidic platform," *Microfluidics and Nanofluidics*, vol. 13, no. 4, pp. 613-623, 2012.
- [94] E. Brouzes, T. Kruse, R. Kimmerling, and H. H. Strey, "Rapid and continuous magnetic separation in droplet microfluidic devices," *Lab Chip*, vol. 15, no. 3, pp. 908-19, Feb 7 2015.
- [95] R. Zhou and C. Wang, "Multiphase ferrofluid flows for micro-particle focusing and separation," *Biomicrofluidics*, vol. 10, no. 3, p. 034101, May 2016.
- [96] J. Wu, Y. Cui, S. Xuan, and X. Gong, "3D-printed microfluidic manipulation device integrated with magnetic array," *Microfluidics and Nanofluidics*, vol. 22, no. 103, 2018.
- [97] S. Zhi, X. Sun, Z. Feng, C. Lei, and Y. Zhou, "An innovative micro magnetic separator based on 3D micro-coppercoil exciting soft magnetic tips and FeNi wires for bio-target sorting," *Microfluidics and Nanofluidics*, vol. 23, no. 43, 2019.
- [98] H. S. Moon *et al.*, "Continuous separation of breast cancer cells from blood samples using multi-orifice flow fractionation (MOFF) and dielectrophoresis (DEP)," *Lab Chip*, vol. 11, no. 6, pp. 1118-25, Mar 21 2011.
- [99] A. Alazzam, B. Mathew, and F. Alhammadi, "Novel microfluidic device for the continuous separation of cancer cells using dielectrophoresis," *J Sep Sci*, vol. 40, no. 5, pp. 1193-1200, Mar 2017.
- [100] J. Sun *et al.*, "Simultaneous on-chip DC dielectrophoretic cell separation and quantitative separation performance characterization," *Anal Chem*, vol. 84, no. 4, pp. 2017-24, Feb 21 2012.

- [101] T. N. G. Adams, A. Y. L. Jiang, P. D. Vyas, and L. A. Flanagan, "Separation of neural stem cells by whole cell membrane capacitance using dielectrophoresis," *Methods*, vol. 133, pp. 91-103, Jan 15 2018.
- [102] L. D'Amico, N. J. Ajami, J. A. Adachi, P. R. Gascoyne, and J. F. Petrosino, "Isolation and concentration of bacteria from blood using microfluidic membraneless dialysis and dielectrophoresis," *Lab Chip*, vol. 17, no. 7, pp. 1340-1348, Mar 29 2017.
- [103] M. P. Barrett *et al.*, "Microfluidics-Based Approaches to the Isolation of African Trypanosomes," *Pathogens*, vol. 6, no. 4, Oct 5 2017.
- [104] D. F. Chen, H. Du, and W. H. Li, "A 3D paired microelectrode array for accumulation and separation of microparticles," *Journal of Micromechanics and Microengineering*, vol. 16, no. 7, pp. 1162-1169, 2006.
- [105] H. S. Moon, Y. W. Nam, J. C. Park, and H. I. Jung, "Dielectrophoretic Separation of Airborne Microbes and Dust Particles Using a Microfluidic Channel for Real-Time Bioaerosol Monitoring," *Environ. Sci. Technol.*, vol. 43, pp. 5857-5863, 2009.
- [106] H. Sadeghian, Y. Hojjat, and M. Soleimani, "Interdigitated electrode design and optimization for dielectrophoresis cell separation actuators," *Journal of Electrostatics*, vol. 86, pp. 41-49, 2017.
- [107] M. Li and D. Li, "Separation of Janus droplets and oil droplets in microchannels by wall-induced dielectrophoresis," *J Chromatogr A*, vol. 1501, pp. 151-160, Jun 9 2017.
- [108] Y. Wang, J. Wang, X. Wu, Z. Jiang, and W. Wang, "Dielectrophoretic separation of microalgae cells in ballast water in a microfluidic chip," *Electrophoresis*, vol. 40, no. 6, pp. 969-978, Mar 2019.
- [109] A. Lenshof *et al.*, "Acoustic Whole Blood Plasmapheresis Chip for Prostate Specific Antigen Microarray Diagnostics," *Anal. Chem*, vol. 81, pp. 6030-6037, 2009.
- [110] P. Augustsson, C. Magnusson, M. Nordin, H. Lilja, and T. Laurell, "Microfluidic, label-free enrichment of prostate cancer cells in blood based on acoustophoresis," *Anal Chem*, vol. 84, no. 18, pp. 7954-62, Sep 18 2012.
- [111] C. Ratier and M. Hoyos, "Acoustic Programming in Step-Split-Flow Lateral-Transport Thin Fractionation," *Anal. Chem.*, vol. 82, pp. 1318-1325, 2010.
- [112] Y. Liu and K. M. Lim, "Particle separation in microfluidics using a switching ultrasonic field," *Lab Chip*, vol. 11, no. 18, pp. 3167-73, Sep 21 2011.
- [113] G. Destgeer, K. H. Lee, J. H. Jung, A. Alazzam, and H. J. Sung, "Continuous separation of particles in a PDMS microfluidic channel via travelling surface acoustic waves (TSAW)," *Lab Chip*, vol. 13, no. 21, pp. 4210-6, Nov 7 2013.
- [114] N. M. Karabacak *et al.*, "Microfluidic, marker-free isolation of circulating tumor cells from blood samples," *Nat Protoc*, vol. 9, no. 3, pp. 694-710, Mar 2014.
- [115] J. Jiang *et al.*, "An integrated microfluidic device for rapid and high-sensitivity analysis of circulating tumor cells," *Scientific Reports*, p. 7:42612, 2017.
- [116] G. R. Aguirre, V. Efremov, M. Kitsara, and J. Ducre'ee, "Integrated micromixer for incubation and separation of cancer cells on a centrifugal platform using inertial and dean forces," *Microfluid Nanofluid*, 2014.
- [117] S. K. Ravula *et al.*, "A microfluidic system combining acoustic and dielectrophoretic particle preconcentration and focusing," *Sensors and Actuators*

- B: Chemical*, vol. 130, no. 2, pp. 645-652, 2008.
- [118] B. Cetin, M. B. Ozer, E. Cagatay, and S. Buyukkocak, "An integrated acoustic and dielectrophoretic particle manipulation in a microfluidic device for particle wash and separation fabricated by mechanical machining," *Biomicrofluidics*, vol. 10, no. 1, p. 014112, Jan 2016.
- [119] X. Chen *et al.*, "A Simplified Microfluidic Device for Particle Separation with Two Consecutive Steps: Induced Charge Electro-osmotic Prefocusing and Dielectrophoretic Separation," *Anal Chem*, vol. 89, no. 17, pp. 9583-9592, Sep 5 2017.
- [120] J. Zhang *et al.*, "Tunable particle separation in a hybrid dielectrophoresis (DEP)-inertial microfluidic device," *Sensors and Actuators B: Chemical*, vol. 267, pp. 14-25, 2018.
- [121] H. Chen, Z. Zhang, H. Liu, Z. Zhang, C. Lin, and B. Wang, "Hybrid magnetic and deformability based isolation of circulating tumor cells using microfluidics," *AIP Advances*, vol. 9, no. 2, p. 025023, 2019.
- [122] G. S. Fiorini and D. T. Chiu, "Disposable microfluidic devices: fabrication, function, and application," *BioTechniques*, vol. 38, no. 3, 2005.
- [123] W. T. Liu and L. Zhu, "Environmental microbiology-on-a-chip and its future impacts," *Trends Biotechnol*, vol. 23, no. 4, pp. 174-9, Apr 2005.
- [124] C. Zhang, J. Xu, W. Ma, and W. Zheng, "PCR microfluidic devices for DNA amplification," *Biotechnol Adv*, vol. 24, no. 3, pp. 243-84, May-Jun 2006.
- [125] U. Kim, A. Ravikumar, J. Seubert, and S. Figueira, "Detection of Bacterial Pathogens through Microfluidic DNA Sensors and Mobile Interface toward Rapid, Affordable, and Point-of-Care Water Monitoring," presented at the IEEE Point-of-Care Healthcare Technologies (PHT), Bangalore, India, 2013.
- [126] F. Ligler *et al.*, "Remote Sensing Using an Airborne Biosensor," *Environ. Sci. Technol.*, vol. 32, pp. 2461-2466, 1998.
- [127] J. Cleary, D. Maher, and D. Diamond, "Development and deployment of a microfluidic platform for water quality monitoring. In Smart Sensors for Real-Time Water Quality Monitoring.," presented at the Springer-Verlag, Berlin, Heidelberg, 2013.
- [128] M. X. Yang, B. Wang, X. Hu, and H.-S. P. Wong, "A simple technique to design microfluidic devices for system integration," *The Royal Society of Chemistry*, 2017.
- [129] B. Y. Yu, C. Elbuken, C. Shen, J. P. Huissoon, and C. L. Ren, "An integrated microfluidic device for the sorting of yeast cells using image processing," *SCIENTIFIC REPOrTS*, p. 8:3550, 2018.
- [130] I. M. Syntouka, P. E. Riches, G. Busby, and A. KAZAKIDI, "Flow Simulation of A Natural Polymer in A Syringe-Needle Delivery Device," in *7th European Conference on Computational Fluid Dynamics (ECFD 7)*, 11-15 June 2018, Glasgow, UK, 2018.
- [131] T. Chunfong, "The effect of the tip angles of the diamond microwell on cell-spheroid formation," master degree, mechanical engineering, Chulalongkorn university, 2020.

## VITA

**NAME** Thammawit Suwannaphan

**DATE OF BIRTH** 19 Oct 1987

**PLACE OF BIRTH** Phitsanulok

**INSTITUTIONS ATTENDED** Chulalongkorn University, 2016-2020  
Doctor of Philosophy's Degree of Engineering,  
Mechanical Engineering.

Chulalongkorn University, 2014-2016  
Master's Degree of Engineering, Mechanical  
Engineering.

King Mongkut's University of Technology North  
Bangkok, 2006-2010  
Bachelor's Degree of Engineering, Aerospace  
Engineering

King Mongkut's Institute of Technology North  
Bangkok, 2003-2006  
Certificate in Technical Education, Mechanics.

**HOME ADDRESS** 580/86, Soi Phopun, Rama 9 Road, Asok DinDeng,  
Bangkok, Thailand 10400

**PUBLICATION** Investigation of Leukocyte Viability and Damage in  
Spiral Microchannel and Contraction-Expansion  
Array